ABSTRACT

Title: FUEL INJECTION IN SCRAMJETS: MIXING ENHANCEMENT AND COMBUSTION CHARACTERIZATION EXPERIMENTS

Andrew Henry Zang, Master of Science, 2005

Directed By: Associate Professor, Dr. Kenneth H. Yu, Department of Aerospace Engineering

A two-part experimental study was conducted to address the issues of supersonic fuel mixing enhancement and efficient combustor development. The first part of the study involved quantitative characterization of fuel-air mixing in a non-reacting supersonic flowfield. Two flow configurations were compared: i.) a baseline case with normal fuel injection and ii.) a case with an acoustically open cavity placed downstream of the injection in order to excite mixing. Direct measurements of local atomic fuel-air ratio were acquired using Laser Induced Breakdown Spectroscopy (LIBS), which was applied for the first time in a supersonic flowfield. Indirect measurements of fuel

spreading rate were inferred from intensity gradients in time-averaged Schlieren images. The quantitative results were compared to show conclusive gains in fuel-air mixing rate for the cavity configuration. LIBS was proven as an effective diagnostic for quantifying supersonic mixing. In the second part of the study, a baseline supersonic combustor was designed, built, and tested for future comparative studies of combustion performance. The combustor featured a square cross-section and a three-dimensional expanding section, with optical access on one side. Combustor wall pressure was measured at various fuel injection conditions. Supersonic combustion was evident for some conditions, but results indicated poor combustion efficiency for all cases. This shows the need for either mixing enhancement or a redesign of the baseline conditions.

FUEL INJECTION IN SCRAMJETS: MIXING ENHANCEMENT AND COMBUSTION CHARACTERIZATION EXPERIMENTS

By

Andrew Henry Zang

Thesis submitted to the Faculty of the Graduate School of the
University of Maryland, College Park, in partial fulfillment
of the requirements for the degree of
Master of Science
2005

Advisory Committee:
Dr. Ken Yu, Chair
Dr. Mark Lewis
Dr. Chris Cadou

DEDICATION

I would like to dedicate this thesis to my devoted girlfriend, Hannah, and my loving family. Without their continuing support and advice I do not believe I could have ever made it this far in life. Because of their understanding and unconditional belief in my hopes and aspirations I have been able to drive myself to excel in my studies. Their contributions have been tremendous and wide-ranging in nature, and for that I will forever be indebted to them. It is for these reasons and countless more that this work is presented and dedicated in their honor.

ACKNOWLEDGEMENTS

I would like to acknowledge first, and foremost, my advisor Dr. Kenneth Yu. His constant help and guidance have been paramount in my success as a graduate student, and in my successful completion of this thesis. I would also like to thank Dr. Mark Lewis for his guidance throughout my graduate studies and for serving on my thesis committee. Additionally, I would like to thank Dr. Chris Cadou for his insight as well as being my third thesis committee member.

My thanks go out to my fellow graduate students namely those who share office space in the SVT office. Their collective motivation and support has made my graduate experience an enjoyable and successful venture. Without their council I am sure that I would have found my graduate studies to be considerably more stressful and difficult.

Finally I would like to acknowledge the funding which made this research possible. This work has been sponsored by the Space Vehicle Technology Institute, under grant NCC3-989, one of the NASA University Institutes, with joint sponsorship from the Department of Defense. Additional funding was provided by the Office of Naval Research grant N000140110698. Appreciation is expressed to Claudia Meyer, Mark Klem, and Harry Cikanek of the NASA Glen Research Center, Dr. John Schmisseur and Dr. Walter Jones of the Air Force Office of Scientific Research, and Dr. Gabriel Roy of the Office of Naval Research.

TABLE OF CONTENTS

LIST OF TABLES

LIST OF FIGURES

TABLE OF NOMENCLATURE

A	Area
a	Speed of sound
C_δ	Change in shear layer growth
$(C_\delta)_0$	Change in shear layer growth for incompressible shear layer
C_p	Phase speed
C_∞	Freestream speed of sound
D	Characteristic depth
f_n	Frequency of n harmonic
H	Characteristic height
L	Characteristic length
L/D	Length to depth ratio
M_1	Mach number in stream 1
M_2	Mach number in stream 2
M_c	Convective Mach number
n	Mode number
OH*	Hydroxyl radical
P_0	Stagnation pressure
P	Static pressure
P_w	Wall static pressure
Sr_L	Strouhal number of characteristic L
T_{AFT}	Adiabatic flame temperature
T_σ	Mass averaged fuel and air temperature at burner entry
$t_{combustion}$	Time for combustion to occur
t_{chem}	Time for chemical reaction
t_{mixng}	Time for mixing to occur
$t_{convective}$	Convection time of the disturbance in the shear layer
$t_{acoustic}$	Time for the acoustic wave to travel upstream inside the cavity
t_{phase}	Phase delay associated with the acoustic process
t_{ind}	Induction time
U_1	Velocity in stream 1
U_2	Velocity in stream 2
U_c	Convective velocity
U_∞	Freestream velocity
W	Characteristic width
x	Distance downstream
Greek Symbols	
α	Phase delay term
γ	Ratio of specific heats
Δu	Change in velocity
δ_m, δ'	Shear layer height
δ_0	Shear layer height, incompressible flow

η_b	Burner efficiency
ν	Sweep angle
σ_m	Standard error of the mean
σ	Standard deviation
ϕ	Equivalence ratio

Acronyms

AR	Aspect Ratio
CR	Contraction Ratio
EISP	Estimated specific impulse
ER	Equivalence Ratio
LIBS	Laser Induced Breakdown Spectroscopy
RDP	Radial Deviation Parameter
SSTO	Single Stage to Orbit
TPS	Thermal Protection System

1 Introduction

1.1 Background and Motivation

For over 50 years the development and importance of ramjet and scramjet engines has been prevalent in pursuing high speed air breathing flight applications. From hypersonic missile systems to access to space concepts the advantages of an air breathing propulsion system have long been desired. The principal advantage of utilizing the atmosphere as a combustion oxidizer is paramount in the study of such vehicles. However achieving sustainable stable combustion is an event that "is like lighting a match in a hurricane" according to NASA officials. This engineering problem is one which has been extensively studied, and is also the impetus for both sets of experiments investigated within this thesis.

1.1.1 Scramjet Development

Beginning as early as 1946 the concept of possibly adding heat directly to a supersonic stream by the means of a standing wave was proposed[1]. Although the concept of supersonic combustion was realized the complications involved with supersonic combustion were only beginning to be explored. Early work by Ferri[2,3] explored these complications and for this work he is widely credited as the major leader in exploring scramjet technology in the United States in the 1960s[4]. Weber and McKay[5] followed up Ferri's early work and anticipated some major technical

hurdles facing scramjet development including fuel injection and mixing without severe shock losses, wall cooling and frictional losses, nozzle performance, as well as the need for a diverging combustor to avoid thermal choking[4]. Clearly scramjet issues, in particular combustor issues, were defined very early on in the history of scramjets.

The combustor is of particular interest because of the need to have the fuel and air mix and combust efficiently on both the micro (or molecular) and macro (or large) scale at supersonic speeds. As the Mach number is increased the molecular level mixing of fuel and air becomes retarded due to the stabilizing influence of compressibility on the turbulent mixing layer[6]. These issues are even more dramatic when a small vehicle is examined as the skin friction drag becomes a more significant part of the overall drag. Therefore a means of increasing turbulent mixing and thus reducing mixing length and in turn combustor length would be of great benefit[7].

One means of increasing this turbulent mixing is the placement of a cavity adjacent to the flow in the combustor, which produces large coherent structures. The structures shed by these cavities have been shown to be very important for air entrainment and thus mixing[8]. Cavities have also been tested experimentally to act as flame holding devices in scramjet systems. Their relatively low pressure drop, as compared to strut and other forms of injection, make them a more attractive flame holding device[7,9]. Previous work performed at the University of Maryland by Nenmeni et al.[10] investigated the application of these cavities over a wide range of flow conditions and cavity geometries. This work also briefly investigated a

simulated fuel injection of helium coupled with the cavity system to identify the fuel-air mixing qualities.

One focus of the present study is to enhance the characterization of one such coupled cavity and simulated fuel injection system over a wide range of flow conditions with new and enhanced diagnostic techniques. The utilization of Laser Induced Breakdown Spectroscopy (LIBS), which has never been previously applied to supersonic flow, will demonstrate both the robustness of the diagnostic technique and provide quantitative flow mixing information. Schlieren imagery is also used in a novel approach to provide 'frozen' images of the coherent structures as well as provide a basis with which to qualify the LIBS measurements. Thorough discussions of these techniques and their results can be found in the following chapters of this thesis.

1.1.2 Vehicle Design and Combustor Considerations

Another area of great development and investigation over the last 50 years is that of hypersonic vehicle shape and inlet configuration. With advances in computational design and computing power, new and interesting designs have been proposed for hypersonic air-breathing missions ranging from cruise missile applications to single-stage-to-orbit (SSTO) flight. The design envelope for such vehicles is relatively small, requiring the vehicles to maintain a high capture area ratio, compress the captured airflow to pre-combustion conditions, act as an integrated airframe-engine system, handle the high heating loads present, and

accommodate internally the payload, structure, and fuel for the given mission[11]. A main area of concern for all hypersonic vehicles is heating, most specifically in the combustor area where heat release from combustion adds to the already high heating loads associated with supersonic flight.

Traditional wedge derived wave riding designs for hypersonic vehicles utilize two dimensional flow paths to take advantage of theoretical two dimensional uniform flows through the inlet. These designs reduce the complexity of computing hypersonic flow fields and have good on-design characteristics. However, their two dimensional nature create large aspect ratio inlets which result in large aspect ratio combustors. These combustion chambers thus have large surface areas for thermal conduction and need a larger mass of thermal protection. New vehicle design techniques were developed to address these problems.

The inverse design procedure of carving out an airframe using the streamsurfaces of a known field is one such approach to improve hypersonic vehicle design[12]. Examples of these types of designs have been proposed for conical flow derived vehicles by Takashima and Lewis[13] and for inward turning axisymmetric vehicles by Billig[14]. Further study into these types of vehicles by Kothari[15,16] and Billig[12] developed another methodology of vehicle design that utilizes a modified method of characteristics. This design approach established the role of a Radial Deviation Parameter (RDP) in generating a range of vehicle profiles. The RDP is defined as the degree to which a generating method of characteristics is deviating from two-dimensional flow. For example, RDP = 1 corresponds to a completely

inward turning, isentropic, conical compression whereas RDP = 0 corresponds to an isentropic but entirely two-dimensional inlet flow. Examples of various vehicle designs as a function of the RDP for a range of RDP's are presented in Figure 1.1.

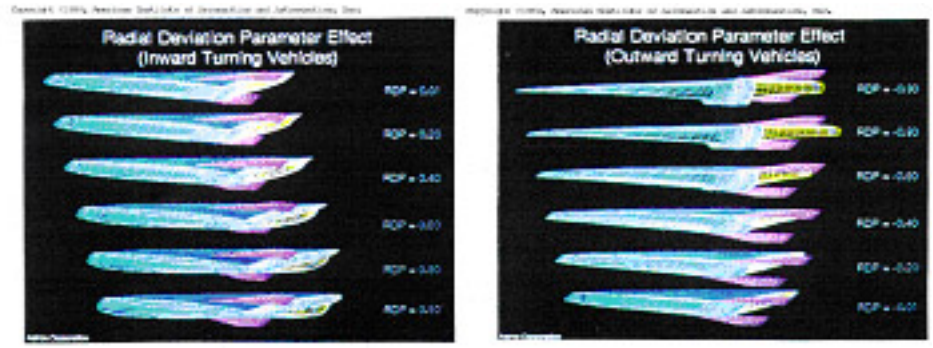

Figure 1.1: Conceptual Vehicle Designs for Various RDP Values

In Kothari's studies it was shown that, when compared to equivalent two-dimensional vehicles, an axisymmetric compression configuration may produce an improvement in EISP of 200-400 seconds over equivalent 2-D configurations in the hypersonic Mach number regime[15]. With predicted performance improvements of this nature possible, the motivation to experimentally investigate these designs is paramount.

Many assumptions are made when developing computational models of hypersonic vehicles, particularly within the combustor. Often quasi-one-dimensional and simplified chemical kinetics are required to reduce the computational demands associated with reaction chemistry. CFD models based on the Reynolds averaged Navier-Stokes equations use models for turbulent fluxes that employ many ad hock assumptions and empirically determined coefficients[17]. Although required to make the computational problem tractable, these simplifications often reduce the accuracy

of the model. Furthermore the large number of adjustable parameters typically leads to a low confidence in the models prediction when they are applied to classes of flows for which they have not been experimentally validated. An example of these issues is documented by Cutler[1718] where computational models fail to fully correspond to measurements of the combustion of hydrogen fuel made under flight enthalpy conditions in NASA Langley's Direct-Connect Supersonic Combustion Facility. Their calculation underestimated the length of the ignition region and indicated that there were problems with uncertainty in their kinetics model and/or a need to account for turbulence-chemistry interactions. These errors are a major motivator in acquiring empirical data, both for CFD validation and general characterization of supersonic combustion systems.

For these reasons the other focus of this study was to generate a baseline characterization of the combustion in a supersonic duct with an aspect ratio of one. This characterization would serve as the benchmark against which the testing of combustion configurations developed by novel vehicle designs, specifically those produced by the inward turning designs, could be compared. These comparisons may be able to quantify effects of geometry such as corner effects and non-traditional cross-sections on combustion efficiencies and qualities. A thorough explanation of the geometry tested as well as the testing conditions and results can be found in chapters 3-5 of this thesis. The following sections will develop the theoretical and experimental background of both aims of this study in more detail.

1.2 Scramjet Combustion Issues

In a typical scramjet powered vehicle design the flow path reduces the flight Mach number to approximately one-third once the flow has reached the combustor entrance[19]. Based on their simplistic analysis, Mach numbers at the combustor entrance would be approximately 2-3 for a flight Mach number of 6[20]. Their analysis establishes the interest area of combustion Mach numbers for the low end of the hypersonic spectrum. Within this spectrum a general consensus is that storable JP-type hydrocarbon fuels can be used[21]. Hydrocarbon fuels provide benefits in terms of energy density and handling issues in comparison to hydrogen fuels[22]. For these reasons a combination of gaseous hydrogen and hydrocarbon fuels were utilized in these investigations. It should be noted, however, that higher flight Mach numbers will most likely require the use of gaseous or liquid hydrogen due to its higher heating value as well as the possibility of using it for active cooling.

1.2.1 Mixing

At the combustor Mach numbers described in the previous subsection a key issue is the residence time of the fuel and air mixture within the combustor, which is often shorter than the ignition delay time of hydrocarbon fuels. In order for a reaction to occur, the fuel and air first must mix on a macroscopic scale then molecular collisions must occur which lead to the overall heat release and combustion[23]. Therefore the overall combustion time is simply the sum of the times of chemical

reaction (including the ignition delay) and the mixing time:

$$t_{combustion} = t_{chem} + t_{mixing} \quad [1]$$

The chemical reaction can be viewed as occurring in two phases. The first is an induction phase where intermediate radicals are produced and then an exothermic reaction in which the products are produced[24]. The first stage incorporates the ignition delay time and is a function of the fuel and the fuel to air ratio. This is typically defined by the fuel to air equivalence ratio: ϕ (which is the ratio of fuel/oxidizer divided by the stoichiometric fuel /oxidizer ratio), and the kinetics of the fuel itself. This induction phase makes up the majority of the chemical reaction time, and is considered to be long for hydrocarbon fuels. However, ignition delay times are much shorter than the mixing time. Therefore, the combustion time and mechanism is dominated by the time taken by the macroscopic fuel-air mixing.

Typically, in flight conditions create high static temperatures in the combustor which can lead to auto-ignition or very low energy addition needed to initiate the chemical reactions. In a report by Cain[25], studies were reviewed that demonstrated the flame speeds produced by these reactions are very slow in comparison to the flow velocity in the combustor, often an order of magnitude smaller. For this reason flameholding in the traditional sense appears impossible and combustion induced turbulence or subsonic pilots (or pockets) are necessary for maintaining combustion.

1.2.2 Heating

A major area of concern when a hypersonic vehicle design is being considered is that of thermal management. As flight mach numbers increase past Mach 4 the ambient air temperature relative to the aircraft is too hot to utilize ram air as an effective cooling mechanism[26] . Even when designs are considered for the lower end of the hypersonic realm, in the range of Mach 6-8, these material limits and thermal protection are major concerns. One specific location of concern is the isolator and combustor as airflow with already high static temperatures, above approximately 900K, is reacting exothermically with fuel being injected. The need to cool the surface walls of the combustor can become a very demanding requirement as flight Mach numbers increase. Conservative estimates have predicted that the fuel cooling requirements (for a fuel cooled system) will exceed the combustion requirements of the system by as much as 4 times for a Mach 20 flight system, meaning that 4 times as much fuel is required for cooling as is required to power the vehicle[26]. Naturally this increase of needed fuel flow along with the associated plumbing and systems will dramatically affect the flight weight of such a system. For these reasons an area of interest is reducing the overall Thermal Protection System (TPS) weight.

A direct method of reducing this weight would be by reducing the effective area needing to be cooled by the TPS. When a comparison of isolator/combustor cross sections is made between planar and inward turning inlets, the advantages of these novel geometries are clear.

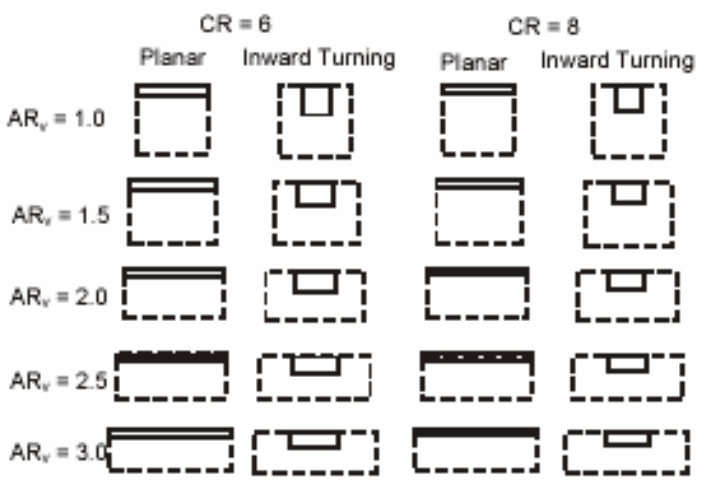

Figure 1.2 Comparison of Isolator/Combustor Cross Sections of Planar and Inward Turning Inlets from Billig[27].

In Figure 1.2, from Billig[27], the cross sections of planar and inward turning designs are compared. The diagram shows designs for two Contraction Ratios (CR) and various Aspect Ratios (AR_v) where the Aspect Ratio is the width divided by the height of the projected area of the maximum air capture streamtube. The comparison demonstrates that the planar designs would have larger wetted areas and lead to heavier designs.

By reducing the wetted area the need for TPS would also be reduced, further amplifying the weight advantage of the inward turning designs. One last consideration is the drag and heat transfer on the cowl. Both of these parameters vary with $\cos^N\nu$ where N is 1.5-2 and ν is the sweep angle[27]. Thus the more deeply vented, streamline traced, or inward turning designs are more favorable under this analysis when it comes to the drag and heating on the cowl. Therefore, when the

heating loads on a hypersonic vehicle design are considered these designs are of interest and more experimental testing to explore their specific attributes would be advantageous.

1.3 Objectives

The motivation for this study is established in the previous sections by outlining the current issues apparent in developing hypersonic vehicles, and specifically in the design and performance of their propulsion systems. There are two areas of interest in this investigation: the quantification of fuel-air mixing enhancement utilizing acoustically open cavity resonance, and the characterization of supersonic combustion in a diverging section with an aspect ratio of one.

The objectives of the mixing enhancement experiments are to obtain qualitative and quantitative measurements of the phenomena utilizing novel diagnostic techniques. To do so both high-speed and time averaged Schlieren imagery was utilized with the objective of obtaining instantaneous images of the vortical structures and averaged fuel injection trajectories, respectively. Dynamic pressure measurements were acquired to confirm the systems agreement with previous studies and the Rossiter model, which will be explained in later sections. Also, the LIBS technique was applied with the goal of obtaining a quantitative fuel-air ratio measurement at various locations in the flow. The final goal was the demonstration of the LIBS system in a real-world application.

The objective of the combustion characterization study was to establish a

baseline set of data points for the behavior of the specific combustor configuration. This included static pressure measurements as well as visual imagery and OH* chemiluminescence. This baseline is necessary to enable further experimental study of non-traditional geometries as applied to novel hypersonic vehicle designs such as the inward turning inlet. The baseline may also serve in the future as a validation for a computational fluid dynamics code as applied to this system.

The significant contributions of these experimental studies are:

- High speed Schlieren images were obtained for the cavity mixing enhancement studies which conclusively show coherent structures convecting downstream from the cavity. Pervious phase-locked Schlieren images inferred this convection of structures; however these high speed images capture multiple structures at various downstream locations at one instant in time.
- Laser Induced Breakdown Spectroscopy was applied for the first known instance to supersonic flow conditions for the cavity mixing enhancement studies. This diagnostic quantified the He/O ratio within the flow at multiple inspection points and revealed trends in the flow previously un-detectable by simple optical methods.
- Time averaged Schlieren images were analyzed utilizing image processing software to plot the average fuel injection for the cavity mixing enhancement studies. This tool is developed and shows promise in

analyzing qualitative Schlieren images to produce quantitative comparisons of average properties.

- A supersonic combustor was designed, fabricated, and installed on the reacting flow stand in Maryland's Advanced Propulsion Research Laboratory. No known supersonic combustion test bed has been previously developed at the University of Maryland
- Experiments show that for the given low enthalpy apparatus the prescribed staged fuel injection system is insufficient to promote reasonable supersonic combustion characteristics to represent a baseline for future experimental comparisons. A redesign of the fuel injection system and increases in the system enthalpy is recommended for future studies.

2 Theoretical Background

2.1 Compressible Mixing

2.1.1 Mixing Physics

In order for gas-phase chemical reactions to occur, the fuel and air must be mixed at the molecular level. To enable this process to occur the fuel and air must first undergo macromixing or so called near-field mixing, and then subsequently undergo micromixing (or far-field mixing). A thorough discussion of basic fuel-air mixing is presented by Heiser & Pratt[28] in their well-known textbook. Here the mixing of parallel streams is examined and classified into three separate regimes: Zero-shear mixing layer, Laminar shear/mixing layer, and Turbulent shear/mixing layer. The regimes are defined based on the difference between the two streams velocities or Δu, as Δu increases from zero the regimes progress as listed. A diagram of the parallel stream flows is presented in Figure 2.1 for reference. The "shear layer" is defined by the shear stress created between the two streams and the "mixing layer" is defined by the change in mole fraction of air or fuel by one percent from their respective values in the freestream.

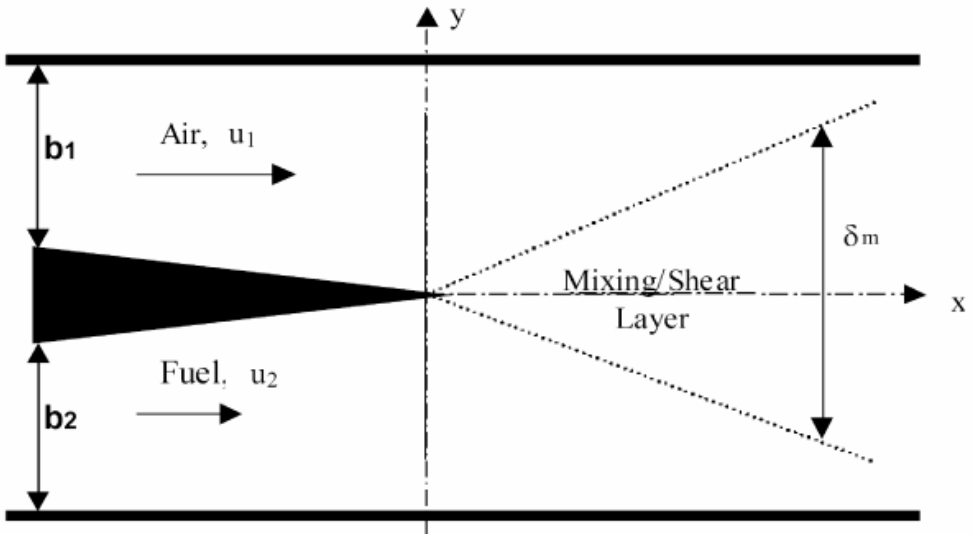

Figure 2.1: Parallel Stream Mixing/Shear Layer from Heiser & Pratt[28]

Corresponding equations for the mixing layer thickness can be found for the first two regimes in the aforementioned text. The third regime, turbulent shear/mixing layer, occurs at high values of Δu and becomes an unsteady process as the flow goes from laminar to turbulent. This results in the shedding of large vortex structures, sometimes referred to as "roller bearings", which occur periodically. Gutmark, et al.[29] points out that the formation of these structures is initiated by the Kelvin-Helmholtz instability, governed by Rayleigh's equation for inviscid flows. The exponential growth of the velocity and vorticity perturbations leads to a nonlinear process that eventually causes the roll-up of the shear layer into vortices, which are then shed. These structures are utilized in numerous mixing enhancement techniques.

Further studies of turbulent mixing, specifically focused on the turbulent shear layer, were conducted by a number of authors[30-34]. One of the earliest and most

prominent studies was conducted by Brown and Roshko investigating the density effects and role of large structures in turbulent mixing layers[30]. This investigation established compressibility as the main factor controlling supersonic turbulent mixing layers. The authors also determined this effect was uncoupled from density ratio and velocity ratio, which have significant effects on the growth of incompressible shear layers. In fact, for the same velocity and density ratios it was shown that the compressible case deviated ten times the amount the incompressible case as compared to a baseline uniform density incompressible case. Clearly compressibility effects are extremely important in the development of mixing in supersonic flows.

Brown and Roshko also developed an important parameter which is utilized by practically all subsequent studies in this area. This parameter is the convective velocity, U_c, which is defined as the speed of a point traveling with the large structures formed in the shear layer. Further study into the compressible turbulent shear layer was conducted by Papamoschou[33] and Papamoschou and Roshko[34] in which this parameter was revisited and a series of convective terms were defined. First let us consider a stagnation point on an infinitely thin shear layer structure between the two parallel flows. This point moves downstream with a velocity, defined hereafter as the convective velocity U_c. This definition is explained graphically in Figure 2.2 (a) in the stationary frame of reference and in (b) the convective frame of reference.

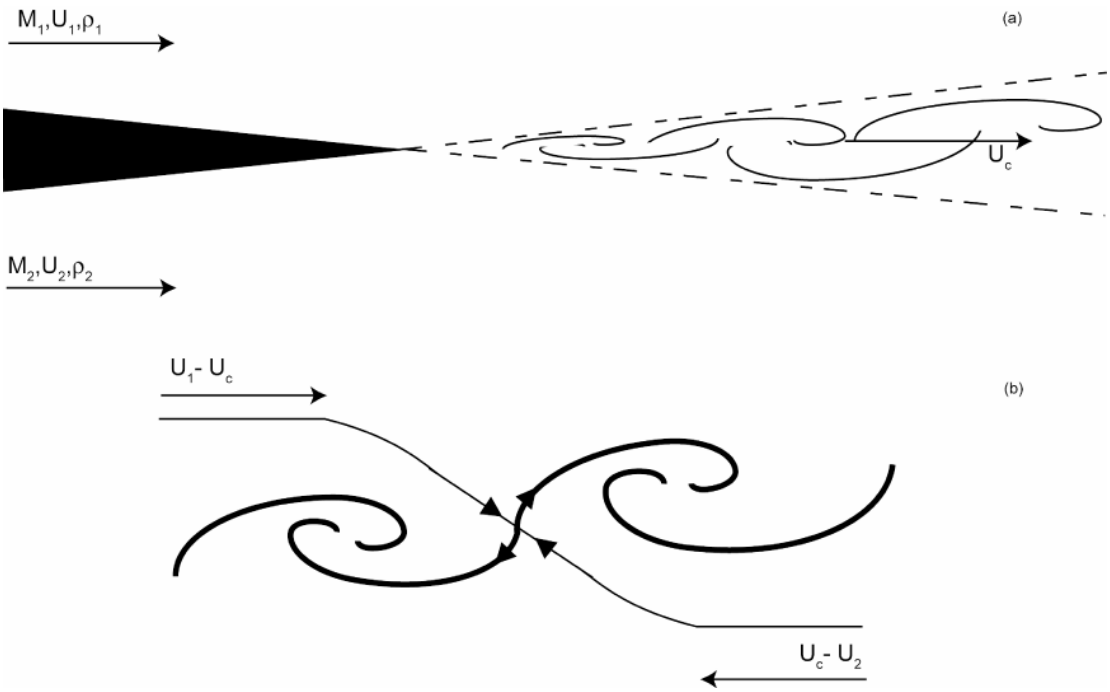

Figure 2.2: Turbulent Shear Layer in a.) Stationary frame of reference b.) Convective Frame of Reference with Streamlines

From this definition the convective Mach number is defined:

$$M_{c1} = \frac{U_1 - U_c}{a_1} \quad , \quad M_{c2} = \frac{U_c - U_2}{a_2} \qquad [2]$$

At the stagnation point these relations can be equated by:

$$\left(1 + \frac{\gamma_1 - 1}{2} M_{c1}^2\right)^{\frac{\gamma_1}{\gamma_1 - 1}} = \left(1 + \frac{\gamma_2 - 1}{2} M_{c2}^2\right)^{\frac{\gamma_2}{\gamma_2 - 1}} \qquad [3]$$

Which can be simplified by the assumptions that M_{c1} and M_{c2} are not very large, and that γ_1 and γ_2 are not greatly different to yield:

$$M_{c2} = \left(\frac{\gamma_1}{\gamma_2} \right)^{\frac{1}{2}} M_{c1} \qquad [4]$$

By utilizing the definition of M_c from equation [2] an equation for U_c can be related:

$$\frac{U_c}{U_1} = \frac{1 + \frac{U_2}{U_1}\left(\frac{\rho_2}{\rho_1} \right)^{\frac{1}{2}}}{1 + \left(\frac{\rho_2}{\rho_1} \right)^{\frac{1}{2}}} \qquad [5]$$

Lastly for the case of equal γ ($\gamma_1 = \gamma_2$),

$$U_c = \frac{a_2 U_1 + a_1 U_2}{a_1 + a_2} \qquad [6]$$

It is this convective velocity and Mach number which are used as a reference parameter in practically all the investigations into mixing enhancement, and turbulent mixing in scramjet engine applications. Seiner, et al.[6] summarizes Papamoschou and Roshko[34] results by explicitly relating the reduced shear layer growth at compressible speed to incompressible shear layer growth as:

$$\frac{C_\delta}{(C_\delta)_o} = \frac{C_\delta a_1 M_c}{const(U_1 - U_2)} \qquad [7]$$

where C_δ is the change in shear layer growth over distance and $(C_\delta)_o$ is the incompressible growth rate. The constant is a function of their measurement technique and was found to be 0.14 for Pitot tube measurements and 0.17 for shadowgraph visualization measurements.

Thus compressibility effects were quantified and the problems related to

mixing of supersonic compressible turbulent streams outlined. Through these studies the need to increase the shear layer growth in turbulent compressible flows was made clear if supersonic combustion was to be enabled. For this reason a variety of techniques to either excite or manipulate the properties of the compressible turbulent mixing layer have been explored and proposed.

2.1.2 Techniques of Mixing Enhancement

Two primary categories can be defined in reference to the techniques of controlling the turbulent compressible shear layer and thus controlling supersonic mixing. The first is active control in which mechanical or physical means of controlling the flow is actively controlled. A major issue with active control techniques is understanding the time-dependent behavior of the supersonic flow as well as the added weight and complexity of actuators or systems. The second is passive mixing enhancement in which a geometrical device is placed in or adjacent to the flow in order to tailor the flow to produce the desired results. The second strategy seems to offer more robust operation due to its lack of moving parts and relatively low weight penalties.

A number of authors[6,29] have compiled overviews of numerous techniques, both active and passive, to enhance mixing for scramjet application. These techniques all attempt to excite the turbulent shear layer to increase its growth[35]. Some examples of active techniques include vibrating splitters/wires, pulsed jets, Helmholtz resonators, piezoelectric actuators, and direct acoustic excitation[6,8].

Although these devices offer, in theory, better control of the mixing layer over a variety of conditions their penalties are also great in terms of weight addition and complexity. Furthermore, most of the actuation systems do not have significant enough forcing authority to achieve favorable results over a wide range of conditions[35]. For this reason passive techniques have often been viewed as the more favorable method. These techniques include ramp fuel injectors, tabs, lobe mixers, chevrons, swirlers, counterflow, rectangular injectors, steps and cavities[6,8]. Of these techniques the use of cavities has been extensively investigated and shown to have promising effects[36].

Another concern which is directly linked to mixing enhancement is the fuel injector geometry. Although various injector designs have been considered a bulk of the current work has been performed on wall injectors because of their low pressure losses and drag, as compared to intrusive injectors like strut injectors. In consideration of a single wall injector port there are two extremes of orientation: normal (or transverse) and parallel injection. Parallel injection follows the theory presented in previous sections, however a major issue with parallel injection is that it is essentially impossible to achieve near-stoichiometric mixtures in the near-field[28]. For this reason transverse injections were studied. A simplified model of the flow characteristics can be envisioned as a cylindrical rod being inserted into the supersonic flow.

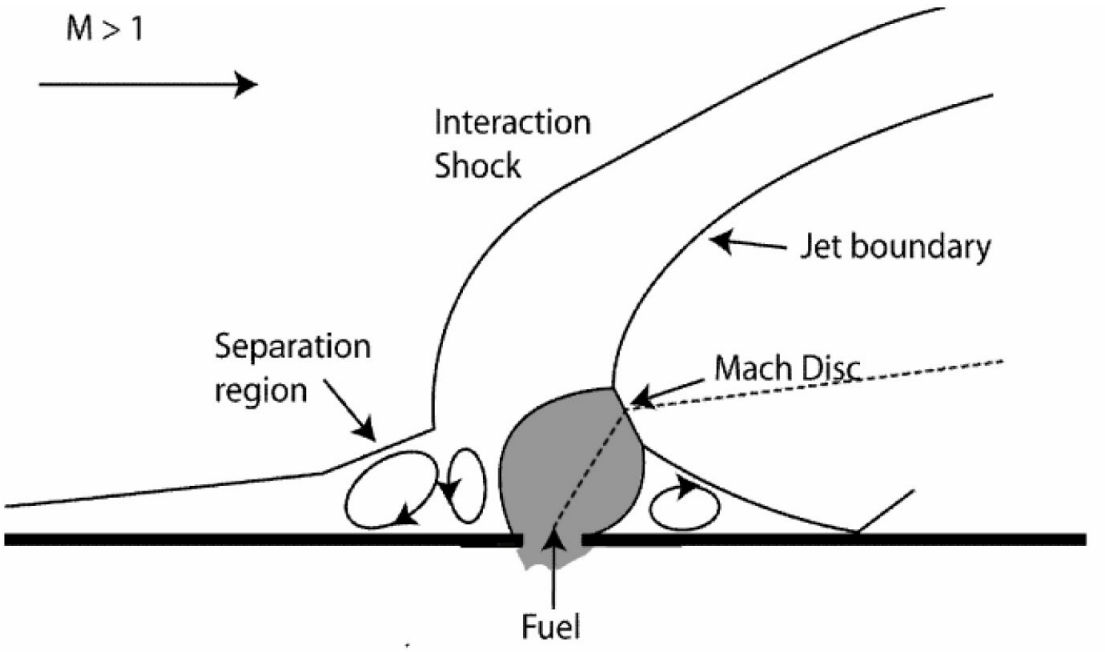

Figure 2.3: Transverse Fuel Injection into Supersonic Flow, adapted from Heiser, et al.[30], and Ben-Yakar, et al.[37]

A diagram of typical normal fuel injection flow fields is presented in Figure 2.3. Here it can be seen that the upstream boundary layer separates, and a detached bow shock is created upstream of the injector. A small recirculation zone forms upstream of the injected fuel stream, which can act as a flame holding region[37]. A bluff-body wake region is formed immediately downstream of the jet core, which can also be utilized for flameholding[28]. The overall effect is to reduce the mixing transition distance by anchoring the mixing layer firmly to the jet core. This reduction actually drives the distance past zero to a slightly negative mixing distance (in the near-field) due to the separation region upstream of the injector, as fuel diffuses upstream[28]. These mixing advantages are accompanied by significant stagnation pressure losses

due to the strong three-dimensional bow shock formed in front of the fuel injection. These losses increase with flight velocity, which is also very undesirable. Thus experiments have been performed utilizing angled injectors between these extremes[7,38-40]. These studies have sustained combustion and investigated various aspects of supersonic combustion control at high enthalpy conditions. Ben-Yakar, et al.[37] points out, however, that numerous studies have shown that at lower enthalpy conditions ignition occurs much farther downstream with angled injection as compared to the transverse case. Therefore, with the primary goal being to shorten the combustor length and increase near-field mixing transverse injection may be the preferred injection configuration.

Further mixing, however, is still required and excitation of the shear layer by cavities has been shown to be a promising technique. For those reasons a combination of normal injection and cavity excitation may produce significant reductions in mixing length.

2.1.3 Cavity Mixing Properties

Cavity flow fields have been a subject of great interest in aerodynamic research. Traditionally this research was focused on subsonic flows associated with store separation, wheel well acoustics, and pitching motions due to surface pressure variations[41]. The observed generation of coherent structures, however, brought interest into the supersonic regime in the form of passive mixing enhancement. There have been many studies to date which have investigated the flow field acoustics of

cavities at supersonic speeds [37,41-43]. These studies have the goal of exciting the resonance of the cavities whereas the previous subsonic work aimed to suppress the oscillations.

Cavities have shown promise in these experiments, as compared to other enhancement techniques. When the compressible shear layer growth rate is considered, as defined earlier by Papamoschou and Roshko[34], a method of comparing the effectiveness of excitation is developed. Figure 2.4, from Yu et al.[38], shows the comparison of results from a variety of authors for planar shear layers, natural axisymmetric shear layers, and the cavity excited shear layers. Here it can be seen that as convective Mach number increases past 1 the shear layer growth rate reduces asymptotically to 20% of its incompressible value. It can also be seen that increases of up to 3 fold in the growth rate can be achieved by cavity resonance.

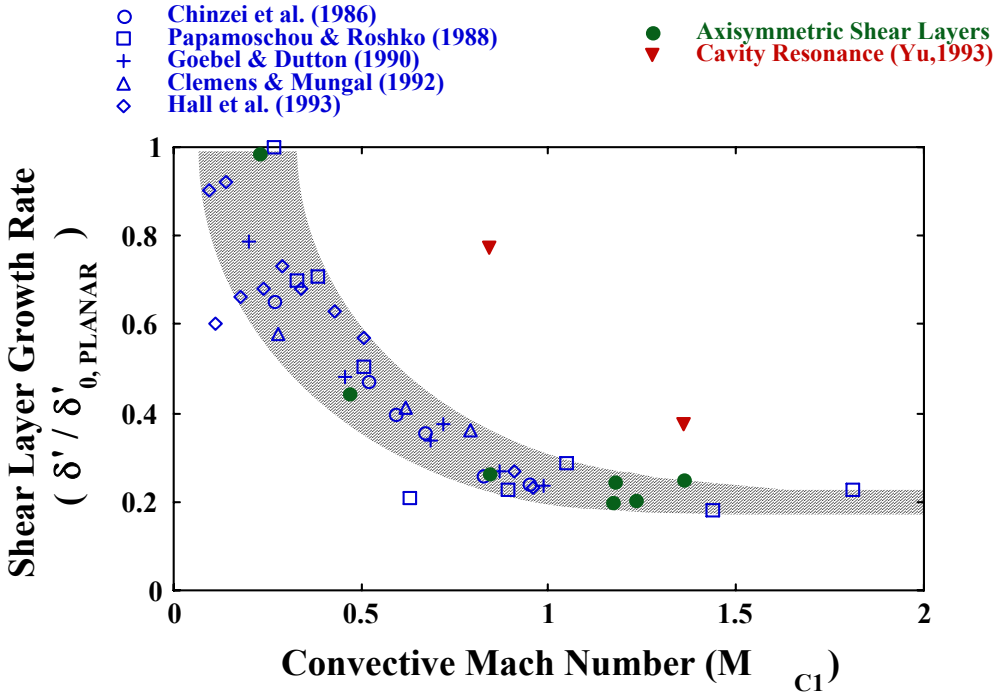

Figure 2.4: Normalized Growth Rate of Natural and Excited Shear Layers from Yu et al.[38]

For these potential benefits cavities have become one of the leading supersonic mixing enhancement techniques for scramjet applications.

2.1.3.1 Cavity Physics

Cavities are defined by a few geometrical parameters: length (L), depth (D), inlet height (H), and width (W). These parameters are usually expressed in the form of ratios such as the length-to-depth L/D (or aspect ratio), width-to-depth W/D, etc. Cavities are usually divided into two categories based on their aspect ratios and resulting flow characteristics. Open cavities are defined as having small enough aspect ratios as not to allow the shear layer to reattach to the cavity floor[37,38].

Typically L/D ratios less than 7-10 are considered open cavities. Cavities with aspect ratios larger than 10 are considered closed cavities because of the reattachment of the shear layer to the cavity floor. The mechanisms governing the flow oscillation change from transverse to longitudinal as the L/D ratio goes from less than 2 to more than 3. This mechanism, as well as the definition of open and closed cavities is illustrated in Figure 2.5.

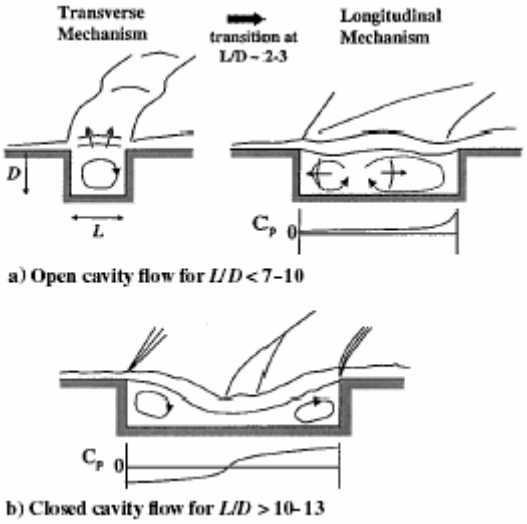

Figure 2.5: Flowfield Schematics of Different L/D Cavities in Supersonic Flow from Ben-Yakar, et al.[37]

It has been shown that cavity drag is proportional to L/D, in that as L/D increases so does the associated cavity drag. Furthermore, it has been observed that smaller aspect ratio cavities have better flame-holding characteristics than those with larger aspect ratios. It is for these reasons that acoustically open cavities which are driven by the longitudinal mode are becoming the preferred configuration for supersonic flow tailoring.

The mechanism of cavity induced resonance was first examined by Rossiter[44] who proposed that shear layer impingement on the trailing edge of the cavity would cause a pressure wave to travel upstream at the local speed of sound within the cavity. This wave would then travel to the leading wall of the cavity, upon which it would interact and cause another shear layer structure to roll off from the leading edge. Their structure would then convect downstream at U_c and impinge upon the trailing edge once again, closing the oscillation loop. A diagram of the flowfield over an open cavity is presented in Figure 2.6, and a diagram of the pressure wave oscillation and associated shocks is presented in Figure 2.7.

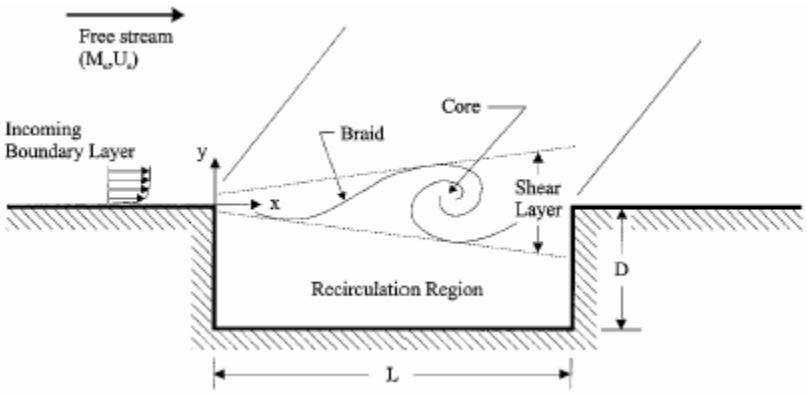

Figure 2.6: Schematic of a Compressible Two-Dimensional, Acoustically Open, Cavity Flowfield from Murry, et al.[42]

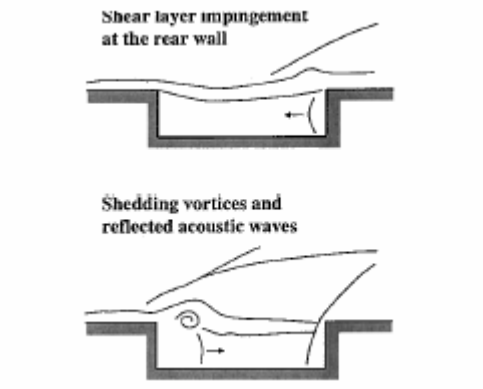

Figure 2.7: Longitudinal Cavity Oscillations Caused by Shear Layer Impingement from Ben-Yakar, et al.[37]

2.1.3.2 Rossiter Model

Rossiter developed a semi-empirical model to represent the resonant frequencies associated with the cavity oscillations[44]. His model was later modified by Heller and Bliss[45] to account for temperature differences inside and outside the cavity. Rossiter's model has three main terms, the downstream propagating wave frequency, f_n, the convection velocity κU (equal to U_c), and the acoustic propagation speed within the cavity called the phase speed c_p. To account for the temperature difference effects, the phase speed is replaced by the freestream speed of sound at the stagnation temperature[45]:

$$c_p = c_\infty \sqrt{1 + \frac{\gamma - 1}{2} M_\infty^2} \qquad [8]$$

The equations associated with this model are derived and discussed in many sources[35-39,42]. First let the fundamental period be taken to be the sum of the

disturbance convection time and the feedback time within the cavity and a possible phase delay term:

$$T = t_{convective} + t_{acoustic} + t_{phase} = \frac{L}{\kappa U_\infty} + \frac{L}{c_p} + \alpha \qquad [9]$$

where L is the characteristic length of the cavity and α is the phase delay. Typically the frequency is expressed in terms of the Strouhal number based on the cavity length[37]. This leads to:

$$S_{r_L} = \frac{f_n L}{U_\infty} = \frac{n - \alpha}{\frac{U_\infty}{c_\infty} + \frac{1}{\kappa}} = \frac{n - \alpha}{M_\infty + \frac{1}{\kappa}} \qquad [10]$$

where κ is the ratio of convective velocity to freestream velocity defined as:

$$\kappa = \frac{U_c}{U_\infty} \qquad [11]$$

and n is the wave number excited analogous to the excited mode, represented by an integer greater than unity. Equation [10] represents the original Rossiter model for cavity induced oscillations. Rearranged to solve for the frequency, which is predominantly the parameter of interest:

$$f_n = \frac{n - \alpha}{M_\infty + \frac{1}{\kappa}} \cdot \frac{U_\infty}{L} \qquad [12]$$

Heller et. al.'s[45] revision of the phase speed results in a slightly expanded form:

$$f_n = \frac{n-\alpha}{\left\{\frac{M_\infty}{\sqrt{1+\left(\frac{\gamma_\infty-1}{2}\right)M_\infty^2}}+\frac{1}{\kappa}\right\}}\cdot\frac{U_\infty}{L} \qquad [13]$$

where γ_∞ is the ratio of specific heats. Values of α and κ have been determined experimentally and from curve fit[42], but are still debated; the values are 0.25 and 0.57, respectively. Previous experiments in very similar laboratory settings[10] compared these values to those of experiment for flow conditions to be described in Chapter 3 of this thesis. The findings showed relative agreement with these empirical values within ± 3.5%. For the analysis to be presented in latter sections of this thesis the values of α and κ will be assumed as constants and the values presented here will be utilized.

2.2 Supersonic Combustion Characteristics

The main requirement in supersonic combustion is that the reaction rates which control the chemical reactions be very fast, so that the mixing of fuel and oxidizer can be a much slower process and therefore, be the controlling factor of the combustion[46]. To do so the induction time, or ignition delay time (t_{ind}), must be minimized. Supersonic combustion systems can be categorized by the flight mach number into two regimes: high flight Mach numbers and low flight Mach numbers. At high Mach number flight conditions, static temperatures and pressures are

typically high enough to auto ignite fuels like hydrogen. However at lower flight Mach numbers the static temperature and pressure are lower and combustion must be controlled by the transport of heat an radicals, as well as mixing. Often some kind of pilot flame is required[46]. The Mach number which divides these regimes is dependent on many factors including, but not limited to, fuel selection, geometry, flight altitude, etc. Traditionally a Mach number of approximately 6 or 7 is the dividing line between auto ignition systems and piloted systems. These considerations become especially important when low enthalpy ground testing is considered.

2.2.1 Staged Fuel Injection

Researchers conducting subscale tests of scramjet engines have encountered both ignition and flameholding problems due to the small scale of the models, the relatively low static temperatures and pressures, and the details of the combustion configurations themselves[47]. For these reasons, means of increasing the reactivity of the fuel and air are necessary. Creating high enthalpy conditions is possible via the use of preheated air generated by systems like vitiated heaters, pebble bed heaters, etc. However systems such as these require extensive hardware to compensate for the high temperature and pressure loadings. Additionally these systems are expensive and cumbersome, and often outside the realm of university level research. An alternate means to increase reactivity locally is to heat the air/fuel via means of a pilot flame. Encouraging results have been seen in the use of staged (multiple) perpendicular fuel injectors[47]. A diagram of a staged fuel injection system is

presented in Figure 2.8:

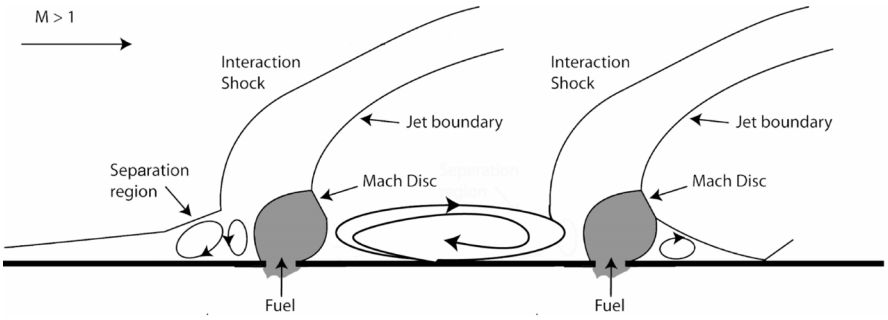

Figure 2.8: Schematic of Staged Injection Flowfield Adapted from Weidner[47]

Thus a flameholding device, such as this staged fuel injection, is necessary in completing supersonic combustion experiments at low enthalpy conditions. Due to the nature of novel geometries a flame holding device which does not affect the flowpath geometry would be preferred. For this reason a staged fuel injection scheme will be employed in the combustion experiments. This scheme will effectively shorten the ignition delay time which is discussed in the next section.

2.2.2 Chemistry

Ignition delay time is a direct result of chemical kinetics related to the given hydrogen or hydrocarbon – air reactions. These times can be determined by evaluating the chemical reaction rates for given conditions. This process is not trivial by any means and the validity of the calculations is wholly dependent upon the accuracy of the chemical mechanism selected, i.e. the elementary reactions which are considered as intermediate steps in the global reaction process. Numerical methods have been developed and software produced to model combustion reactions based on

inputs of reaction mechanisms, activation energies, and forward chemical reaction rates. Turns et. al.[48] presents a thorough investigation of the basic concepts and applications of chemical kinetics in combustion, including empirically determined parameters for many reaction mechanisms. A full investigation of chemical kinetics is beyond the scope of this thesis and the author refers readers to Turns' text for further investigation.

Studies have shown that the hydrogen-air induction time can be represented by empirical formulas as functions of pressure and temperature, from Heiser et. al.[28]:

$$t_{ind} = 4.5 \times 10^{-9} \left(\frac{p_o}{p} \right) e^{\frac{10^4}{T}} \qquad [14]$$

where t_{ind} is in seconds, temperature in degree Kelvin, and pressure in atmospheres. This gives a good first approximation for the delay time and provides insight into the combustion characteristics. To enable combustion, this time must be shorter than the mixing time. This is accomplished by increasing the mixing time by using subsonic recirculation regions or by decreasing the induction time by raising the temperature. Both of these are accomplished, in theory, by the staged fuel injection approach described in the previous section.

It should be noted that the CHEMKIN software package, or a similar combustion program, can be utilized to estimate induction and reaction times using chemical mechanisms based on elementary reactions. Inherent assumptions in the mechanisms and coefficient values will generate some uncertainty or inconsistency in the model; however approximate characteristics for temperature and reaction rates are

very useful in combustor design. Typically, the parameters calculated by such programs are almost impossible to measure directly within a supersonic flow field because of the hostile flowfield environment. Traditionally non-intrusive measurements are necessary to avoid shocks and pressure changes associated with intrusive probes. For these reasons static pressure ports along the combustor are the only direct measurement technique and predicted parameters are equated from these measurements.

2.2.3 Interpretation of Experimental Data

This subsection explains the use of static pressure port data, along with known combustor entrance conditions and geometries, to evaluate parameters along the combustor length including Mach number, temperature, and combustion efficiency. The method outlined here is presented in Heiser et al.[28] , and derived from papers by Billig[50,51], and Waltrup and Billig[49] . First consider a diagram of a generic combustor flowpath and the corresponding pressure gradient plot seen in Figure 2.9.

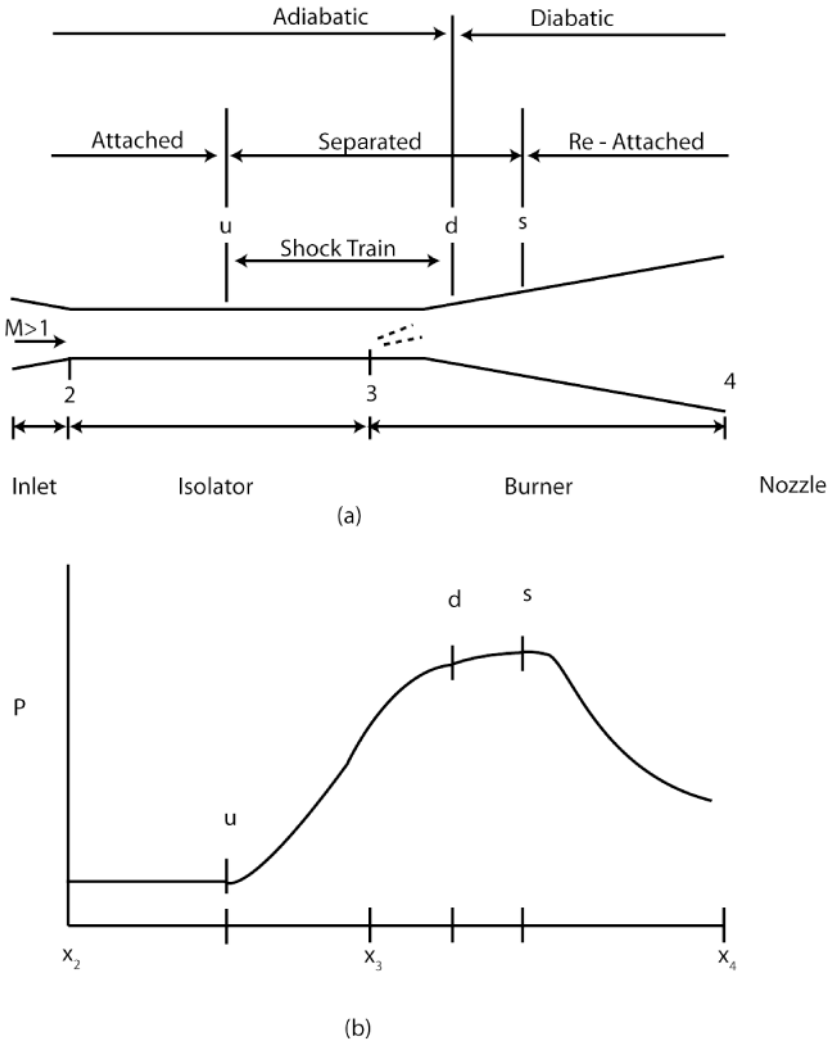

Figure 2.9: Designation of a.) Axial Locations for Combustion System and b.) Typical Static Pressure Distribution, from Heiser et al.[28]

The pressure distribution in this plot is idealized and realistic raw data would not present such a smooth curve. The initial step is to inspect the pressure distribution and determine the axial locations at which favorable or adverse pressure gradients occur. They are designated as x_u, x_d, and x_s, respectively. Next the data should be smoothed by curve fitting, as proposed by Waltrup and Billig[49]. Between stations u

and d the curve can be represented using a cubic polynomial;

$$\frac{p(x)}{p_u} = 1 + \left(\frac{p_d}{p_u} - 1 \right)(3 - 2\chi)\chi^2, \quad where \quad \chi \equiv \frac{x - x_u}{x_d - x_u} \qquad [15]$$

In the interval from station d to station s pressure is constant so p(x) = p_s = p_d , ideally. Any smoothing function can be used to fit from station s to station 4, Billig recommends:

$$pA^n = const. \qquad [16]$$

where

$$n = \frac{\ln[p(x_s)/\, p(x_4)]}{\ln[A(x_s)/\, A(x_4)]} \qquad [17]$$

Equation [16] has been determined empirically and values of p(x_s) and p(x_4) may have to be adjusted to obtain a best least square fit for all the intermediate p(x) data. Since the assumption was made that only pressure forces are acting on the external walls an evaluation of the stream thrust function can be used to find the Mach number as a function of axial location. The stream thrust function is defined:

$$dI = pdA \qquad [18]$$

For the change between two axial locations, x_i and x_e this equation can be written as:

$$I(x_e) = I(x_i) + \int_{x_i}^{x_e} p(x') \frac{dA(x')}{dx'} dx' \qquad [19]$$

This expression is based on the pressure at the walls and is valid whether or not the flow is separated or attached. Since the author is only considering a linear A(x) distribution equation [19] is evaluated and results in a quartic expression with respect

to pressure since p(x) is modeled by [15], for the expanding section of the duct. In the constant area section the stream thrust function is constant, i.e. since $A_e = A_i$ then $I_e = I_i$. For the range from x_s to x_4 equation [16] was utilized and the integrand in [19] reduces to:

$$\frac{p(x_e)A(x_e) - p(x_i)A(x_i)}{1-n}, \; n \neq 1 \qquad [20]$$

Once I(x) is determined M(x) is found from the definition of the impulse function:

$$I \equiv pA(1+\gamma_b M^2) \qquad [21]$$

thus

$$M(x) = \sqrt{\frac{1}{\gamma_b}\left[\frac{I(x)}{p(x)A(x)} - 1\right]\frac{A(x)}{A_c(x)}} \qquad [22]$$

In this equation A_c represents the core flow area, which is not equal to the duct area for the case of a shock train existing in the isolator. This creates adiabatic separated flow (from station u to station d). In this area the total temperature, T_t, is constant and known, $T_t = T_{r2}$, so that the core Area $A_c(x)$ is evaluated by equation [22] along with:

$$T(x) = T_2 \cdot \frac{T_t(x)}{T_{t2}}\left[\frac{1+\left(\frac{\gamma_b - 1}{2}\right)M_2^2}{1+\left(\frac{\gamma_b - 1}{2}\right)M^2(x)}\right] \qquad [23]$$

$$p(x) = p_2 \cdot \frac{A_2}{A_c(x)} \cdot \frac{M_2}{M(x)}\sqrt{\frac{T(x)}{T_2}} \qquad [24]$$

In the diabatic, attached region these two equations are used to evaluate T(x) directly

since A(x) is known. Thus in the diabatic, attached region and the adiabatic, detached region the properties are known based on the pressure distribution and the known state of the air at station 2. For the region from x_d to x_s where the flow is separated and diabatic any simple smooth function could be used to intersect $T_t(x_d)=T_{t2}$ to $T_t(x_s)$ and approximately determine the properties within that section. To do so the differential forms of the conservation equations and [16] are combined:

$$\frac{dT_t}{dx} = \frac{T_t}{A}\left[\frac{1+\frac{n(1-M^2)}{\gamma_b M^2}}{1+\frac{\gamma_b-1}{2}M^2}\right]\frac{dA}{dx} \qquad [25]$$

Combined with:

$$P_t(x) = P_{t2}\cdot\frac{p(x)}{p_2}\left[\frac{T_2}{T(x)}\frac{T_t(x)}{T_{t2}}\right]^{\frac{\gamma_b}{\gamma_b-1}} \qquad [26]$$

$$u(x) = u_2\cdot\frac{M(x)}{M_2}\sqrt{\frac{T(x)}{T_2}} \qquad [27]$$

the values of these properties can be determined along the length of the combustor. One more parameter of interest, the combustion efficiency $\eta_b(x)$, may be determined if the adiabatic flame temperature is calculated for a given equivalence ratio:

$$\eta_b(x) = \frac{T(x)-T_\sigma}{T_{AFT}-T_\sigma} \qquad [28]$$

where T_σ is the mass-averaged static temperature of both fuel and air streams at burner entry, and T_{AFT} is the adiabatic flame temperature.

Thus a fairly straightforward analysis can be performed to analyze the static pressure data for a given combustor and infer the temperature, Mach, velocity, and combustion efficiency profiles. These parameters are key in characterizing a combustor flow, however additional information by means of visual measurements provide insight into the flowfield characteristics.

2.3 Diagnostics

2.3.1 Schlieren

Light propagating through a vacuum travels along straight lines or rays. These rays are deflected when light passes through a medium which does not have optical homogeneity, i.e. a medium where the refractive index is not the same everywhere. Many optical visualization techniques are based on this phenomenon, including that of Schlieren visualization.

The idea of utilizing ray deflection has been around for many years. Toepler is given credit as being the first scientist to develop the technique for observation of liquid or gaseous flow, in around 1860[52]. Since that time, these techniques have been utilized extensively and evolved. Typically Schlieren techniques are utilized to produce qualitative imagery, however recent investigations have begun to modify classical Schlieren techniques to obtain quantitative flow characteristics[53-55]. The current study utilizes classical Schlieren techniques with sophisticated optical collection technology to observe both qualitative as well as some quantitative

measures.

A typical Schlieren system consists of a light source, a collimating lens (or mirror), a collecting lens (or mirror), a diaphragm (or knife-edge), and the collection optics. Figure 2.10 shows a diagram of a typical setup. Light passes through the collimating lens to create parallel rays through the test section, and the collecting lens focuses the light on the detector which is usually some type of camera. The diaphragm is positioned at the focal point of the collecting lens to block any refracted light. In gaseous flows light is deflected by density gradients which have non-homogeneous indexes of refraction. These gradients occur across gas-gas interfaces, shocks in supersonic flow, and along boundary layers for example.

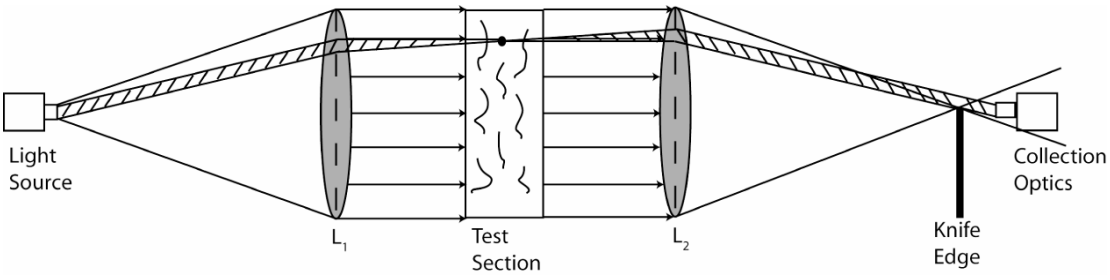

Figure 2.10: Diagram of Typical Schlieren Optics

The choice of diaphragm should be made with great care as it directly affects which direction of refraction is blocked and therefore which direction density gradients are detected in. Typically a knife edge is placed as the diaphragm so that light refracted in one direction is blocked while light refracted in the opposing direction passes. Blocked light appears as dark or bright areas on the Schlieren images dependent on diaphragm orientation. This method produces reliable results and provides qualitative

insight to the flowfield studied.

2.3.2 OH* Chemiluminescence

A wide range of sources for optical radiation from a flame or combustion system are available to use as analysis tools for combustion characteristics. The source most directly connected to the combustion reactions, however, is chemiluminescence[56]. Chemiluminescence appears when a certain chemical reaction in a chain of reactions mainly produces some molecules in an electronically excited level[57]. These molecules undergo transitions from higher to lower energy states that result in fluorescent emissions at specific frequencies depending on the molecule that has been excited. Such excited molecules or atoms have radiative lives on the order from 10^{-8} to 10^{-6} seconds[60]. The intensity of the resulting emissions is proportional to the production rate of the excited state species. In hydrogen-air reactions excited state OH (OH*) is produced by collisions with CH radicals and can be used to mark the location of the reaction zone. For this reason chemiluminescence has been used as a rough measure of reaction time and heat release rate previously[56].

OH* and CH* chemiluminescence has been utilized to study flame front structure[58], local equivalence ratio[59], and to monitor flame stability[56]. OH* chemiluminescence is of interest in the present studies due to its appearance in both hydrogen and hydrocarbon flames. Gaydon[60] discusses the sources of chemiluminescent OH* and sights four means of excited OH emission: i.) weak thermal radiation, ii.) weak anomalous excitation to higher vibrational levels (mainly

in hydrogen flames), iii.) strong excitation in reaction zones of hydrocarbon flames which lead to higher effective rotational temperatures and iv.) strong excitation in other flames not leading to high rotational temperatures (i.e. methyl alcohol, formaldehyde, etc.). In the present investigation the second and third mechanisms are those responsible for OH* generation. The reactions producing these OH* radicals are as follows:

$$CH + O_2 = CO + OH^* \quad [29]$$

in the hydrocarbon flame, and

$$H_2 + HO_2 = H_2O + OH^* \quad [30]$$

for the hydrogen flame. These chemical reactions occur near the areas of highest heat release and near the flame front in both types of reactions. Therefore obtaining OH* chemiluminescence images under combustion conditions would broaden the characterization of the reacting flowfield.

Chemiluminescent images can be obtained at visual wavelengths using appropriate narrow band interference filters to isolate the wavelength of interest. It should be noted, however, that at low wavelengths outside the visible spectrum intensified CCD cameras and special optical lenses may be required to obtain reliable signals.

2.3.3 Laser-Induced Breakdown Spectroscopy

Laser-Induced Breakdown Spectroscopy (LIBS) is an innovative method of

quantitatively measuring gas composition which can be used to measure local fuel to air ratios[61]. LIBS is an optical technique requiring no sampling from the flow. In LIBS a pulsed laser beam is focused onto a small point via a converging lens, creating a spark in the medium to be examined. The deposition of energy is enough to create a microplasma of roughly 0.1-1 mm^3 in volume[62], hot enough to dissociate molecules into their constituent atoms and excite the electrons in the neutral atoms and ions into higher electronic states[63]. The resulting temperature at short times (<10μs) is in the range of 10,000-25,000K. As the plasma cools, the excited electrons relax emitting light at characteristic atomic emission frequencies. That light is collected and recorded as a function of wavelength by a spectrometer. The total time for plasma formation and decay is on the order of microseconds, therefore providing rapid, in-situ analysis. Data obtained can be used to determine the elemental concentrations and ratios present in the measurement volume, which is defined by the volume of the plasma. Typical applications for the LIBS technique have been in the evaluation of waste emission analysis[63], environmental monitoring[61], and material processing. Characterization of supersonic turbulent flows has been previously been performed using hot wire or film anemometry (HWA) and laser Doppler velocimetry (LDV)[64]. However these techniques are invasive and have their individual shortcomings. The application of the LIBS technique to supersonic flow is novel, and could have a wide range of potential benefits.

3 Experimental Apparatus & Approach

3.1 Flow Facilities

Airflow for both the cavity induced resonance and supersonic combustion characterization were provided by an Atlas Copco Compressor. This compressor can achieve a maximum flow rate at its outlet of 358 cubic feet per minute at a pressure of 150 psi. It is a stationary screw type compressor which is oil injected and single stage. An electric motor provides power to the compressor. The compressor line is fed through a settling tank to remove sediment and/or oil deposited in the compressor air. It is then passed through a dryer which removes condensate by lowering the air temperature to near freezing. Finally the air is passed through a gas/air filter before being routed to the laboratory supply lines. These supply lines are mated to the individual rigs described in the subsequent sections.

3.2 Cavity Induced Resonance

The experimental apparatus to study the cavity induced resonance was set up on the non-reacting test bed in the Advance Propulsion Research Laboratory. A brief description of the overall setup is provided here to aid the reader in understanding the subsequent, more detailed, descriptions. Air flow is provided through a supply line, which undergoes a conical reduction and is then passed through a converging diverging nozzle. Flow velocity at this nozzle exit is approximately Mach 2.0. The

test section with optical access is placed directly after this nozzle and then the air is exhausted from an open end at atmospheric conditions. A rough diagram of this system is presented in Figure 3.1.

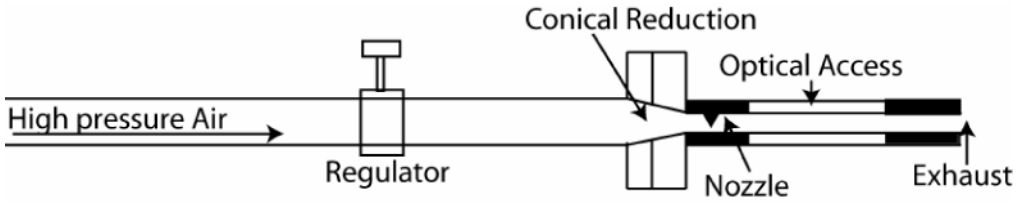

Figure 3.1: Basic Diagram of Cavity Mixing Test Apparatus

3.2.1 Hardware

The supply line described in section 3.1 from the gas/air filter is mated to a 2 inch diameter steel pipe and redirected into the laboratory. A ball valve is placed on this line, followed by a Wilkerson screw type regulator valve with an operating range of 0-180 psi. Mass flow and stagnation pressure upstream of the test section is controlled by this choked regulator. Pressure is measured directly after the regulator with a Setra Model 206 static pressure transducer with a range of 0-250 psi and monitored on a Datum 2000 dual channel display which was calibrated according to factory specifications. The test section is mated to the circular pipe approximately 7 feet downstream of this regulator by a 4.75 inch bolt circle adapter and two subsequent aluminum custom milled blocks. These blocks reduce the flow area from the circular supply line to a one inch square cross section. The first block (referred to as the transition block) serves as a conical reduction and the second block (referred to

as the front block) establishes a straight, square cross section and couples to the test section. Three-view CAD models of these two blocks is presented in Figure 3.2 and Figure 3.3.

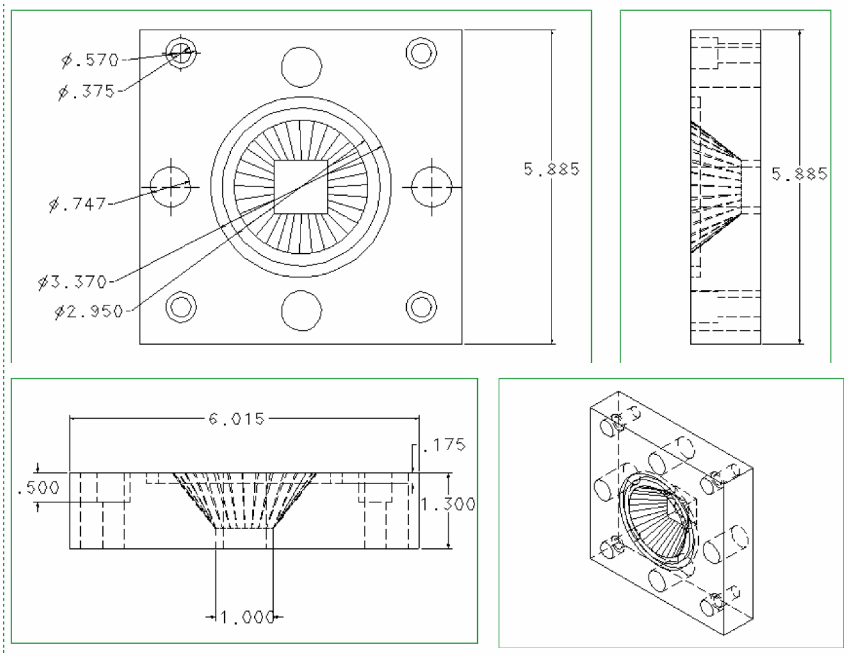

Figure 3.2: Transition Block Schematic for Cavity Mixing Rig

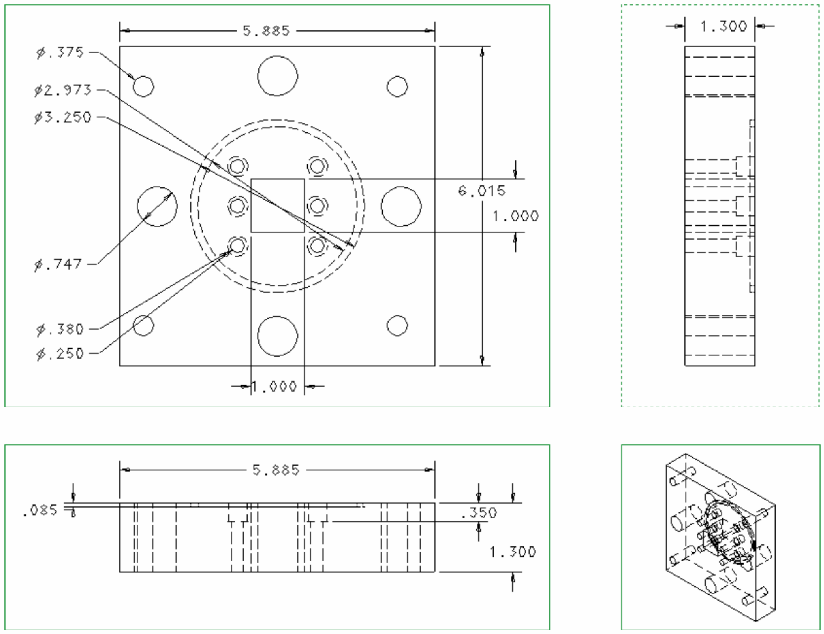

Figure 3.3: Front Block Schematic for Cavity Mixing Rig

The test section consists of two aluminum blocks, which make up the top and bottom test section surfaces, and two quartz windows held within stainless steel frames, which make up the sides of the test section. The frames, or window-holders, are directly connected to the front block and sandwich the top and bottom plate. These frames are milled from 316 stainless steel and allow an optical, line of sight, access 1.2 inches high and 11.8 inches long to the test section. They hold in place the quartz windows which measure 2 inches high and 12 inches long. The quartz windows can be replaced with aluminum plates with ports for dynamic pressure measurement. A schematic of one of the window holders is presented in Figure 3.4. Bolts are used to secure the window holders together with the top and bottom plate

held in-between the two window holders.

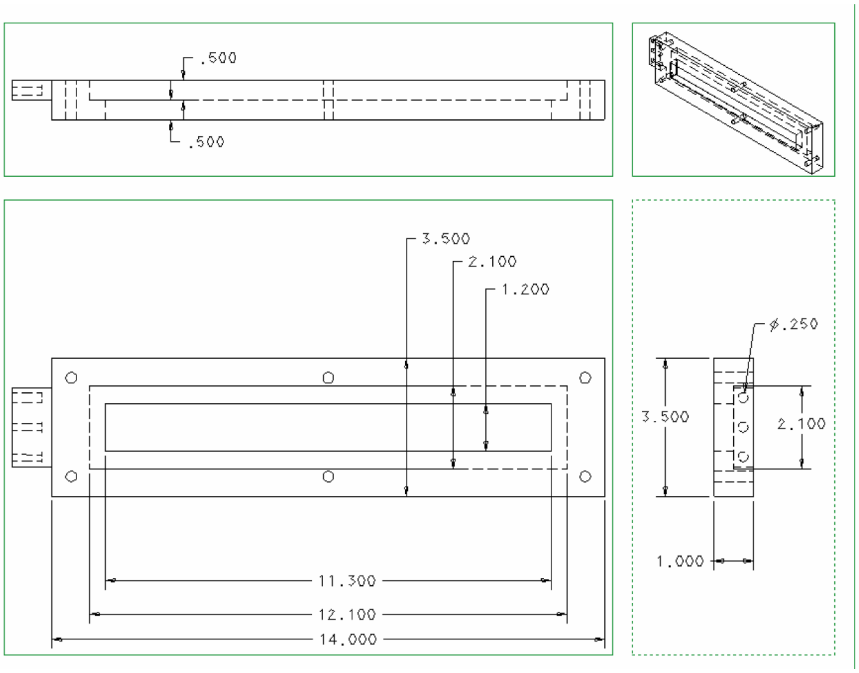

Figure 3.4: Window Holder Schematic for Cavity Mixing Rig

The top and bottom plate are milled from Aluminum Stock and measure one inch wide by sixteen inches long. The top plate has a constant angle converging section which terminates in a flat section 0.1 inches long, after which is the sharp-corner nozzle profile. This profile was developed by employing a simple two dimensional method of characteristics[65] written in the MATLAB software. A three degree expansion angle was placed downstream of the injection point (on the bottom plate to be described) to compensate for boundary layer growth in the duct. This expansion is based on previous experimental results and design[10]. The top plate is presented in Figure 3.5.

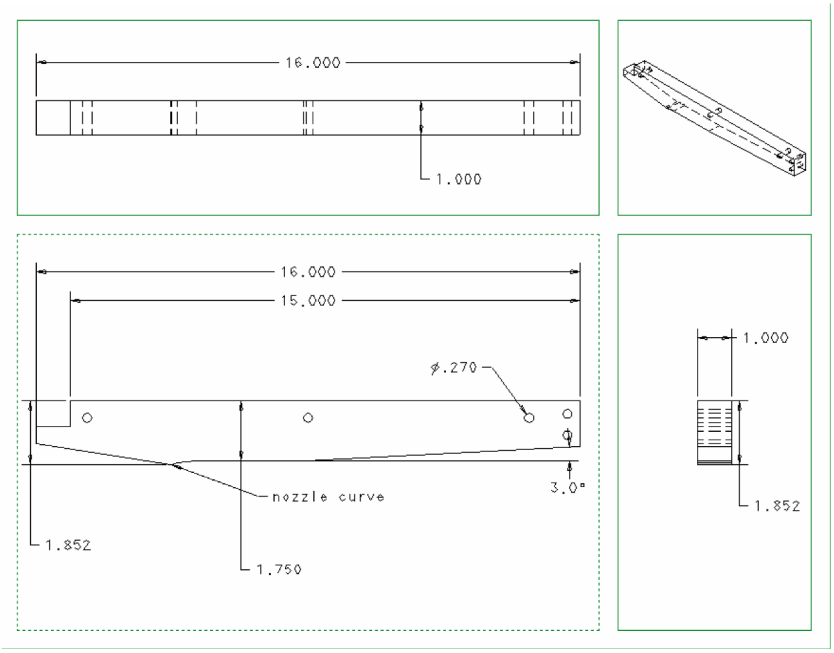

Figure 3.5: Top Plate Schematic for Cavity Mixing Rig

The bottom plate also has a constant angle converging section which terminates at the throat location corresponding to the short flat section preceding the nozzle curve on the top plate. From the throat to the exhaust the bottom plate has a flat profile for the baseline configuration. This plate was simply replaced to switch between the baseline configuration and the cavity configuration. An injection point is placed nine inches from the throat in both configurations, and measures 0.100 inches in diameter. The cavity bottom plate has a cavity recess cut from the aluminum at a location starting one inch upstream of the fuel injection. The cavity measures 0.5 inches long by 0.125 inches deep, giving the cavity an aspect ratio of 4. This aspect ratio was selected based on prior investigations into various cavity configurations and

their characteristics[10]. CAD drawings of these two bottom plates is presented in Figure 3.6 and Figure 3.7.

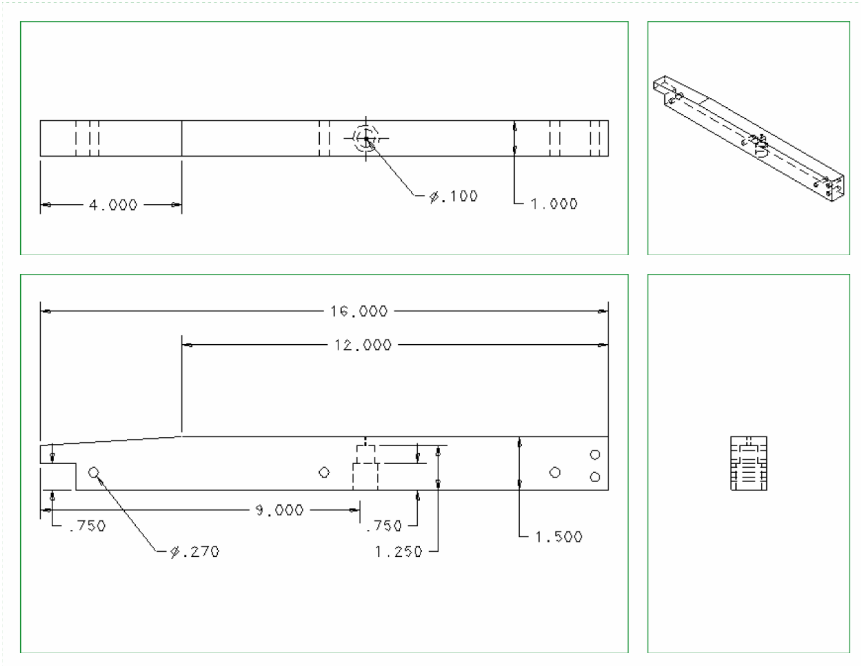

Figure 3.6: Baseline Configuration Bottom Plate Schematic for Cavity Mixing Rig

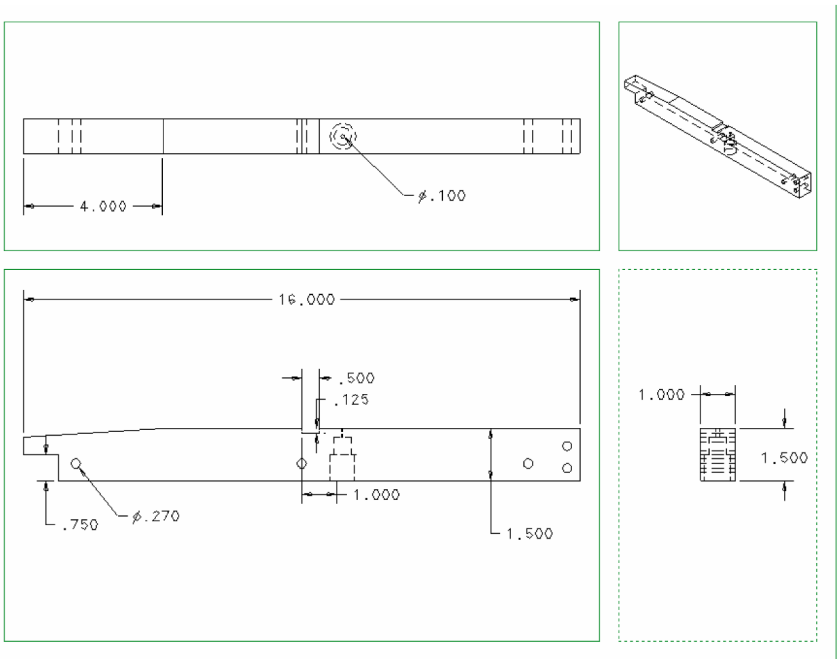

Figure 3.7: Cavity Configuration Bottom Plate Schematic for Cavity Mixing Rig

This hardware was utilized for all of the mixing enhancement experiments, with the only variation being the bottom plate for the corresponding baseline and cavity cases. An adhesive gasket material was used to seal the glass-metal interfaces as well as the connection of the front block and test section. O-ring seals were utilized between the supply line and transition block as well as between the transition block and the front block. A complete schematic of the assembled components is presented in Figure 3.8 for a more comprehensive understanding of the experimental apparatus. Additionally, a picture of the test section is shown in Figure 3.9.

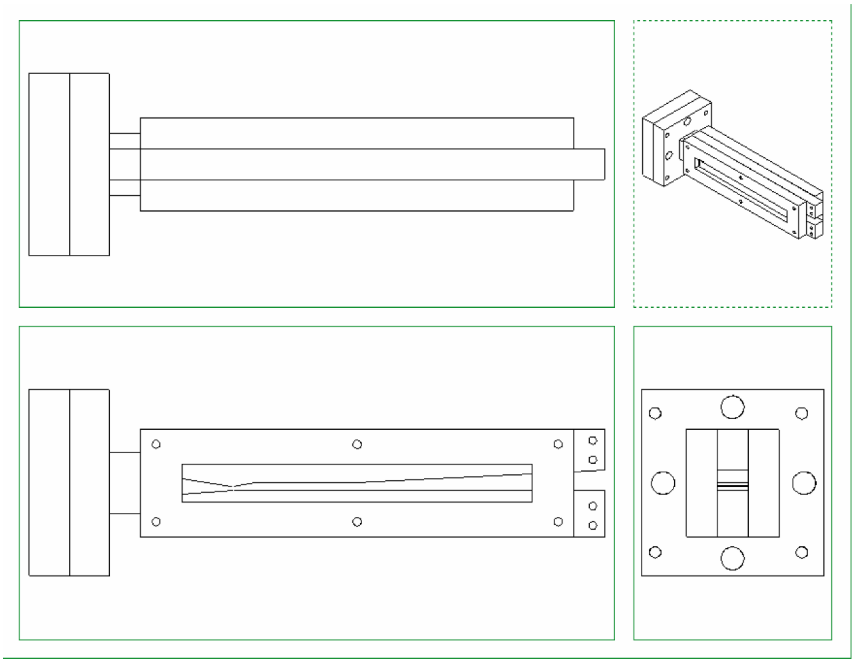

Figure 3.8: Cavity Mixing Test Section Schematic, Baseline Configuration

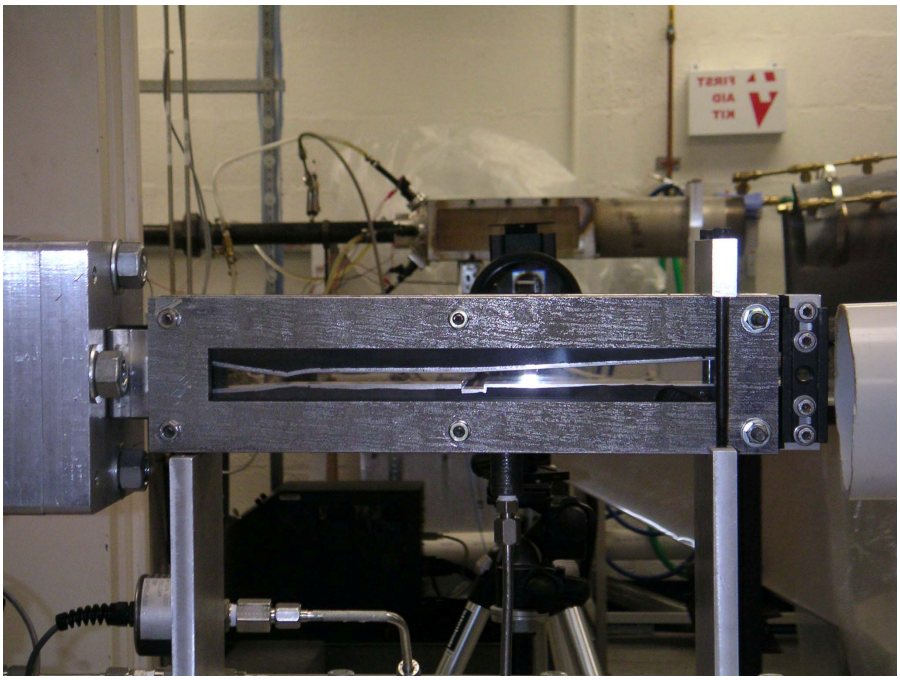

Figure 3.9: Close-up Picture of Cavity Mixing Test Section, Cavity Configuration

3.2.2 Diagnostics

3.2.2.1 LIBS

The LIBS system used in the cavity mixing experiments utilized the 1064 nm fundamental of a Nd:YAG laser to create the plasma spark. This laser was operated with an energy of approximately 400 mJ / pulse and monitored periodically throughout testing to detect any power drift. As shown in Figure 3.10, the laser beam is expanded from 5 mm to 22 mm, after which the beam is passed through the center hole of a pierced mirror and then focused into the test section via a 10 cm focal length fused silica lens. Light emitted from the plasma is collected back along the same optical path via the pierced mirror by achromatic collection system, which transmits the light via a UV-compatible optical fiber to an intensified CCD camera mated to a 0.3 meter spectrometer. Spectra are output to a desktop computer for analysis. For the application in the supersonic wind tunnel this apparatus was mounted on a movable cart and placed adjacent to the continuous flow facility. A picture of the LIBS system in place can also be seen in Figure 3.11.

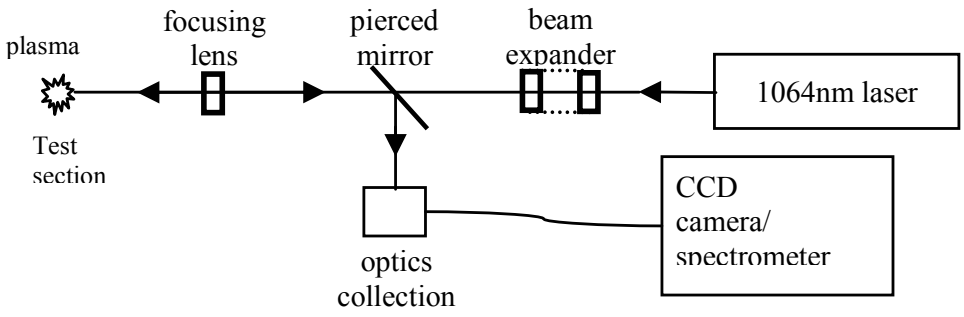

Figure 3.10: LIBS Diagnostics Schematic

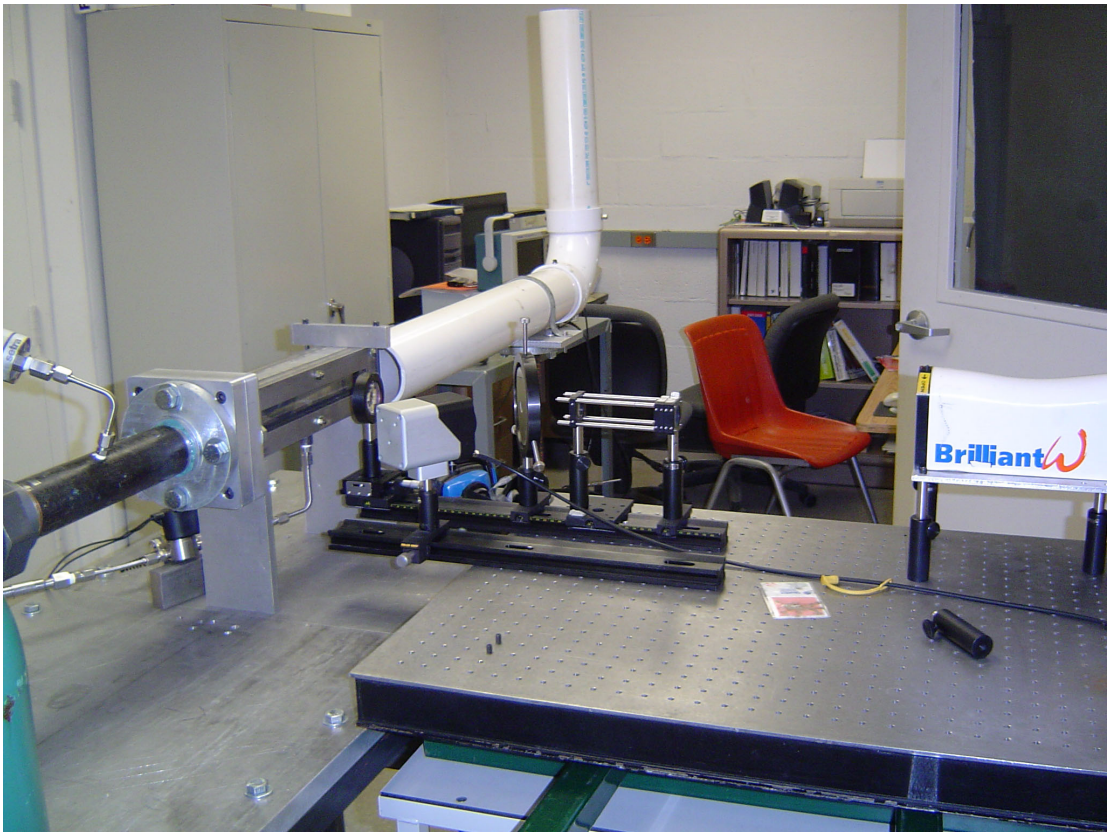

Figure 3.11: Picture of LIBS Apparatus placed perpendicular to test section

3.2.2.2 Schlieren

The Schlieren system used was a high speed Schlieren configuration consisting of a 10W continuous light source reflected by a six inch diameter concave mirror through the test section. The light was collected by an identical mirror perpendicular to the test section and passed through a radial Schlieren stop aperture. The mirrors have focal lengths of 60 inches and were placed as seen in Figure 3.12.

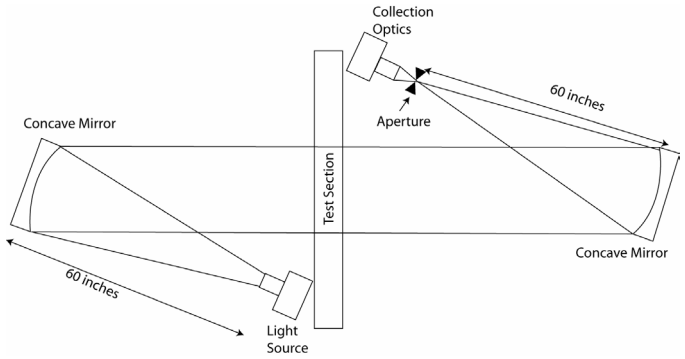

Figure 3.12: Specific Schlieren configuration for cavity mixing enhancement studies

A Photron Ultima 1024 CMOS camera was used to collect the filtered light from the Schlieren stop. A desktop computer and the Photron Fastcam software were used to capture and store the images. The camera has an acquisition rate of 60-16000 frames per second and shutter speeds from 0.016 to 7.8E-6 s. For the purposes of the current investigation the camera was operated over a range of 1-8000 fps and the full range of shutter speeds to produce both quasi-instantaneous and time averaged Schlieren images. These images were also analyzed using the image processing toolbox of MATLAB to plot the intensity maps as a measure of fuel injection and fuel spreading.

3.2.2.3 Dynamic Pressure

To investigate the oscillating pressure waves in the cavity, the quartz window was replaced with the instrumented aluminum plate discussed in 3.2.1. This plate was fitted with a flush mount dynamic pressure transducer located at the trailing edge of the cavity. The transducer was a Kistler 211B5 voltage mode dynamic pressure transducer with a measuring range of 0 to 100 psi and with a maximum pressure capability of 500 psi. This was mated to a Kistler 5010B dual mode charge amplifier and then fed into a National Instruments Digital Acquisition Center which interfaced with a LabView monitoring program. This program also saved the signal in data files which were subsequently loaded and analyzed in MATLAB. The signal was sampled at 1 Mega samples / second. Signals from 0 to 50 kHz were detectable based on this sampling rate and the Nyquist Criterion. A Fast Fourier Transform (FFT) was conducted on the data sets in MATLAB to identify the dominant frequency at the given flow conditions.

3.2.3 Experimental Procedure

Flow conditions were established by setting the upstream stagnation pressure for all of the cavity induced mixing experiments. This was done using the Wilkerson regulator and the pressure was recorded using the Setra Datum 2000 display. Once the air flow was established a helium injection was set to a specific pressure and controlled via an electronically actuated solenoid valve. This helium line was passed

through a 0.052 inch orifice to create a choked condition and to allow for mass flow calculations based on stagnation pressure. With both the fuel and air on measurements were then taken for the given diagnostics.

3.2.3.1 Schlieren and Dynamic Pressure Testing

Schlieren measurements were also performed once the air flow and helium pressures were established as outlined in Table 3-2. Both the cavity and non-cavity configurations were investigated at three optical conditions for the Schlieren testing. The optical conditions selected were:

Table 3-1: Optical Configurations for Schlieren Testing

Optical Configuration	Frame Rate (fps)	Shutter speed	Resolution	Lens
1	2000	1/64000 s	512 x 256	Zoom
2	8000	1/128000 s	512 x 64	Standard
3	60	1/60s	1024 x 1024	Zoom

The configuration corresponding to high framing rates and shutter speeds were assumed to produce 'instantaneous' images and are used to make qualitative observations of the cavity resonance phenomena. The low framing rate configuration produces time averaged images that were loaded into MATLAB as grey scale images with the intensity corresponding to a value from 0 (black) to 255 (white). These

images were then mapped for their intensity to infer quantitative information about the fuel injection trajectory. The image files were acquired as movie files and then split into individual images. The number of images and resolution were a function of the camera's available memory.

Dynamic pressure measurements were acquired for the same apparatus but were taken over a wider range of flow conditions. Air flow conditions from 20 to 100 psig were investigated with a tighter test matrix centered around the conditions where mode 'hopping' occurred. As mentioned previously these signal were also analyzed in MATLAB and compared to the theoretical predictions of Rossiter[44].

3.2.3.2 LIBS Testing

Preliminary testing encompassed a test matrix from 20-80 psig for Air and 20-60 psig for Helium. These tests were utilized to narrow the experimental test matrix to include three separate conditions for the two configurations, which were optimal for the LIBS testing. This produced a test matrix as follows:

Table 3-2: LIBS Testing Conditions

	Air Stag. Press	Air Mass Flow Rate	He Stag. Press	He Mass Flow Rate
1	20 psig (2.4x105 Pa)	0.051 kg/s (0.11 lb/s)	40 psig (3.7x105 Pa)	4.8x10-4 kg/s (1.1x10-3 lb/s)
2	20 psig (2.4x105 Pa)	0.051 kg/s (0.11 lb/s)	60 psig (5.2x105 Pa)	6.5x10-4 kg/s (1.4x10-3 lb/s)
3	40 psig (3.7x105 Pa)	0.081 kg/s (0.18 lb/s)	60 psig (5.2x105 Pa)	6.5x10-4 kg/s (1.4x10-3 lb/s)

At each test condition a set of 9 measurement locations were investigated using the LIBS diagnostics creating a total of 27 test locations in the matrix. As illustrated in Figure 3.13 , the nine test locations were at three streamwise (or x-direction) locations from the injection point: 6.3 mm, 31.7 mm, and 57.1 mm and at three spanwise (or y-direction) locations: 0 mm (centerline), +5 mm, +10 mm in this symmetric flow. Due to experimental constraints, the test location height (in the z-direction) was kept constant for all cases at 3.2 mm or approximately 3 injector diameters. The test matrix was then collected for both the cavity and non-cavity (or baseline) conditions.

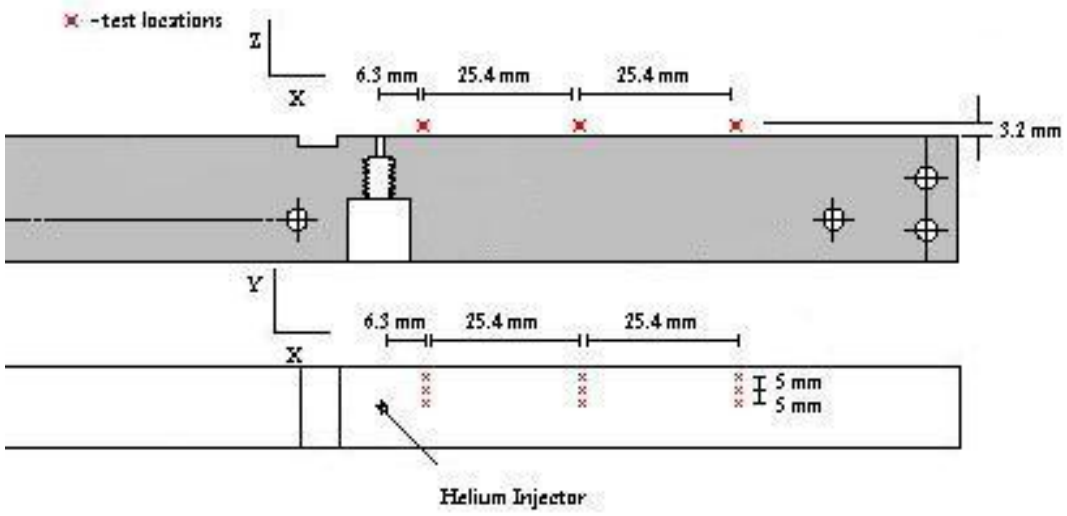

Figure 3.13: LIBS Investigation Points

LIBS data was collected for 100 single shot spectra and then averaged to produce a single measure of the He/O ratio. This parameter is the ratio of the integrated atomic emission peak of He at 588 nm to the integrated peak of O at 777 nm. Since the peak area is proportional to the number of atoms of a particular element present and the plasma volume is constant for each shot, this ratio represents the molecular concentration of helium, relative to air, within the test volume. The constant laser power allows the assumption of a constant plasma volume, as these are directly proportional. Laboratory experiments which were not conducted as a part of this thesis have proven the usefulness of the He/O atomic peak ratio for quantification of helium concentration[66].

3.3 Supersonic Combustion Characterization

Air was supplied via the same process as describe in section 3.1 via a 2 inch

diameter steel pipe for the combustion characterization experiments. This rig, however, was built on the reacting flow stand in the Advance Propulsion Research Laboratory. A general overview of the supersonic combustion apparatus is presented in Figure 3.14. Supply air is brought through a converging-diverging nozzle which accelerates the flow to Mach 2. A short straight section of duct follows this nozzle and then the duct is expanded in all three dimensions with a constant angle expansion. The fuel injection and pilot flame are placed just downstream of this expansion and optical access is provided by a quartz window on one side. The combustor is exhausted into the atmosphere and an active water cooling system is placed in front of the exhaust duct to protect the laboratory HVAC system. A detailed description of the components and diagnostic systems can be found in the subsequent sections.

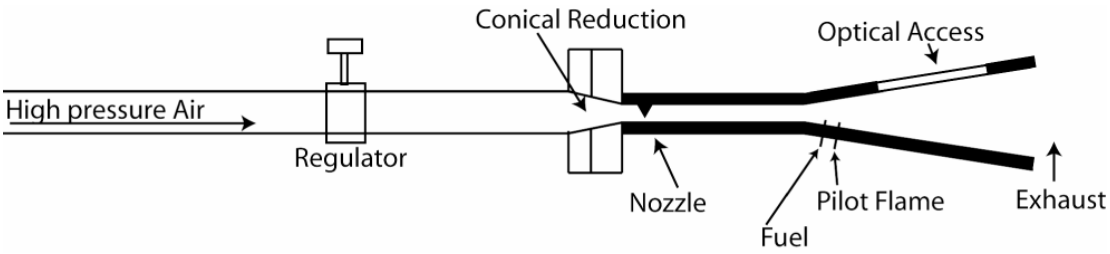

Figure 3.14: Basic Diagram of Supersonic Combustion Test Apparatus

3.3.1 Hardware

Similar to the configuration described in section 3.2.1, the 2 inch supply line is mated to a Wilkerson regulator which controls the upstream stagnation pressure and mass flow rate accordingly. Pressure is measured directly after the regulator with a Setra Model 206 static pressure transducer with a range of 0-250 psi and monitored

on a Datum 2000 dual channel display which was calibrated according to factory specifications. The test section is again mated to the circular supply line by a 4.75 inch bolt circle connected to two custom milled aluminum blocks. These blocks will also be referred to as the transition block and front block as described for the cavity mixing enhancement hardware. Although serving the same purpose the dimensions of these blocks are different than those of the cavity mixing rig. The transition block serves as a conical reduction of the flow from the circular pipe to a 0.5 inch square cross section. This is accomplished over a distance of 2 inches which is longer than the cavity mixing transition block length. A schematic diagram of the transition block is presented in Figure 3.15.

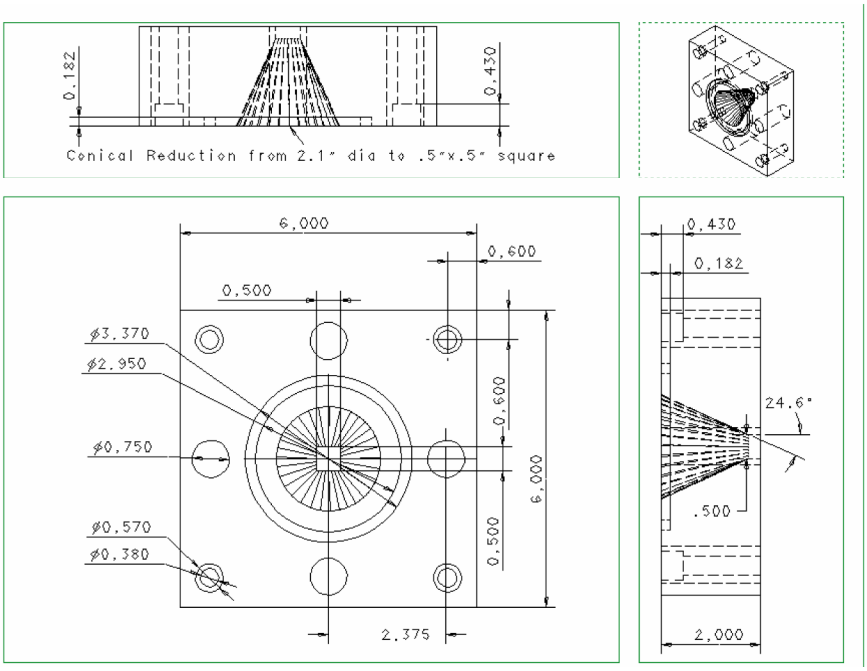

Figure 3.15: Transition Block Schematic for Supersonic Combustion Rig

The front block for the combustion characterization experiments mated the transition block to the combustor test section itself. This block had a square cross section flowpath with dimensions of 0.7 inches by 0.7 inches. The flowpath area is expanded to allow for the placement of a flow straightener in this front block section. The flow straightener is a stainless steel honeycomb material with length equal to 2 inches and hexagonal cells with cell sizes of approximately 0.005 square inches. The flow leaving the transition block, therefore, undergoes negligible expansion due to the flow straightener and enters the test section at the same area as the exit of the transition block. The intersection between transition block, supply pipe, and front block are all sealed via o-ring connections. A schematic of the front block is presented in Figure 3.16.

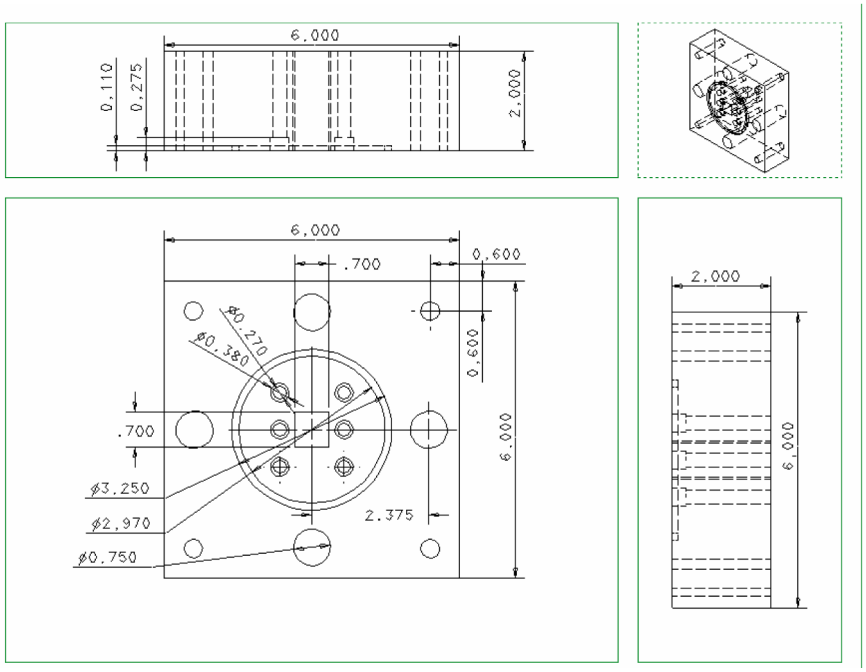

Figure 3.16: Front Block Schematic for Supersonic Combustion Rig

The combustion characterization test section consists of three components, a solid combustion block, a nozzle plate, and a quartz window held in place by a window holder. All of these parts are milled from 306 stainless steel so they are able to withstand the heat loads during testing. The combustion block is connected to the front block using four bolts and has a corresponding 0.5 inch square flow path aligned with that of the transition block upstream. The combustion block itself makes up three walls of this flow path with nozzle plate making up the fourth, or front wall. In this section the walls are referred to by their orientation on the test stand with the observer looking at the flowpath. The square flow path extends for 7 inches after which a three dimensional expansion with an angle of 3.6° occurs. The expansion

runs the rest of the length of the combustor which is 12 inches. Again the combustor block makes up three of the walls of the test section in the expanding flowpath and the quartz window makes up the fourth.

Injection ports are located 0.75 inches and 1.75 inches downstream of the expansion point on both the back and top wall of the test section. These ports are perpendicular to the expanding walls and measure 0.1 inch in diameter at the test section. The ports extend 0.25 inch into the block after which they expand to accept a standard 1/8 inch normal pipe thread (NPT) fitting. Also located along the length of the combustor block are pressure ports. These ports are 0.04 inch at the test section wall and expand to 0.063 inch at a depth of 0.1 inch to accept the pressure measurement tubules. Four ports are located in the straight section, on both the top and back walls, beginning 2.0 inches upstream of the expansion with a spacing of 0.5 inches between each port. Twenty-two ports are located in the expanding section, on both the top and back walls, beginning 0.25 inches downstream of the expansion with a spacing of 0.5 inches between each port. Naturally some ports are omitted due to the injection ports and connecting bolt clearance constraints. It should be noted that the injection ports occur along the pressure port spacing, that is to say the pressure ports directly upstream and downstream of the injection ports are at a distance of 0.5 inches. A schematic of the combustion block and associated ports is presented in Figure 3.17.

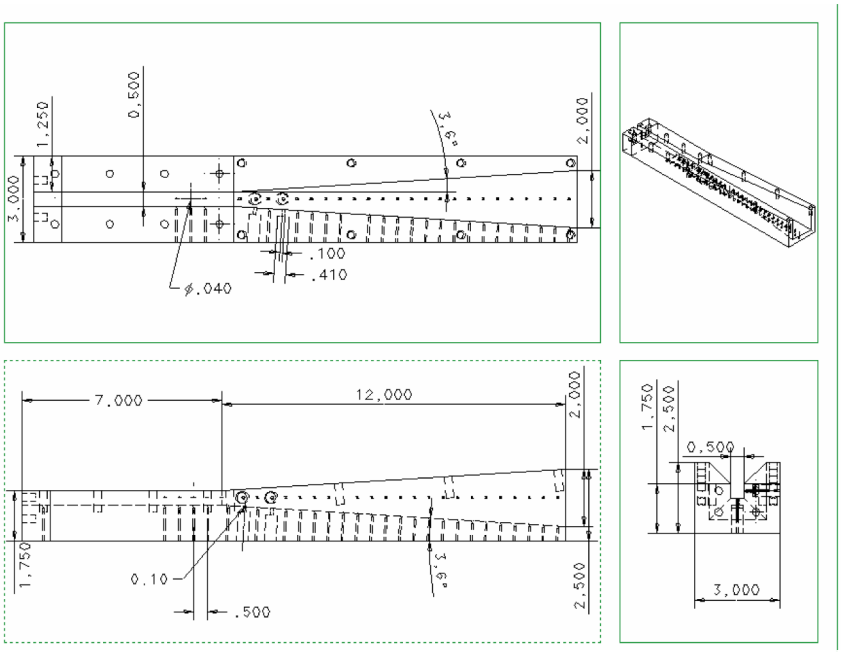

Figure 3.17: Combustion Block Schematic for Supersonic Combustion Rig

The fourth test section wall in the constant area section is established by the nozzle plate. This plate fits flush to the combustion block and has a 0.5 inch wide converging-diverging nozzle profile protruding into the flowpath. The nozzle profile is developed by using the same methodology described for the cavity mixing nozzle profile. A sonic throat is established at the end of the converging section and occurs 4.0 inches upstream of the expansion in the combustor block. The interface between the nozzle plate and combustor block is secured by eight bolts and sealed with a liquid copper gasket. The interface between the nozzle plate and the front block is also sealed with the same gasket and secured by two bolts. A schematic of the nozzle plate is presented in Figure 3.18 .

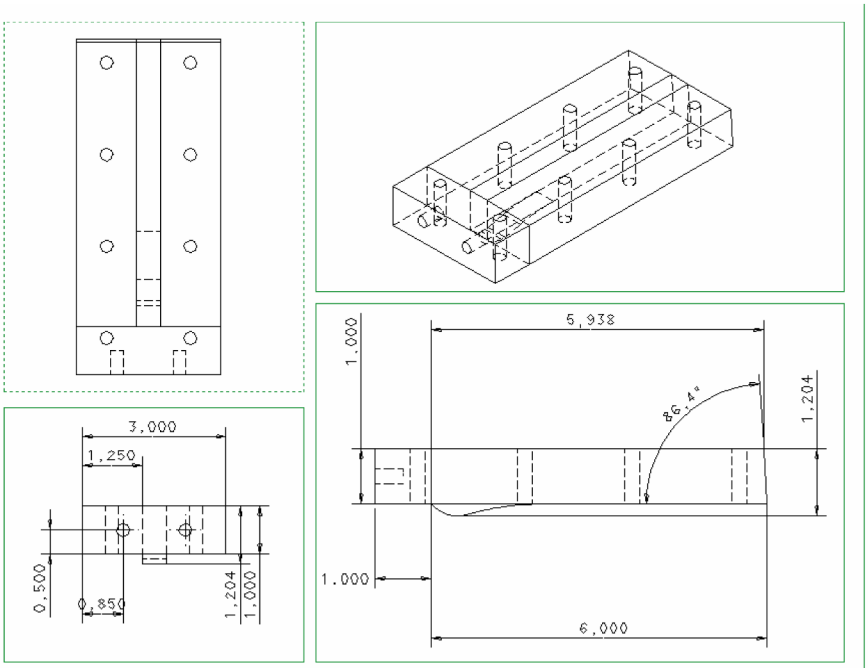

Figure 3.18: Nozzle Plate Schematic for Supersonic Combustion Rig

The final wall of the test section is established by the quartz window held in place by the stainless steel window holder. The window holder allows optical access from the expansion to 11.65 inches downstream with a width of 1.4 inches. The quartz-metal interfaces are sealed with 1/32 inch high temperature silicon gaskets. A schematic of the window holder is presented in Figure 3.19.

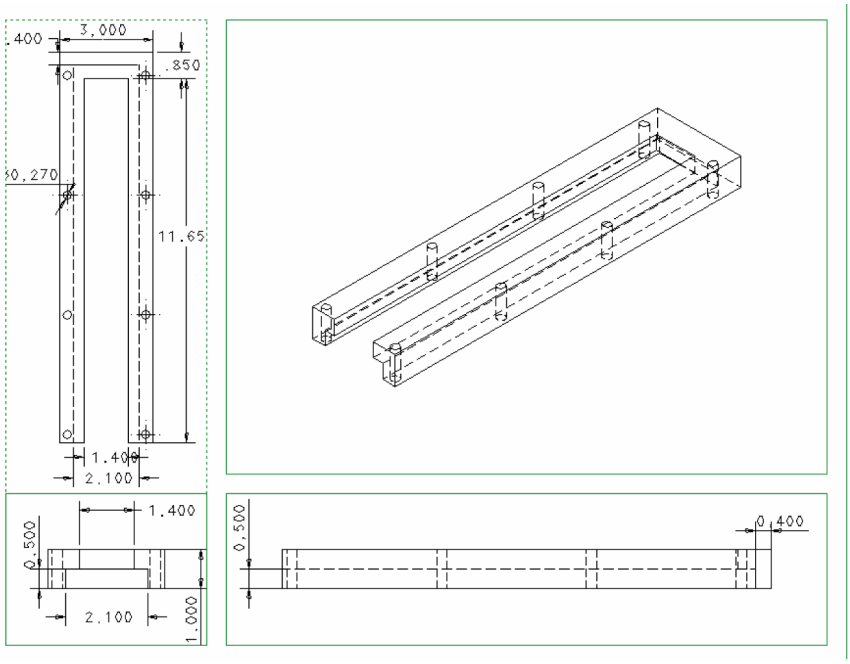

Figure 3.19: Window Holder Schematic for Supersonic Combustion Rig

The exhaust from the combustion block flows into the laboratory exhaust system via an eight-inch water cooled duct. This is placed downstream of the combustion block exit and has no notable effects on the flow field in the combustor.

In order to provide an ignition source for the fuel injected into the combustor block a pilot flame is established at the second injection port in the staged fuel injection studies. This is accomplished by the use of a staged igniter system. The igniter burns a fuel-air mixture which is initially reacted by a spark plug. The air supply is brought in perpendicular to the fuel supply and the flow is also perpendicular to the spark. The flame is sustained by a small rearward facing step in the igniter itself. Following the ignition of this hydrogen-air mixture a secondary fuel

is brought through an additional injector perpendicular to the core flow. Overall the length of the igniter is 6 inches with the first fuel injection 0.75 inches from the air entrance, the second fuel injection 2.75 inches downstream and the spark plug 1.75 inches downstream. The total flow (fuel 1, fuel 2, and air) is then passed through a choked orifice before expanding into the fuel injection port on the combustor block. This acts as a secondary flame holder and is utilized in the pilot flame operation described in subsequent sections. A schematic of the fuel delivery system is shown in Figure 3.20. Additionally, a CAD model of the igniter itself is presented in Figure 3.21 .

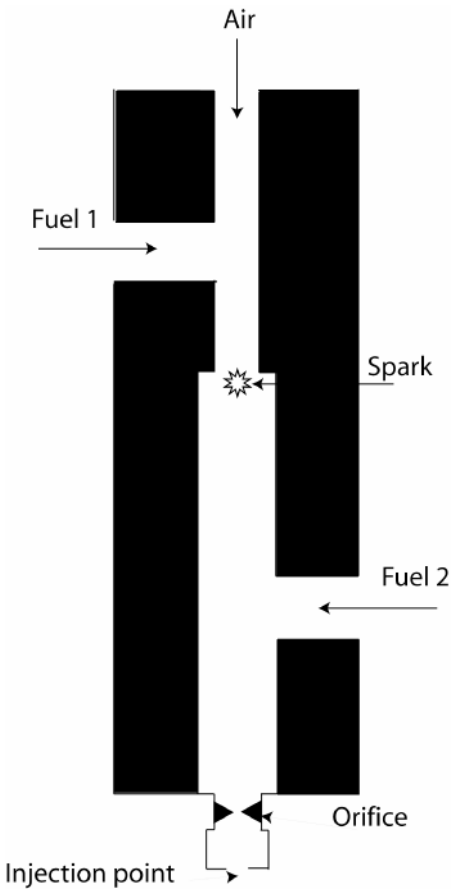

Figure 3.20: Basic Diagram of Igniter

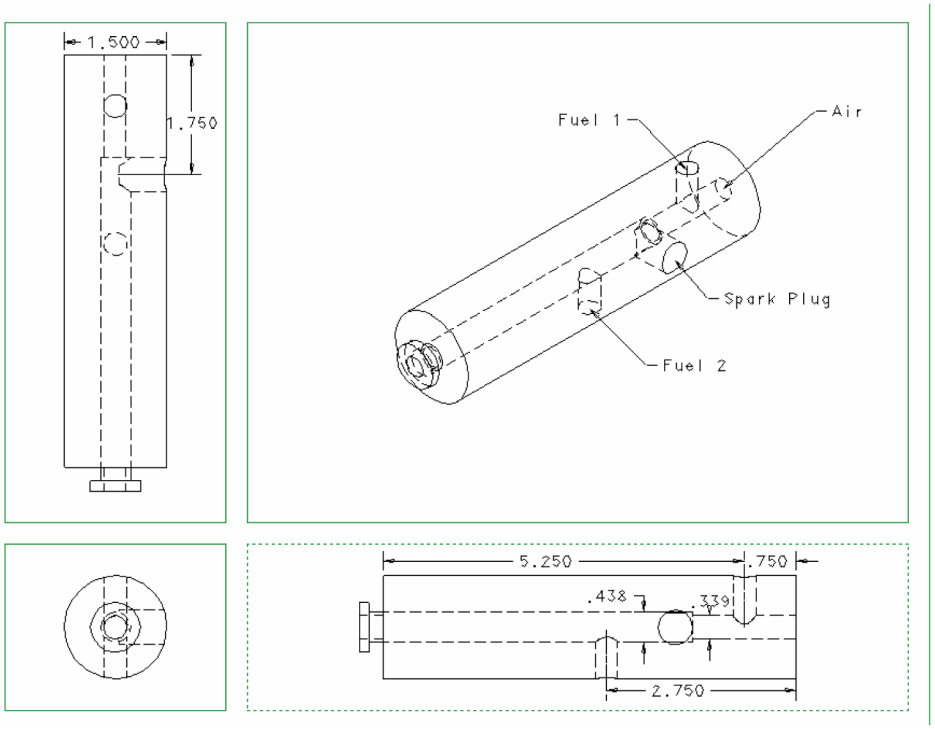

Figure 3.21: Igniter Schematic for Supersonic Combustion Rig

Fuel and air supplied to the igniter as well as the combustion block is fed from pressurized supply bottles via 0.25 inch supply lines. Four lines were available for use on the combustion rig and all four were utilized with different fuels / air. These lines are passed through direct acting electronically controlled valves. The valves are normally closed stainless steel valves controlled by 10 watt, 24 volt DC solenoid coils. Signals were sent to the solenoid valves via a custom built switch box apparatus. A schematic of the apparatus is presented in Appendix A: Switch Box Control System. Choked orifices were placed in each line to regulate the mass flow of each gas. The types of gases used and their respective orifice sizes can be found in

Table 3-3.

Table 3-3: Gas Grades and Orifice Sizing

Gas	Supply line	Airgas® Grade	Orifice Size (in)
Hydrogen	3	Zero Grade	0.012
Ethylene	2,4	Chemically Pure Grade 2.5	0.010, 0.100
Air	1	Dry Grade/ Compressor Supply	0.033

Spark to ignite the fuel-air mixture was provided by an automotive type Autolite copper core spark plug driven by a Standard Motor Products coil. The coil was powered by a Interstate 60 month Meta-tron battery and spark timing was controlled by a solid-state relay. The relay control signal was provided by a Wavetech 40MHz Universal Waveform Generator and consisted of a pulse signal with 2 ms duration and 20 ms period.

A schematic of the assembled test apparatus is presented in Figure 3.22 with the igniter system in place. Additionally a picture of the apparatus is presented in Figure 3.23 .

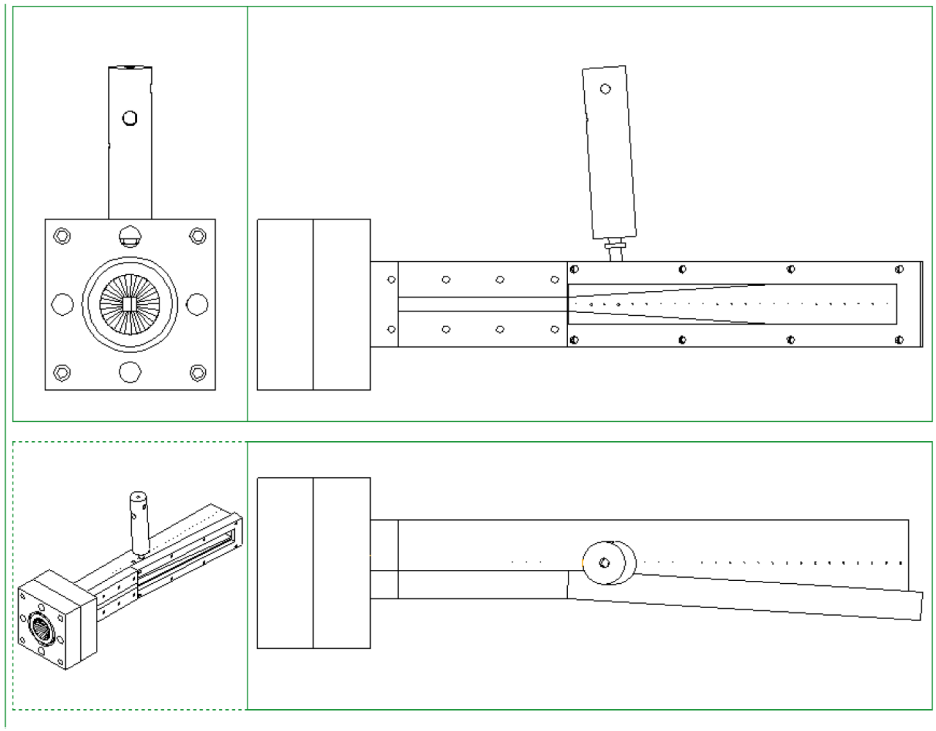

Figure 3.22: Supersonic Combustion Rig Schematic with Igniter

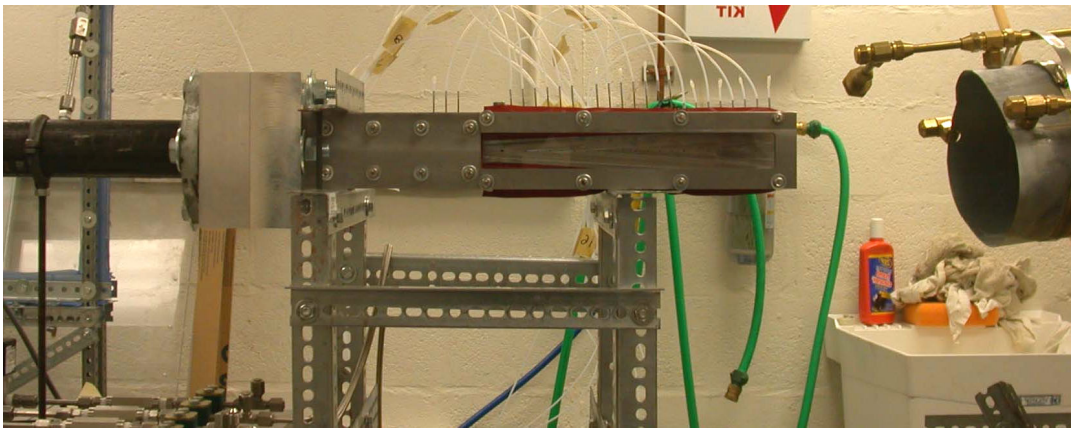

Figure 3.23: Picture of Supersonic Combustion Rig on Reacting Flow Stand

3.3.2 Diagnostics

3.3.2.1 Scanivalve Pressure Measurements

A Scanivalve Corporation DSA-3217 Digital Sensor Array was used to make static pressure measurements at all of the pressure ports along the top and back walls of the combustion block. This Array consists of 16 temperature compensated piezoresistive pressure sensors with a pneumatic calibration valve. The 16 sensors, or channels, all have a range of 0-200 psi. Their associated error is ±0.2% of scale for pressures less than 1 psi, ±0.12% of scale for pressures between 1 and 5 psi, and ±0.05% of scale. The measured pressures are sent via a TCP/IP connection to a desktop computer and into a LabView virtual control panel. This virtual interface (VI) allowed for monitoring of all 16 channels and the DSA's settings as well as writing of the data to a text file to be read by post-processing software. The default settings for the DSA were manually changed to give better temporal resolution and to provide data for determination of error. Settings which were changed were the period, or time between scans, which was set to the minimum setting of 250 μs and the average which was set to 5 scans. The DSA has only 16 channels and there are a total of over 50 pressure ports on the combustor block. For that reason multiple runs were performed with the pressure lines connected to different port configurations. Those ports not being monitored were capped.

3.3.2.2 Optical Measurements

Optical measurements were taken using a ½ inch Pulnix Interline Transfer B/W Charge-Coupled Device (CCD) Camera with SC-745 shutter control to monitor the supersonic combustion rig during the experiments. The shutter speed is adjustable from 1/60 to 1/10,000 seconds but was generally time averaged (long shutter) for monitoring purposes. This camera was mated to a 13 inch Sony high-resolution Trinitron Monitor and recorded to VHS. Images of interest were then digitized using a Data Translation frame grabber using the Global lab software.

3.3.2.3 OH* Chemiluminescence

To further characterize the flame front and combustion characterization OH* chemiluminescence was employed. This was done by utilizing a PCO Dicam Pro Intensified CCD camera. The ICCD has a shutter speed as short as 3 ns and is operated at a frame rate of about 5 Hz. When fitted with an narrow band interference filter, centered at 308 nm, the ICCD will only pick up images of the OH* radical. Also fitted to the ICCD is a UV lens which allowed for focusing as well as zooming on areas of interest. The ICCD system is computer controlled and can be adjusted for gain, image size, averaging, and imaging time. A tripod was used to position the camera at the same height as the test section and a variety of images were taken from time averaged to instantaneous. These images were exported from the Dicam software and saved to a hard disk for analysis.

3.3.3 Experimental Procedure

The flow was established by using the Wilkerson regulator and the Setra static pressure transducer to set the upstream stagnation pressure. Initial testing investigated pressures from 30 to 130 psig, however subsequent testing centered on the higher pressure range from 90 to 130psig.

3.3.3.1 Staged Fuel Injection Studies

Once the flow was established, the igniter system was brought on-line systematically. First air flow for the igniter was set, after which the spark plug was turned on, then fuel 1 was brought on to produce the igniter flame. The spark plug was turned off and the secondary fuel, fuel 2, was turned on once the igniter flame was burning. After a short time (~5s) the primary igniter fuel, fuel 1, was turned off and the flame was re-established at the downstream flame holder between the choked orifice and the fuel injection point. This region is presented at the bottom of Figure 3.20. This flame protruded into the main air flow and established the pilot flame used to anchor supersonic combustion. Occasional flame outs of this pilot flame occurred after which the same steps were repeated to re-establish the pilot flame.

The main fuel was brought on and injected upstream of the pilot with the pilot flame burning. Pressure measurements were taken for 5 second durations under conditions of pilot only, fuel and pilot, and non-burning cases with the pilot and main fuel being injected. Main fuel pressures were varied to produce a range of

equivalence ratios in the core flow. Table 3-4 shows the range of equivalence ratios and fuel types investigated. OH* chemiluminescence monitoring was performed for the hydrogen main fuel cases, and some chemiluminescent data was collected.

Table 3-4: Staged Fuel Injection Test Matrix

$P_{0, Air}$	Fuel 1	Fuel 2	Main Fuel	Equivalence Ratio(s)
90	H_2	C_2H_4	C_2H_4	0.3, 0.4, 0.5
110	H_2	C_2H_4	C_2H_4	0.3, 0.4, 0.5
130	H_2	C_2H_4	C_2H_4	0.3, 0.4, 0.5
130	H_2	C_2H_4	H_2	0.05, 0.075, 0.1

4 Cavity Induced Mixing Quantification

Cavity induced mixing enhancement is examined to further explore the formation and transport of coherent structures downstream of the fuel injection. Quantitative measurements and new techniques were employed to investigate these phenomena. Schlieren images were recorded for the optical conditions described in Table 3-1 for the testing conditions described in Table 3-2. The short shutter speeds and high framing rates are examined in section 4.1. These investigations show instantaneous images of the convecting structures. The longer shutter speeds and associated intensity maps are investigated in section 4.2. These images show time averaged information and are utilized to map the average fuel injection pattern. Finally the LIBS investigation is discussed in section 4.3. LIBS provide instantaneous as well as averaged elemental concentration and fuel-air ratio measurements.

4.1 High Speed Schlieren Results

High speed Schlieren images were recorded for both the baseline and cavity configurations for the cavity induced mixing enhancement investigation. For the first set of optical conditions the framing rate was set at 2000fps and the shutter speed was 1/64000s. The investigation area comprised the full height of the test section duct and extends over a length of 1.5 inches upstream of the injector (0.5 inches upstream of the cavity leading edge) and 3.5 inches downstream of the injector. The second set

of optical conditions consisted of an 8000 fps framing rate and shutter speed of 1/128000s. In this case the investigation area comprised the full height of the test section and extended 2 inches upstream of the injector and 3 and 5/8 inches downstream. A standard, non-zoom, lens was used for this second optical configuration.

4.1.1 Optical Configuration #1

Images collected at 2000 fps and 1/64000s shutter speed had some amount of time averaging however some important characteristics can be observed in the imagery. Baseline imagery shows stationary shocks and very little dynamic response within the flow. These images can be seen in Figure 4.1. It should be noted that the first image has the calibration grid in place for reference to the image's physical size. The experimental images had a height of 256 pixels, however half of the original image height was not of interest therefore the images displayed in this subsection have been cropped to a height of 128 pixels with no reduction in resolution.

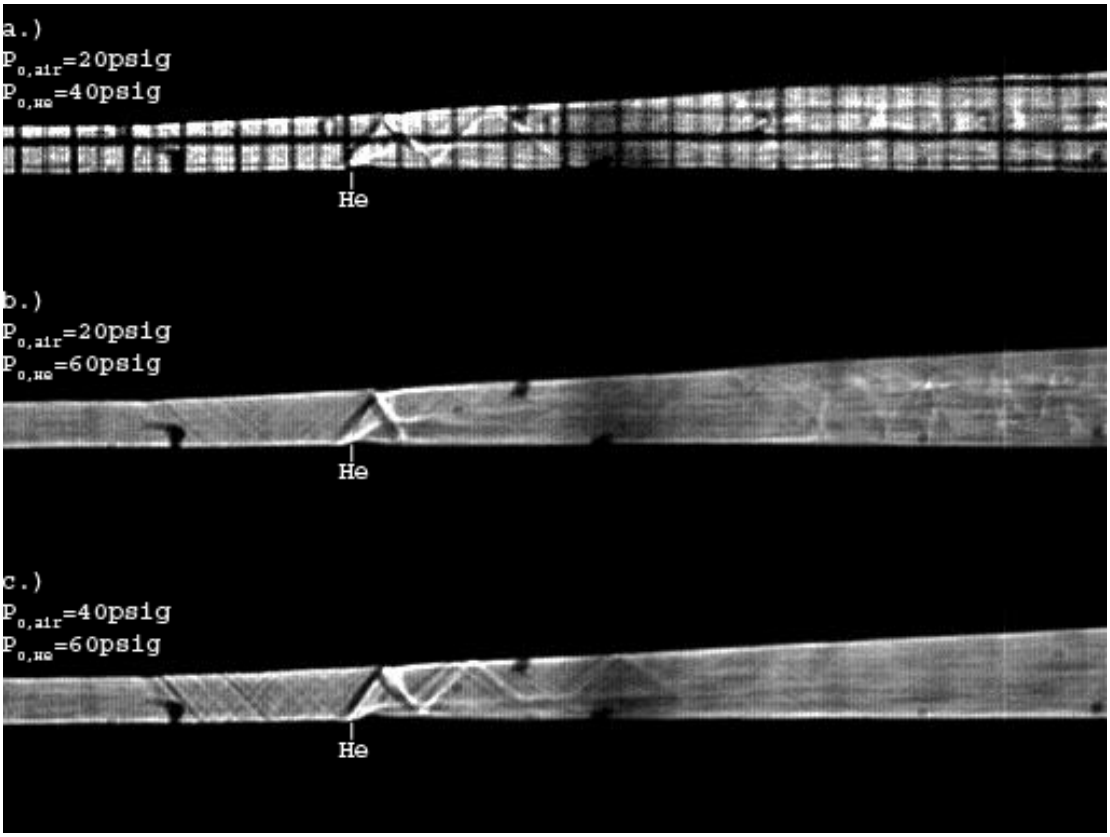

Figure 4.1: Schlieren Images of Baseline Configuration, Optical Configuration #1 for: a.) 20psig Air, 40psig He b.) 20psig Air, 60psig He c.) 40psig Air, 60psig He

From these images, for the three flow conditions investigated, it can be seen that as the upstream air stagnation pressure is increased the shock angle caused by the fuel injection actually becomes more normal. It is originally expected that increasing stagnation pressure will result in higher local Mach number and thus more shallow shock angle, however the opposite is observed. Similar effects have been observed in previous experiments of a similar nature[10]. This change in angle can be explained by the boundary layer growth and more specifically its transition from laminar to turbulent.

When the injection is investigated it can be seen that the normal injection is bent over and the density gradient between fuel and air forms almost a straight line extending back from the injection point. This is most easily seen in part c.) of Figure 4.1. In contrast to this compact, and not very well mixed, fuel injection the cavity cases can be observed for the same optical conditions in Figure 4.2.

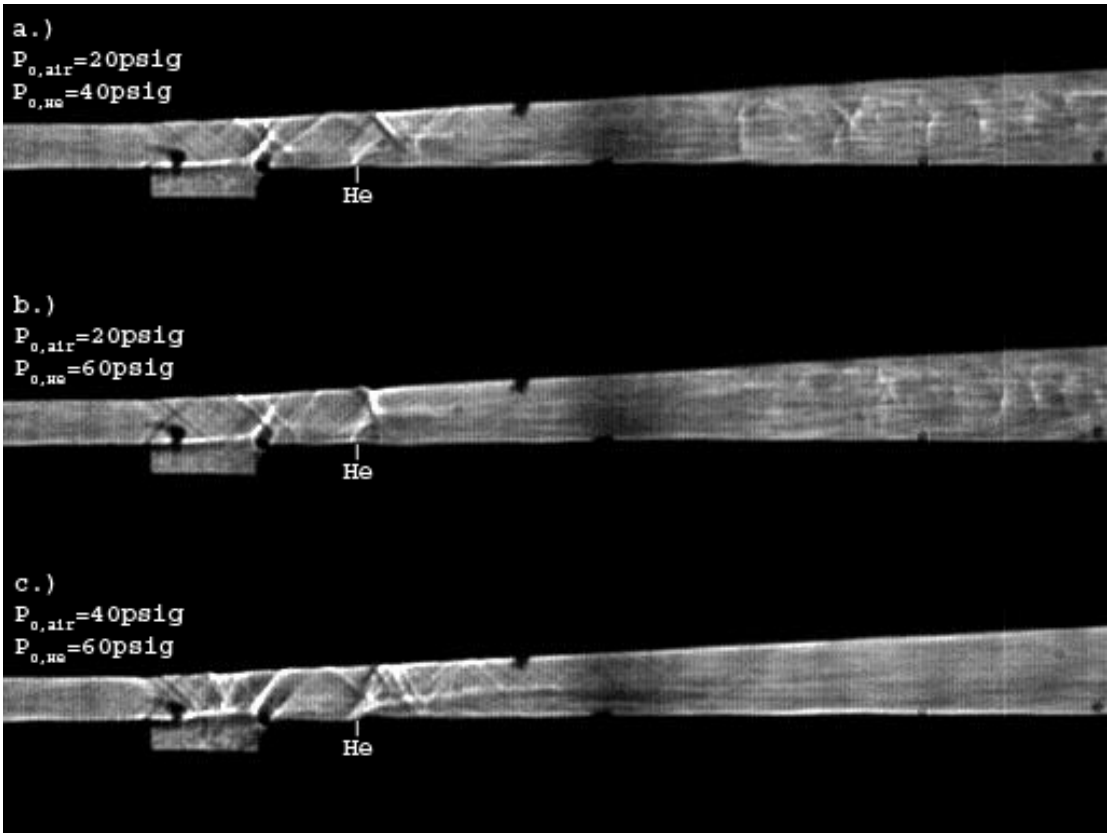

Figure 4.2: Schlieren Images of Cavity Configuration, Optical Configuration #1 for: a.) 20psig Air, 40psig He b.) 20psig Air, 60psig He c.) 40psig Air, 60psig He

No direct 'frozen' imagery of the coherent structures can be seen in the flow downstream of the cavity however the injection profile can qualitatively be seen to penetrate farther into the freestream as evidenced by the density gradient shown by

the dark line extending from the injector. The nature of the cavity is seen in Figure 4.2 as the shear layer can be seen spanning the cavity length. Also, the shocks at the injection point are more normal than those for the non-cavity case. This is representative of the pressure loss associated with the cavity addition. Pressure loss is expected due to the sudden expansion along with the shock and expansion structures formed by the cavity dynamics. This pressure loss is a key issue for future comparison of mixing techniques as total pressure losses reduce the efficiency of a given propulsion system. Therefore, minimizing total pressure loss while maximizing the combustion benefits is the ultimate goal of a mixing enhancement device. A study of this nature is important to determine optimal mixing configurations but is beyond the scope of the current investigation.

Although individual structures cannot be identified at this shutter speed the qualitative nature of the cavity enhancement can be observed. The case for air at 40psig and helium at 60psig is shown in Figure 4.3. Since the shutter speed is set to 1/64000s the images here represent approximately a 16μs average and each image is spaced 0.5ms apart. Time histories for the other two cases can be found in Appendix B-1: Optical Configuration #1.

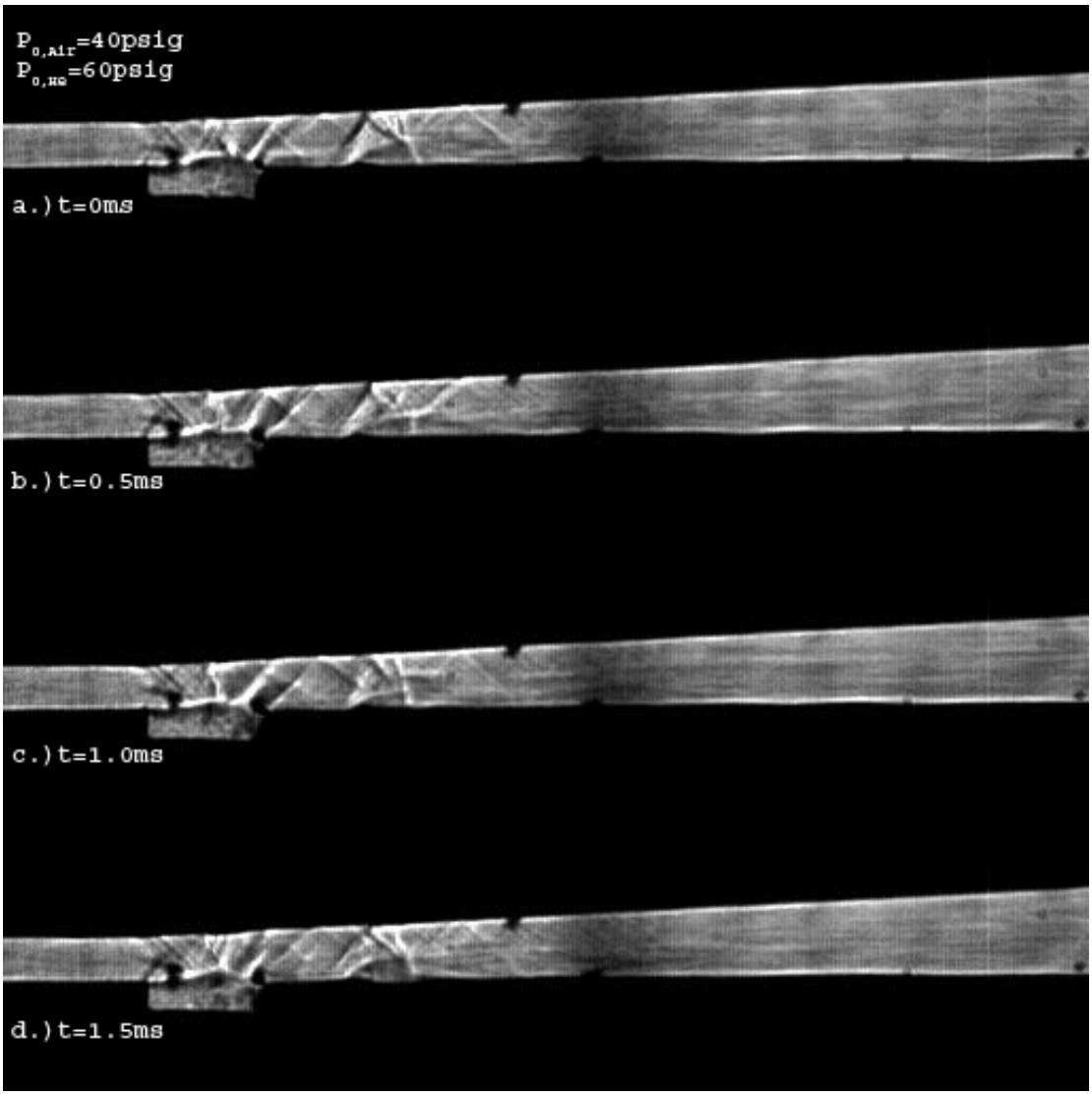

Figure 4.3: Schlieren Images of Cavity Configuration, Optical Configuration #1 for: Air=40psig, He=60psig at a.) 0ms b.) 0.5ms c.) 1.0ms d.) 1.5ms

Here it can be seen that the shear layer periodically oscillates up and down and the fuel injection penetration depth changes accordingly. These results agree with previous historical results[10,36,37,42] and verify the open nature of the cavity, since images show that the shear layer clearly does not reattach to the bottom floor of the

cavity. These images also demonstrate the qualitative operation of the cavity mixing mechanism by visualizing the oscillation of this shear layer.

4.1.2 Optical Configuration #2

Images collected at 8000 fps and 1/128000s shutter speed had very little time averaging and display 'frozen' coherent structures convecting downstream of the cavity. It should be noted that although the shutter speed is high enough to capture structures at the shedding frequency, local velocities may be higher than the shedding frequency and therefore some of the structures themselves may be time-averaged. For this configuration a standard lens with no optical zoom was employed and the images therefore represent a slightly larger area with lower resolution.

Again, baseline imagery shows stationary shocks and very little dynamic response within the flow. Images for optical configuration #2 are presented in Figure 4.4. It should be noted that these images were resized to match the physical size of those images taken for optical configuration #1, however their resolution was not changed.

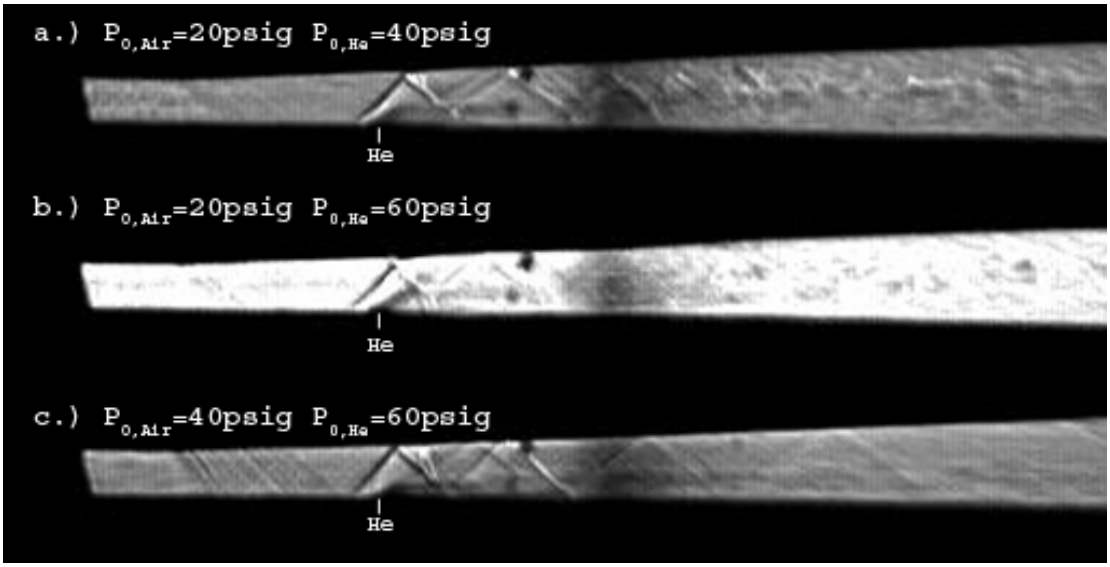

Figure 4.4:Schlieren Images of Baseline Configuration, Optical Configuration #2 for: a.) 20psig Air, 40psig He b.) 20psig Air, 60psig He c.) 40psig Air, 60psig He

Similar to the images presented in the previous section, again an increase in shock angle is seen as upstream stagnation pressure is increased. Taken at a higher shutter speed, these images represent a time average over a duration of approx 8 μs, which capture 'frozen' images with respect to the shedding frequency of the cavity oscillations. this can be seen in Figure 4.4 which shows the turbulent structures observed in the fuel injection wake. Here again it is clear that the fuel injection does not penetrate very far into the core flow.

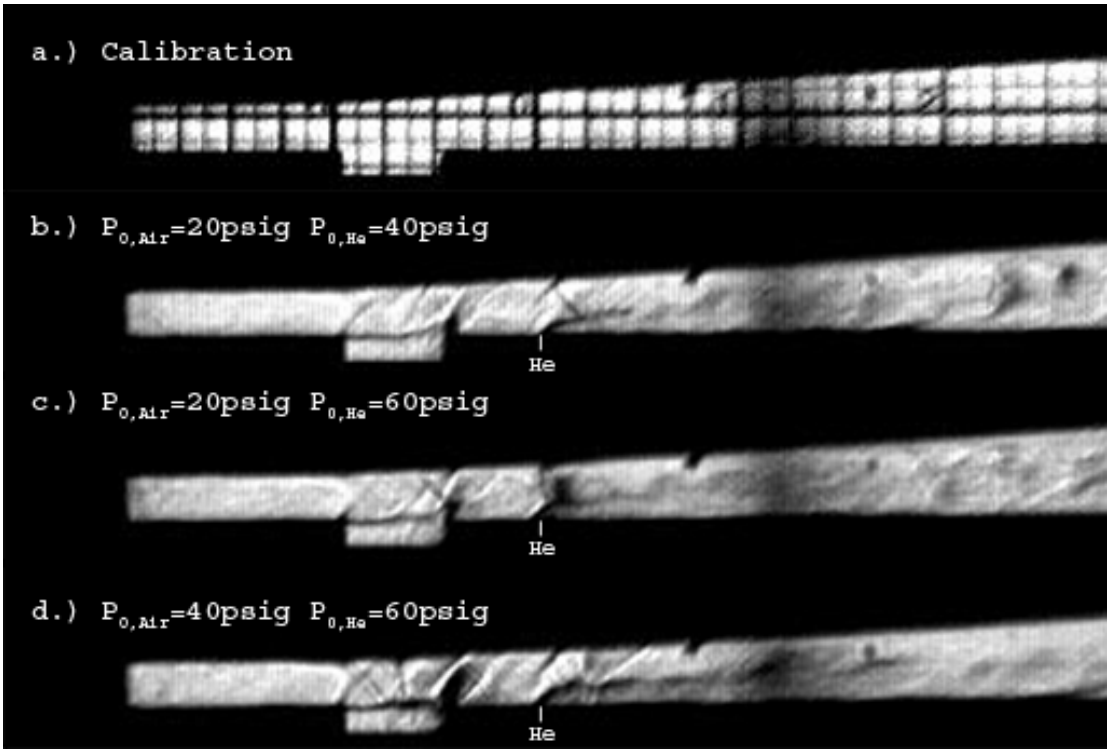

Figure 4.5: Schlieren Images of Cavity Configuration, Optical Configuration #2 for: a.) Calibration b.) 20psig Air, 40psig He c.) 20psig Air, 60psig He d.) 40psig Air, 60psig He

When the cavity configuration is investigated using this high shutter speed individual structures are seen as they convect downstream from the fuel injection point. This is particularly evident in the highest pressure cases seen in Figure 4.5 d.). It is important to note that multiple structures can be seen both at the injection point and farther downstream. These images conclusively show that the structures are periodic and do convect downstream from the cavity. Again the shocks in front of the fuel injection appear to be more normal in the cavity cases, evidence of the cavity pressure losses. Here it can also be seen qualitatively that the fuel penetrates significantly farther into the core flow periodically. Figure 4.5 a.) is included to

provide the calibration for the physical size of the images taken for optical configuration #2.

The images taken for optical configuration #2 represent events spaced 0.125 ms apart due to a framing rate of 8000fps. At this framing rate, with an assumed freestream Mach number of two, the structures formed at the injection in one frame will have convected out of the inspection area by the next frame. This prevents observation of individual structures' motions downstream. However, when the time histories are observed, the oscillating motion of the shear layer over the cavity can be seen. Individual structures can be identified at multiple points downstream of the injection point which is also evidence of their convection. Furthermore, when subsequent frames are viewed these structures have shifted (out of the frame) while new structures have appeared to take their place. Since no phase-locking was performed the subsequent frames are not being captured at any multiple of the shedding frequency. This indicates that the positions of structures in subsequent frames are not comparable due to aliasing. The time history of the highest pressure case (air = 40psig, He = 60psig) can be seen in Figure 4.6. Time histories of the other conditions can be found in Appendix B-2: Optical Configuration #2.

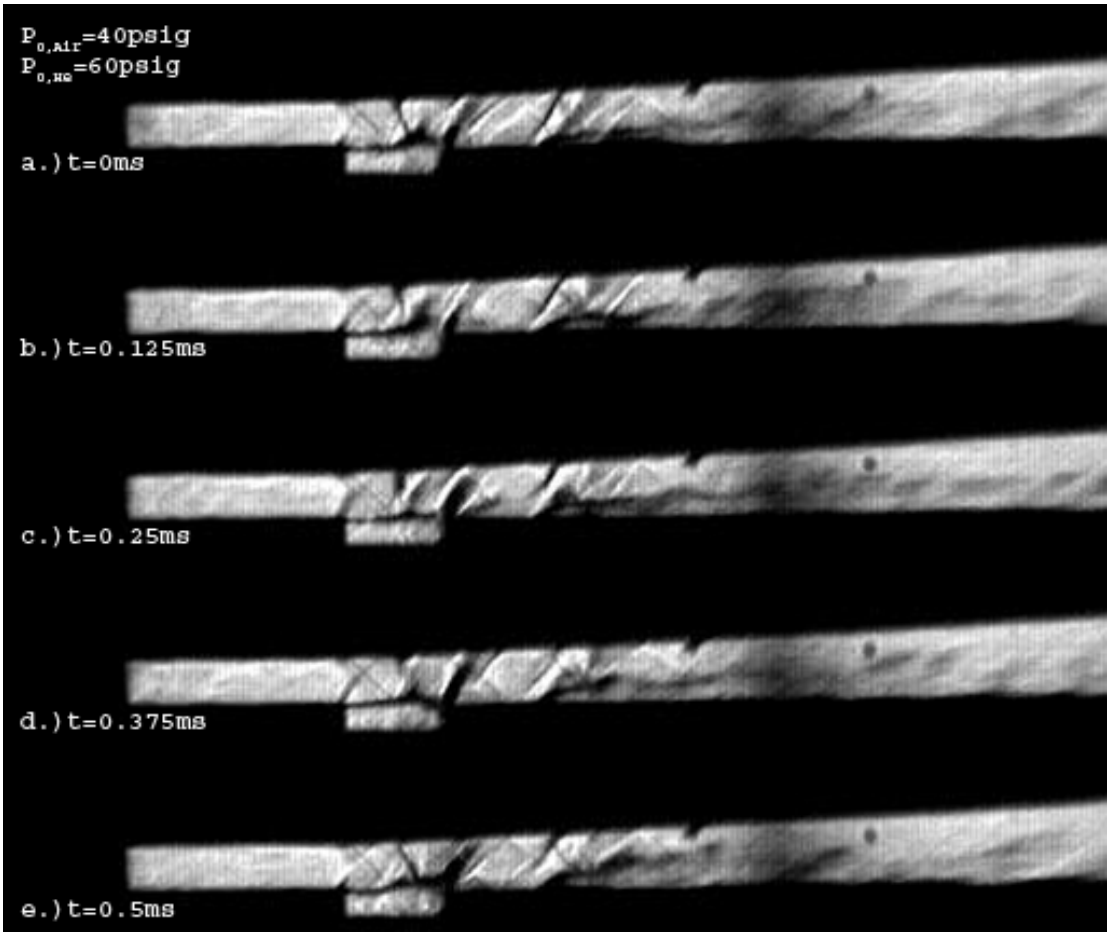

Figure 4.6: Schlieren Images of Cavity Configuration, Optical Configuration #2 for: Air=40psig, He=60psig at a.) 0ms b.) 0.125ms c.) 0.375ms d.) 0.5ms

4.2 Time Averaged Schlieren Results

Time Averaged Schlieren images were acquired for both the cavity configuration and the baseline configuration for all of the testing conditions. These images represent the average flowfield over time, and are useful for quantifying the average fuel injection trajectory and average mixing. Image post-processing in Matlab allowed these metrics to be quantified from the imagery.

4.2.1 Optical Configuration #3

The third optical configuration utilized a shutter speed of 1/60s and a framing rate of 60fps. Since these are time averaged, every image produced is nearly identical and no time histories were resolved. The inspection area was significantly smaller for these images and measured only 1 inch of the flowfield downstream of the injector. Multiple images were taken to assemble a full downstream view however they were not analyzed because only the initial fuel injection trajectory is clearly defined and demonstrates the effective difference with cavity enhancement.

The time averaged images for the baseline case reiterate the earlier observation that as the stagnation pressure of the air is increased upstream the shock angle at the injection point becomes more normal. Images of the three cases are presented in Figure 4.7 for the baseline configuration. The change in angle is evident between cases b.) and c.) as the air stagnation pressure is increased to 40psig. Here it can also be seen that as the fuel injection pressure is increased the average penetration depth increases. Overall, however, the penetration depth is not very great and the clarity of the images provides insight into how stationary the structures are with respect to time.

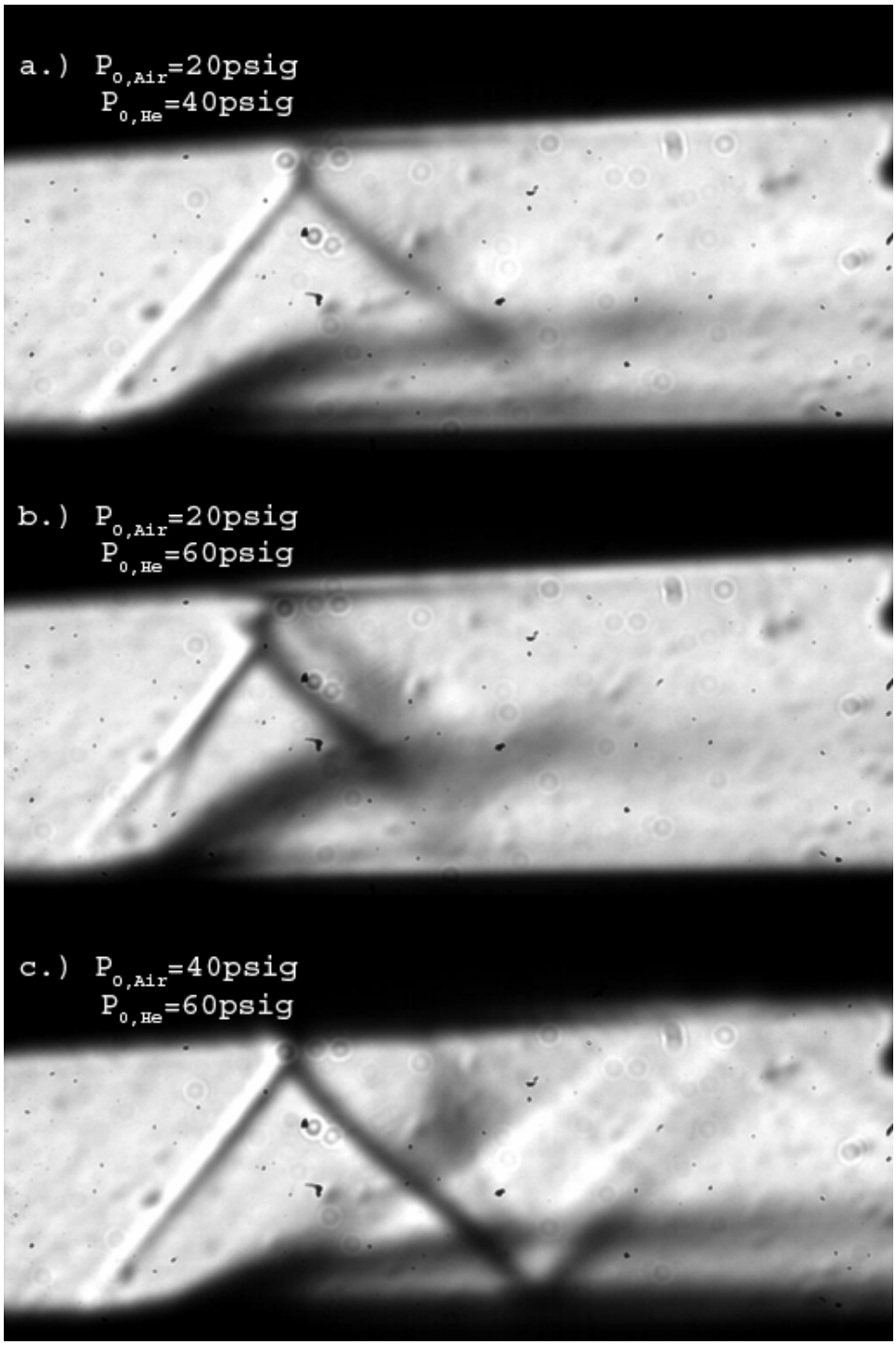

Figure 4.7:Schlieren Images of Baseline Configuration, Optical Configuration #3 for: a.) 20psig Air, 40psig He b.) 20psig Air, 60psig He c.) 40psig Air, 60psig He

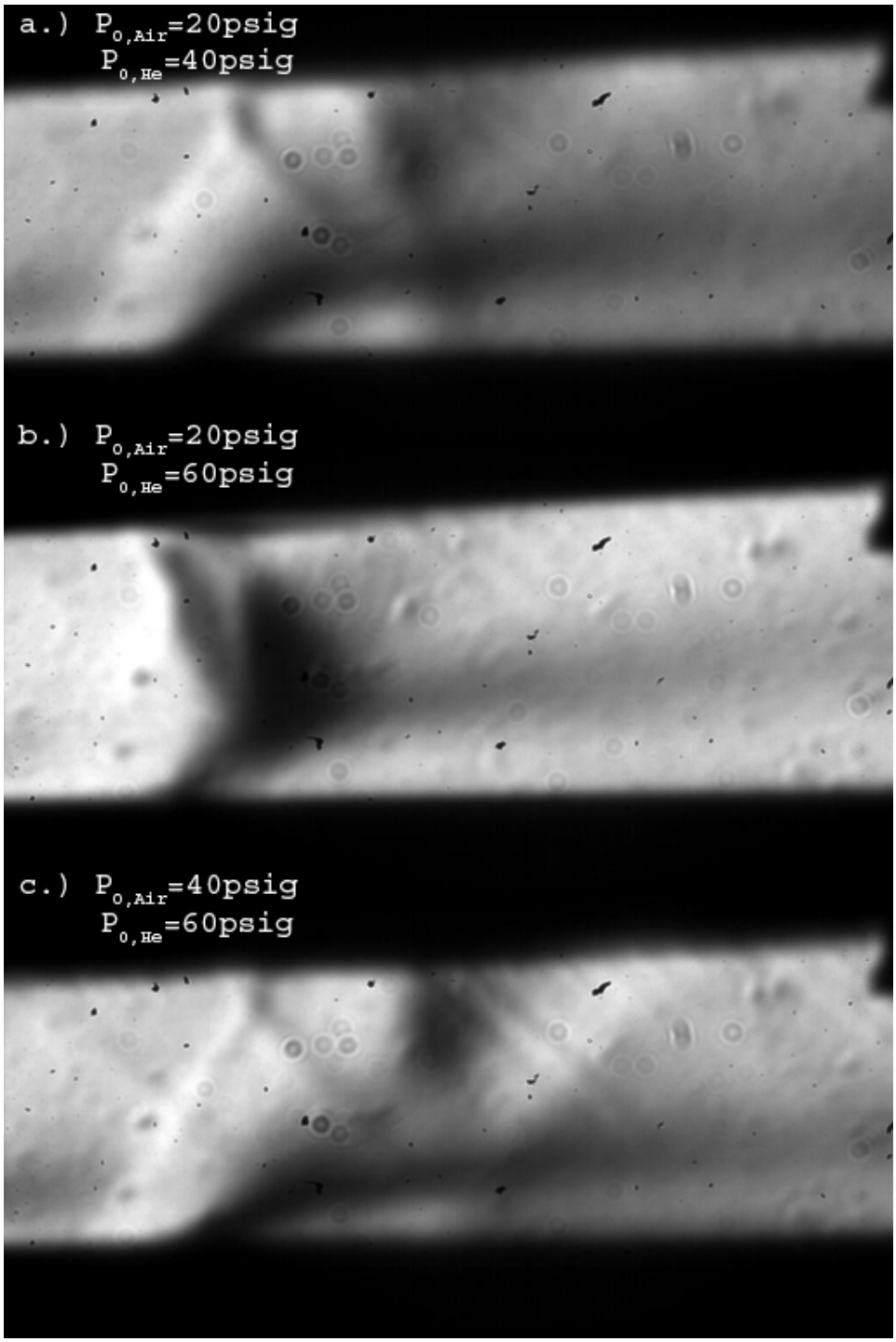

Figure 4.8: Schlieren Images of Cavity Configuration, Optical Configuration #3 for: a.) 20psig Air, 40psig He b.) 20psig Air, 60psig He c.) 40psig Air, 60psig He

The cavity configuration for the same conditions is shown in Figure 4.8. Here it can be seen that the shock structures are more normal than the baseline case as observed in the previous optical configurations. Again in these figures the pressure loss due to the cavity as compared to the baseline case is evident in the more normal shock structures for all the cavity cases. The fuel penetration is deeper for the cavity cases as compared to the baseline cases as seen in Figure 4.9. This image also shows a more disperse density gradient by wider band the fuel injection trajectory follows. This can be explained by either a moving density gradient, since the images are time averaged, or that the density gradient is not as strong which would imply more disperse fuel mixing.

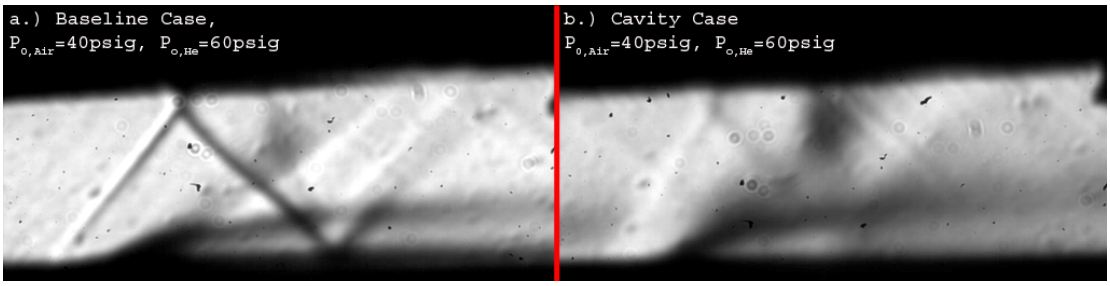

Figure 4.9: Comparison of Schlieren Images, Optical Configuration #3, for Air =40psig, He=60psig, with a) baseline and b) cavity configurations

4.2.2 Intensity Maps

These images were read by the Matlab software and processed as greyscale images. This processing produced a matrix representing each individual pixel of the

image as a value from 0 to 255. This value represents the relative brightness of the image at each pixel, with 0 being 'true' black and 255 being 'true' white. This matrix can be manipulated to investigate the intensity of the Schlieren images and determine qualitative and quantitative characteristics of the flow.

4.2.2.1 Single Pixel Mapping

The simplest manipulation of these matrices is to plot the intensity of the image versus one of the physical axes. This yields the intensity along one pixel width along the height (or width) of the image. The relative intensity in a Schlieren image represents the changing density gradient and can either be darker or lighter depending on the orientation of the Schlieren aperture. In the case of the supersonic mixing enhancements the dark bands represent the density gradient and can be interpreted as the location of fuel-air interface. It should be noted that although the areas below these bands are light it does not mean that there is no fuel, it simply means that there is no density gradient. Thus these regions may be pure fuel or pure air, but gas composition cannot be distinguished in this analysis. An example of the single pixel width intensity mapping is presented in Figure 4.10. The single red line on the Schlieren image, approximately 0.6 inches downstream of the injection, corresponds to the single width intensity map displayed on the right of the image. It should be noted that the x-scale is intensity, from 0 to 255, and the y-scale is height in reference to the overall original image height in this plot. It can be seen that the fuel injection appears as a dark band in the Schlieren and correspondingly a local minima occurs (in

reference to the intensity axis) at that same height.

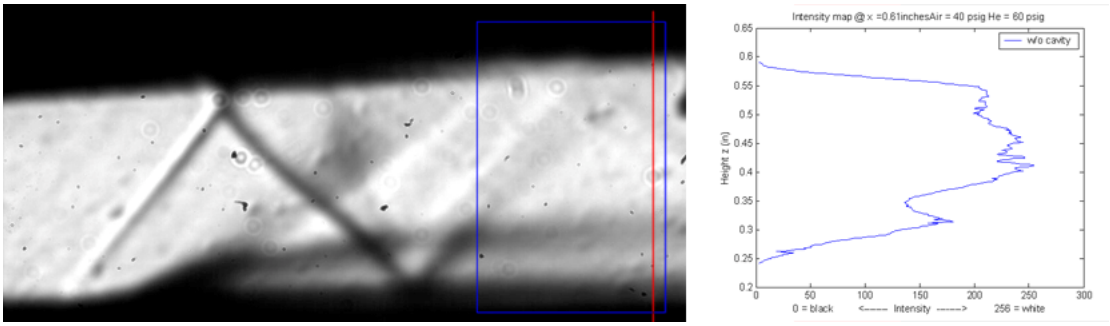

Figure 4.10: Schlieren Image and Corresponding Intensity Map for the Baseline Configuration with Air = 40spig, He = 60psig

More single line mappings are presented for the other conditions studied in Appendix C: Single Line Intensity Maps. This single width mapping provides insight it is fairly rough and only characterizes a small portion of the flow. Average mappings may be of more interest for these reasons.

4.2.2.2 Average Intensity Mapping

An average mapping can be produced by simply averaging the single pixel width intensities over a given image area. In the case of the cavity mixing enhancement averaging is done along the streamwise direction from a distance of 3.75 to 6.25 injection diameters from the injection point. An image of this average is presented in Figure 4.11 where the blue box represents the area being averaged.

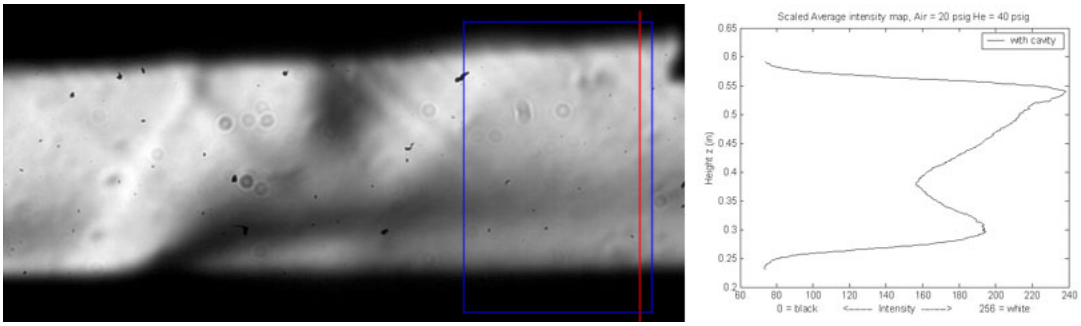

Figure 4.11: Schlieren Image and Corresponding Average Intensity Map for the Cavity Configuration with Air = 40spig, He = 60psig

This mapping represents a much smother curve and can be seen as both a time-averaged and space-averaged map of the intensity which is representative of the density gradient and therefore the fuel-air interface. An evaluation of these mappings compares the baseline and cavity cases and their associated fuel injection characteristics. In Figure 4.12 it these two curves are plotted; it can be seen that the cavity case's low intensity occurs over a broader height, represented by the nature of the curve near the local minima at a height of 0.35 inches. The baseline case, in contrast, has a steeper curve with a darker, or less intense, local minima in comparison to the cavity case. This represents a larger density gradient or a more tightly packed fuel layer. Figure 4.13 zooms in on the region of interest to make these differences more apparent. These curves have been adjusted due to differences in overall intensity between the two sets of images. These differences can be attributed to minute changes in the light source, alignment issues, etc. The curves were scaled to an area upstream of the injection, where the intensity of the two images is assumed to be identical.

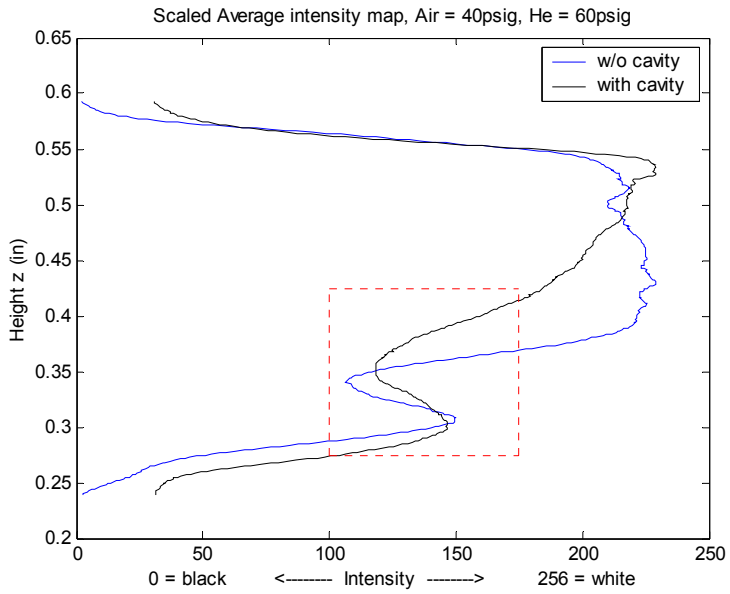

Figure 4.12: Average Intensity Map Comparison for Cavity and Non-Cavity Configurations with Air=40psig, He=60psig

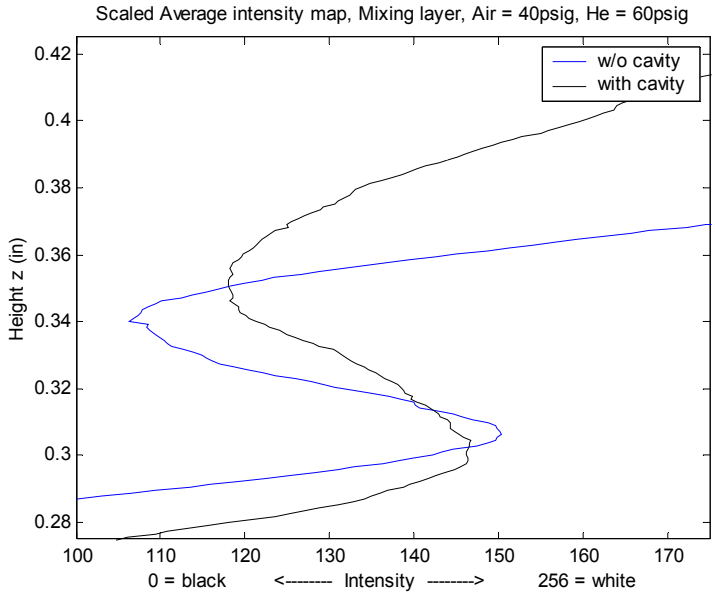

Figure 4.13: Average Intensity Map Comparison of Cavity and Non-Cavity Configurations, Air=40psig He=60psig, Zoomed on Area of Interest

These images show the qualitative time-averaged differences between the fuel injection in the cavity and non-cavity case as investigated by intensity mapping. A more insightful picture of the fuel injection trajectory could be obtained by tracking the local minima across the area of the average images presented in this section.

4.2.2.3 Fuel Injection Mapping

The local minima, which can be used to represent the fuel injection, can be tracked along the length of the inspection area by breaking down the averaged area into multiple smaller averages, or discrete cells. The original averages were discritized into 10 cells and then the local minima were identified using the Matlab software. Their associated heights were calculated and then these values were plotted for both the configurations and all three conditions. This plot is representative of the fuel injection trajectory beginning at a distance of 3.75 diameters downstream of the injector and ending 2.5 injection diameters later. The plot is presented in Figure 4.14. Trend lines fit to the data points are also plotted on this graph. The cavity configuration data points appear as black symbols while the non-cavity configuration's appear as blue symbols. It can be seen that for all cases the fuel injection penetration is greater for the cavity configuration. At the highest pressure case, the slope of the trend line is much steeper for the cavity configuration than for the non-cavity configuration. This indicates that the fuel injection is penetrating faster which is indicative of better mixing. It should be noted that for the trend line configuration the outliers (points 7 and 8 for the two higher pressure non-cavity

cases) were ignored.

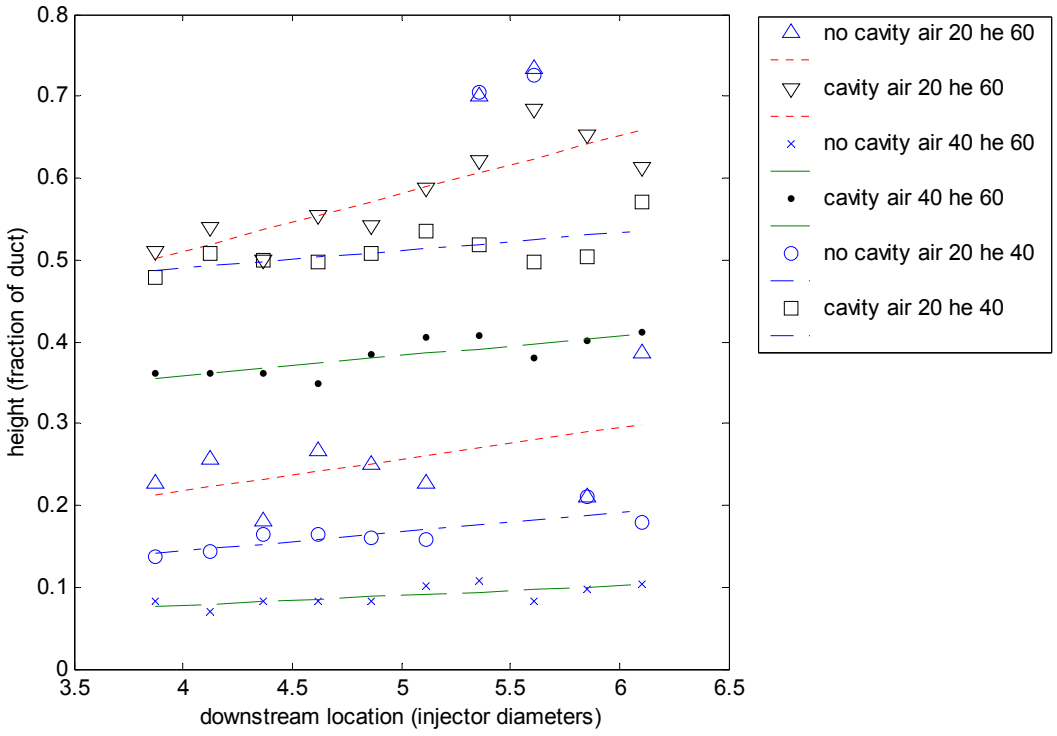

Figure 4.14: Fuel Injection Trajectories for all Configurations and Conditions, Derived from Intensity Mapping

The plots confirm the increased spreading rate and fuel penetration and establish the phenomena qualitatively and quantitatively. The results from the LIBS diagnostics will be compared to these results to evaluate the technique's effectiveness in gaining quantitative fuel-air ratios.

4.3 Dynamic Pressure Measurements

Dynamic pressure measurements were taken to confirm the shedding frequency of the cavity system in reference to Rossiter's model described in Section

2.1.3.2. The pressure port was placed at the trailing edge of the cavity and the output was reduced in Matlab utilizing a Fast Fourier Transform. The output plots from this analysis are presented for all three cases in Figure 4.15.

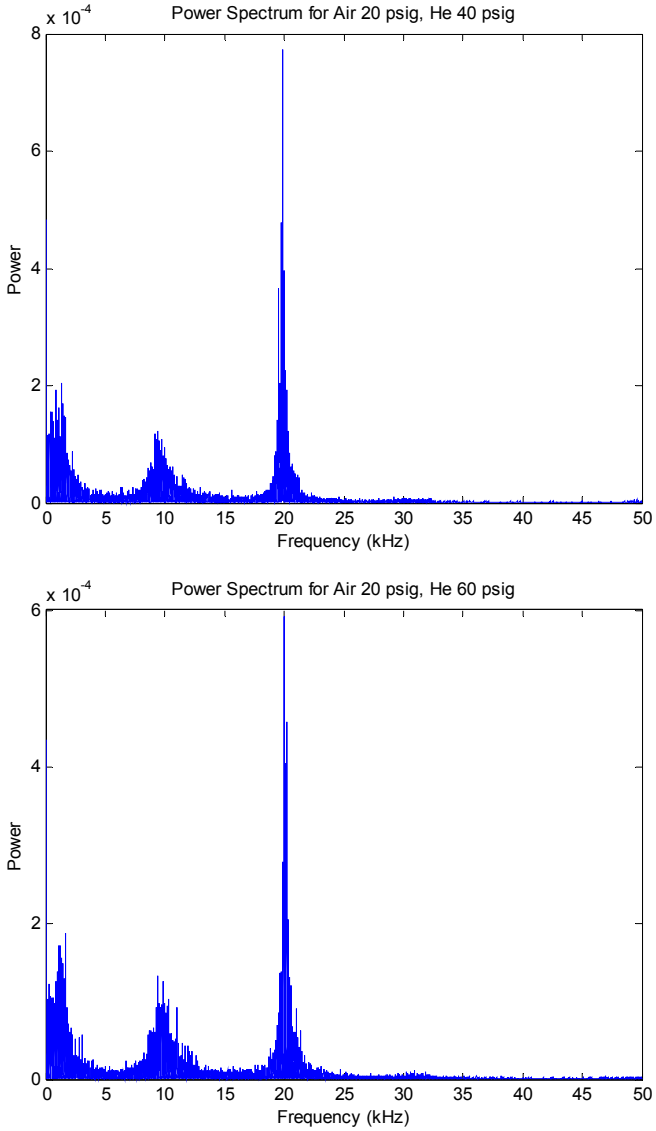

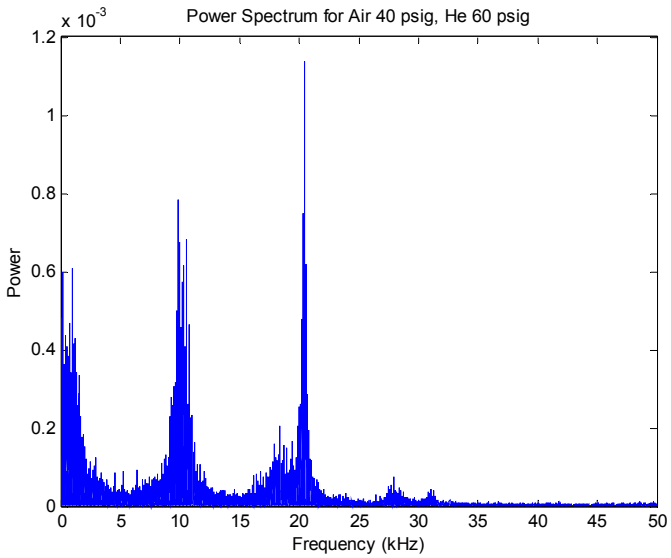

Figure 4.15: Power Spectrum Output from Fast Fourier Transform of Dynamic Pressure Data for all three conditions

In these plots it can be seen that the dominant frequency is centered on 20 KHz which is approximately the predicted value from the Rossiter model for the second harmonic. Analysis of the predicted results and the experimental results are presented in Table 4-1. Here duct Temperature is estimated from previous characterizations of the flow facility[10], and Mach number is estimated by observation of the mach waves present in the Schlieren images. Predicted values are calculated as described in 2.1.3.2. In this table it can be seen that the frequency of the experimental results is within approximately 1 KHz of the predicted value. This confirms that the experimental apparatus tested agrees with previous empirical and analytical results. Further characterization of the shedding frequency across a wider range of upstream pressures was performed and is presented in Appendix D: Dynamic Pressure

Measurements

Table 4-1: Experimental Values and Predicted Rossiter Results for Shedding Frequency and Strouhal Number

$P_{0,Air}$	f_{exp}(kHz)	M_{exp}	T_{exp}	U (m/s)	L_{exp} (m)	$Sr_{L,exp}$	$f_{predicted}$ n=2	Sr_L
20	19.8	1.59	196	446	0.0127	0.564	20.2	0.574
40	20.5	1.48	205	419	0.0127	0.621	19.4	0.588

4.4 LIBS Results

Laser Induced Breakdown Spectroscopy was applied to all the flow conditions and test locations described in section 3.2.2.1. These measurements resulted in 100 single shot data files for each species, He and O, which were loaded into Matlab to be analyzed. The data was manipulated to produce average values at each test point and test condition. Statistical uncertainty was also calculated along with standard deviation. Investigation of these plots reveals the spanwise and streamwise distributions of the He/O ratio for both configurations. These average value plots were also compared to show quantitative differences in the flows between the baseline and cavity configurations.

4.4.1 Streamwise & Spanwise Trends

He/O ratio is determined by analyzing the spectra emitted from the spark

created by the LIBS system. The output of the LIBS measurement directly is 100 single plots of the observed spectra which is post processed and can be evaluated to produce plots of concentration. The methodology and calibration of this particular system is beyond the scope of the current study, however it was thoroughly investigated by Temple[66]. For the purposes of this study the metric of interest is the He/O ratio which is analogous to the fuel to air (or fuel to oxidizer) ratio. It is important to note that the local temperature of the LIBS system completely dissociates Oxygen, thus the ratio is in reference to atomic Oxygen and not molecular. The reader is also referred to Figure 3.13 for a visual representation of the testing locations. In the following plots the value of Y represents the spanwise distance, on one side of the flow, with Y=0 located along centerline. Also, X represents the streamwise distance measured from the injection point. All tests were conducted at a constant height, Z, of 3.2mm.

The streamwise and spanwise trends for fuel to air ratio are quantified by investigating their values for both cases separately at multiple distances in both directions. Figure 4.16 and Figure 4.17 show an example of these plots for the He/O ratio versus y-location for various downstream distances. These show a distinctly higher He/O ratio at the centerline at all downstream locations. This quantifies the three dimensional effects of the single point injection and is an expected result which is illuminated by the LIBS technique.

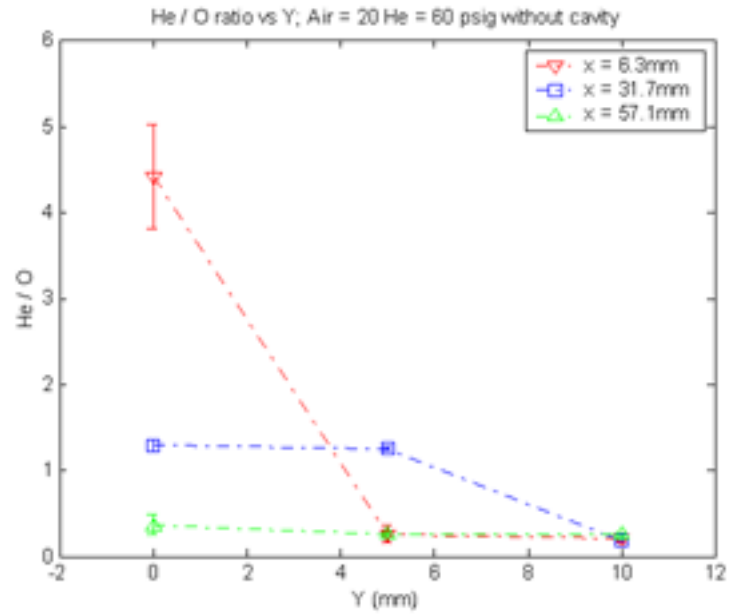

Figure 4.16: Spanwise Distribution of He/O Ratio for Various Streamwise Locations Taken by the LIBS Diagnostics for Air = 20psig, He = 60psig, Cavity Configuration

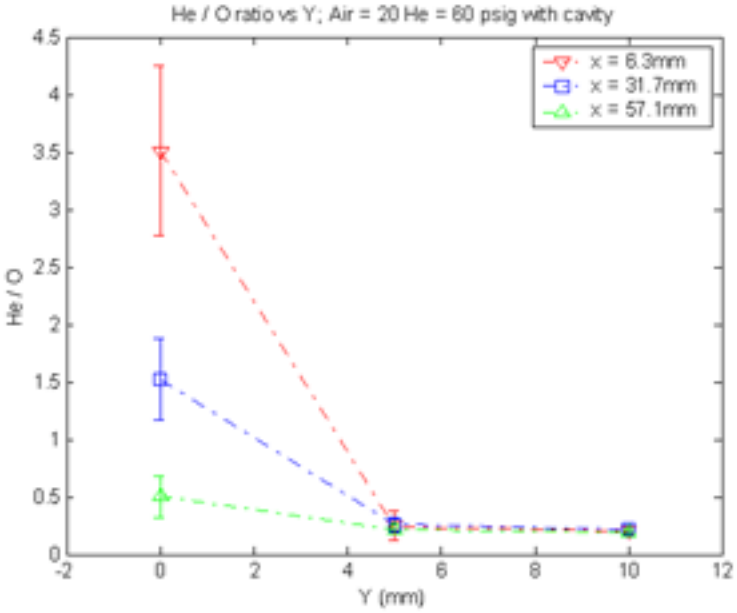

Figure 4.17: Spanwise Distribution of He/O Ratio for Various Streamwise Locations Taken by

This concentration gradient occurs in the spanwise direction therefore it cannot be observed by Schlieren images, because the Schlieren technique integrates across the line of sight. Figure 4.16 shows the values for the non-cavity configuration and Figure 4.17 shows the values for the configuration with the cavity. Both configurations display this spanwise concentration distribution, at all the streamwise locations.

This quantification of He/O ratio proves the applicability of LIBS to a supersonic flow field. With its applicability proven, the LIBS technique could quantify the benefit of the cavity configuration on fuel-air mixing.

4.4.2 Comparison of Baseline and Cavity Configurations

To quantify the mixing enhancement the He/O ratio at the same location and conditions for the two configurations are directly compared. The measured ratios are taken at a constant height, which was set to be in the area of highest fuel concentration for the baseline configuration. Because of this improved mixing will be represented by lower He/O ratios at the given height. This is due to the simulated fuel penetrating deeper into the flow and mixing over a wider volume of the core flow air, reducing the amount of fuel at the given height. He/O ratios are plotted for both configurations and all three flow conditions versus the spanwise distance in Figure 4.18-Figure 4.20, at the nearest streamwise location.

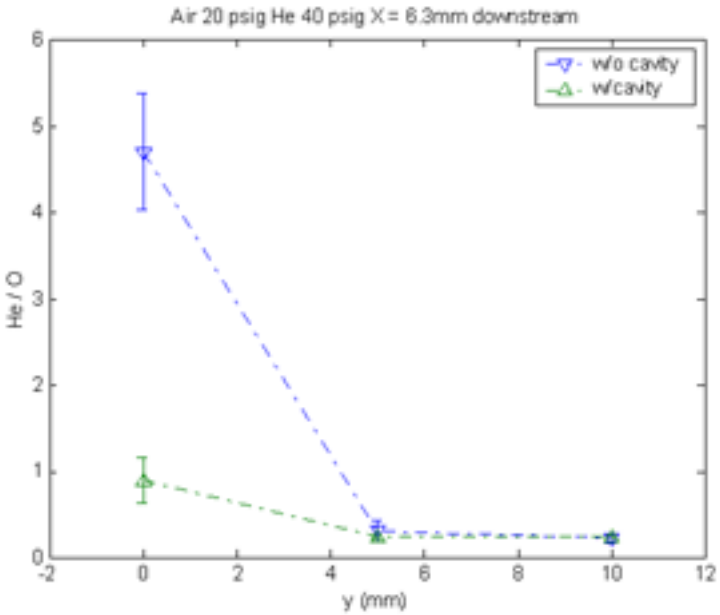

Figure 4.18: Comparison of He/O Ratio versus y for the Non-cavity and Cavity Configurations with Air = 20psig, He = 40psig, at x = 6.3mm

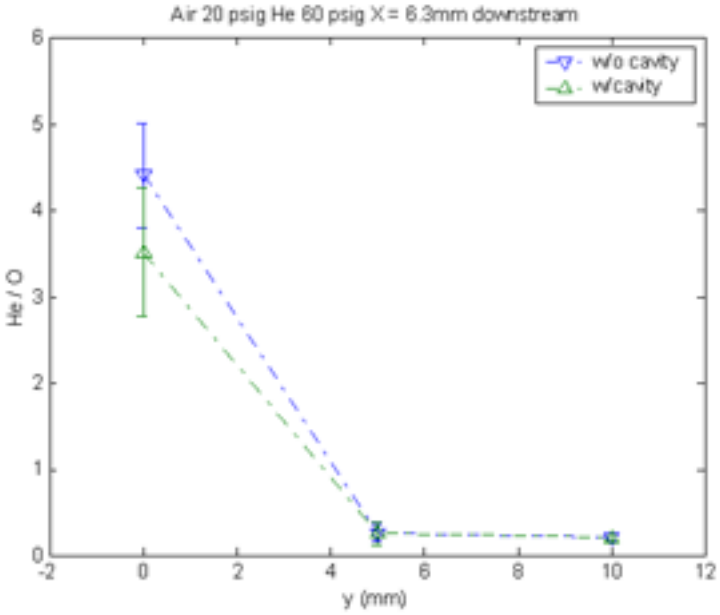

Figure 4.19: Comparison of He/O Ratio versus y for the Non-cavity and Cavity Configurations

with Air = 20psig, He = 60psig, at x = 6.3mm

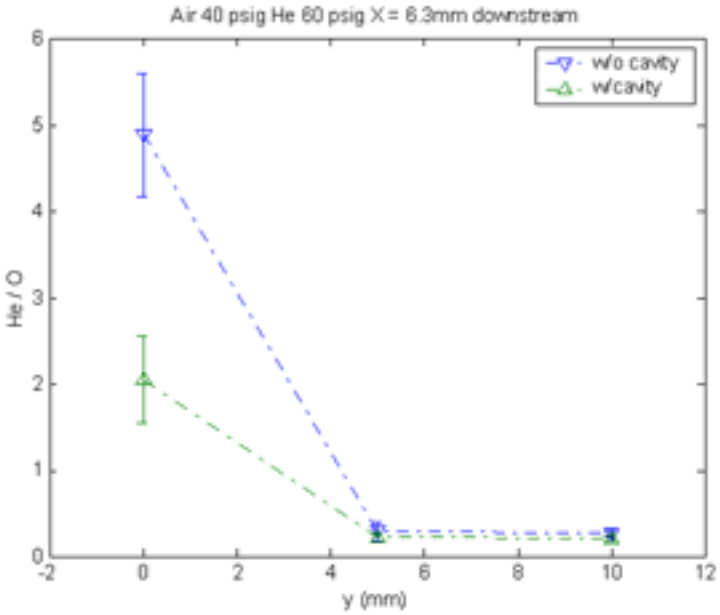

Figure 4.20: Comparison of He/O Ratio versus y for the Non-cavity and Cavity Configurations with Air = 40psig, He = 60psig, at x = 6.3mm

In all three plots the average centerline value is much higher for the non-cavity configuration as compared to the cavity configuration; only for the second case do the uncertainties overlap (however the opposing averages are not within the uncertainty limits). The gain in He/O ratio can be seen to be up to a factor of 5 for the lowest pressure case. If the outer spanwise locations are investigated for the two configurations it can be seen that their values are generally lower. However, some averages are close to one another and even lie within each other's uncertainty. Based on their low ratios it appears that the fuel has not fully convected outward to the walls at this nearest downstream location. Investigation of locations farther downstream

may reveal the spanwise effects of the large coherent structures as they are shed from the cavity. Figure 4.21-Figure 4.23 show plots for the He/O ratio for the same conditions as Figure 4.18-Figure 4.20 for the farthest downstream location investigated.

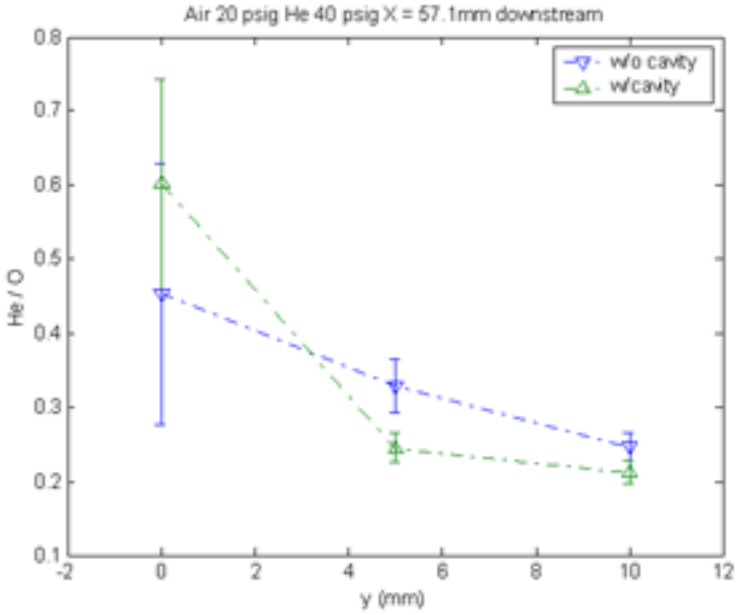

Figure 4.21: Comparison of He/O Ratio versus y for the Non-cavity and Cavity Configurations with Air = 20psig, He = 40psig, at x =57.1mm

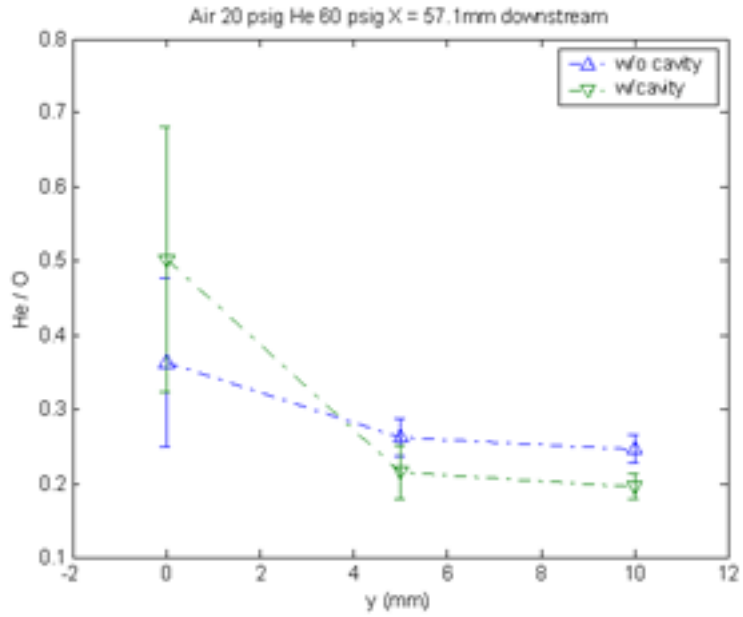

Figure 4.22: Comparison of He/O Ratio versus y for the Non-cavity and Cavity Configurations with Air = 20psig, He = 60psig, at x =57.1mm

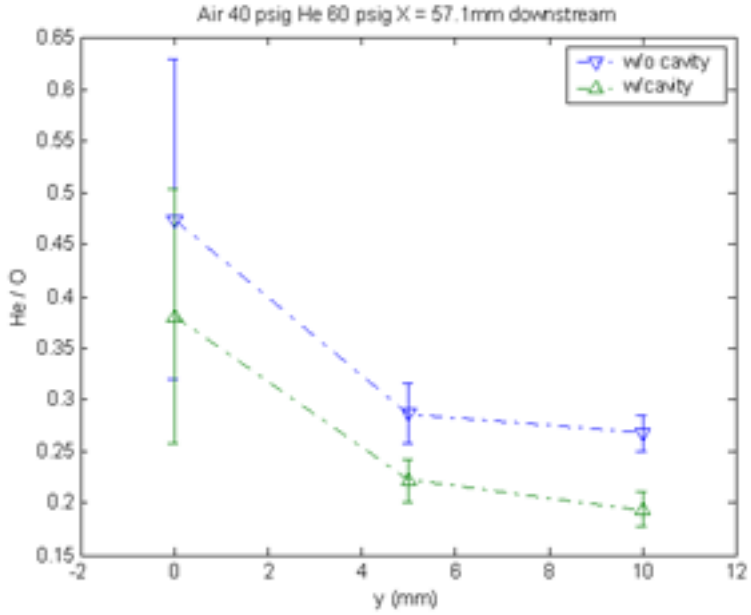

Figure 4.23: Comparison of He/O Ratio versus y for the Non-cavity and Cavity Configurations

with Air = 40psig, He = 60psig, at x =57.1mm

At the streamwise location x = 57.1mm it can be seen that the enhanced mixing effects have a more pronounced effect at the walls as compared to the values at x = 6.3mm. The centerline values have much higher uncertainties than the upstream values, which is indicative of the turbulent shear layer growth. For the two lower pressure cases it can be seen that the centerline average values are actually higher for the non-cavity case, but the two uncertainties overlap and even encompass the other configuration's average value. The general trend to quantify mixing enhancement is seen at the outer values with the cavity case having lower He/O ratios than the non-cavity case with a factor of up to 1.5. When these two sets of Figures are considered it can be seen that at the nearest streamwise location mixing effects are quantifiable at the centerline, with a single point centerline injector. The fuel then is more well-mixed downstream in regards to the spanwise direction.

4.4.3 Uncertainty Analysis

In Figure 4.18-Figure 4.23 the uncertainty bars plotted represent the statistical uncertainty of the average measurements. These bars were determined by considering the sample size, N_i, and the standard deviation of the data, σ_i. The standard error in the mean value is then determined for each atomic element:

$$\sigma_{m,i} = \frac{\sigma_i}{\sqrt{N_i}} \qquad [31]$$

where i indicates the error for the individual atomic emission line measurement.

Once the standard error of the mean is evaluated for Oxygen and Helium the standard error of the ratio can be evaluated:

$$\sigma_m = \sqrt{\sigma_O^2 + \sigma_{He}^2} \qquad [32]$$

This uncertainty is multiplied by two to produce the value for each error bar, or $2\sigma_m$. These values of uncertainty are predicated on the assumption of the central limit theory which asserts that an infinite number of samples will produce a Gaussian distribution of the data around the actual average. The standard deviation is a good measure of the variance of the data, which can be representative of the amount of turbulence apparent in the flow. Duplicate graphs of those shown in 4.4.2 are plotted in 7.5: Appendix E: LIBS Data Plots with the statistical uncertainty replaced by the standard deviation.

Uncertainty in the LIBS method itself is a function of the concentration of fuel, or alternately the He/O ratio. For the ratios represented here the uncertainty in the measurement apparatus is very small in comparison to the statistical uncertainty. Discussion of the apparatus uncertainty is again found in Temple[66].

5 Supersonic Combustion Characterization

A series of experiments were performed for the purposes of characterization of supersonic combustion in a three-dimensionally expanding test section with aspect ratio of one. First airflow through the test article was investigated utilizing the Scanivalve diagnostics described in section 3.3.2.1 with no fuel addition or combustion. These non-reacting flow cases are presented in section 5.1. Reacting flow experiments were then performed to compare with these non-reacting cases in an attempt to identify combustion characteristics. The resulting pressure trace would provide a means for conducting an analytical investigation of the combustion characteristics as described in section 2.2.3. The reacting flow experiments use a staged fuel injection system also described in the early sections of this thesis and appear in section 5.2.1. These tests utilized two fuel types, hydrocarbon and hydrogen, as well as a variety of equivalence ratios.

5.1 Non-Reacting Flow Characterization

Non-reacting or cold flow, characterization was performed for a wide range of stagnation pressures upstream of the supersonic nozzle. No mass addition in the form of fuel injection was performed for these cold flow conditions. A minimum choking pressure was approximated and then experiments were conducted starting from 20psig and running up to 130psig in steps of 10psig. For each experiment a 5.0 second duration measurement was taken by the DSA pressure module which consists

of 16 pressure channels. The combustor block contains 24 ports along the top wall and 27 ports along the back wall, so four separate tests were conducted at the same stagnation pressures to obtain data for every pressure port. These files contained approximately 240 data points for each of the channels, and were averaged to yield the static pressure at each X-location downstream. These pressures were then normalized by the stagnation pressure upstream and plotted to view the trends.

Normalized pressure plots were generated and are shown in Figure 5.1 and Figure 5.2 over the range of the test conditions for both the top wall pressure ports as well as the back wall pressure ports. In this plot stagnation pressure changes are investigated from 30psig to 130psig. Since there is no vacuum at the exhaust of this test apparatus the flow must match atmospheric pressure at some point near the test section exit. Because of this a shock will be established at some location in the flow after which the flow velocity will become subsonic. The supersonic and subsequent subsonic regions can be identified by their characteristic pressure traces. Supersonic flow in an expanding duct will have a negative, or favorable, pressure gradient with respect to the flow direction. However, subsonic flow in an expanding duct will have a positive, or adverse, pressure gradient with respect to the flow direction.

When the pressure plots for the combustor block are investigated it can be seen that the lower pressures, below 90psig, follow the subsonic expansion line almost immediately. In Figure 5.1 for the top wall pressure port measurements this is presented as each pressure trace follows a different subsonic expansion line. As upstream stagnation pressure is increased supersonic region is longer and the shock is

pushed downstream. This is most evident in the 130psig case where the pressure gradient is favorable until approximately 2 inches downstream after which the normalized pressure begins increasing. Figure 5.2 shows the same plot for the back wall pressure ports.

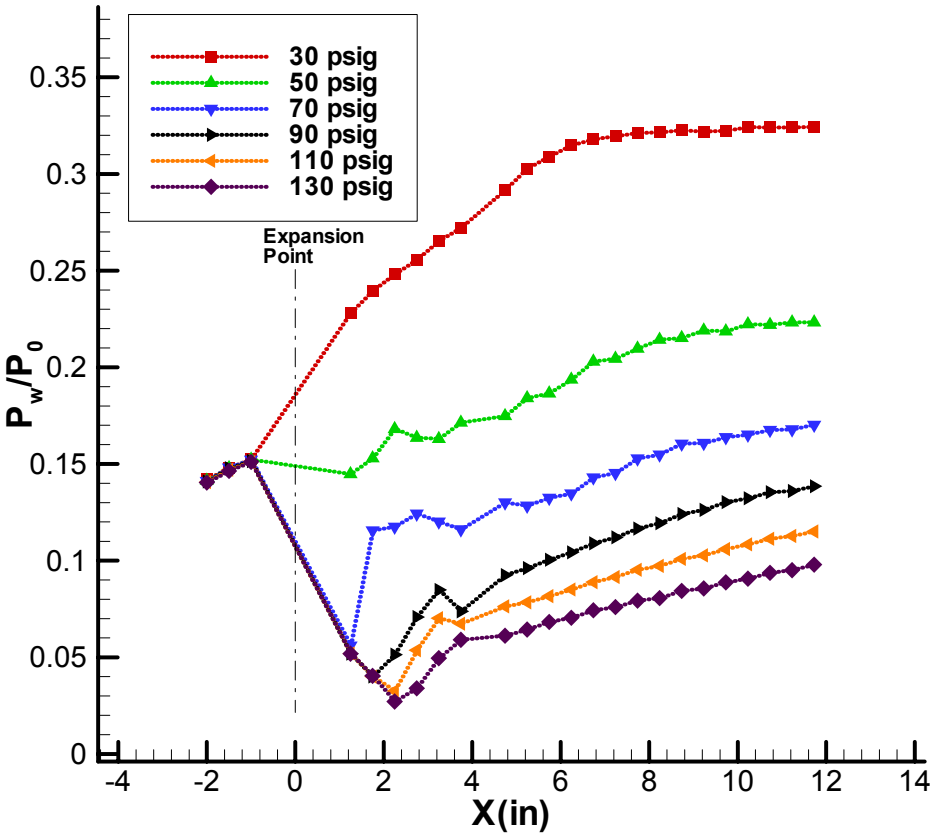

Figure 5.1: Normalized Pressure Profile for Multiple Upstream Stagnation Pressures versus Axial Distance, Non-Reacting Cases, Measured by the Top Pressure Ports

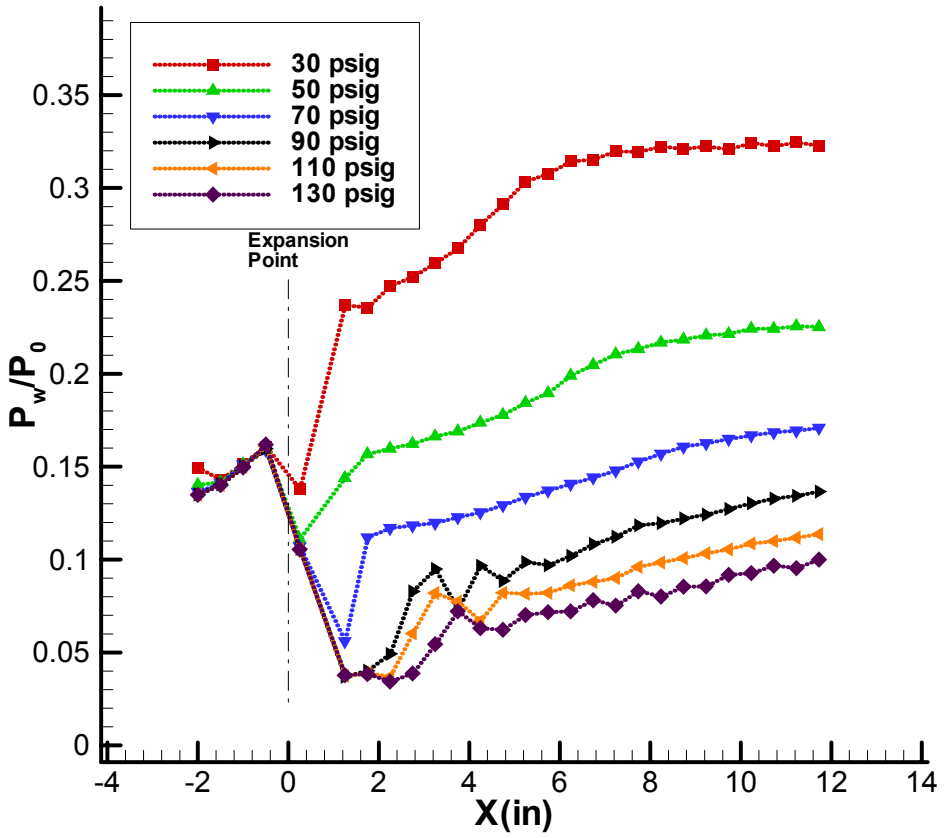

Figure 5.2: Normalized Pressure Profile for Multiple Upstream Stagnation Pressures versus Axial Distance, Non-Reacting Cases, Measured by the Top Pressure Ports

It is of interest to note that the top wall and back wall traces exhibit a fair amount of difference indicating that the flow is not uniform. This is most likely caused by the two dimensional throat and nozzle. The back wall pressure traces display the same trends with the low pressure cases of almost purely subsonic characteristics. Due to these findings the operational limits of the test article will be restricted for reacting flow cases from 90-130psig. Also, this severely restricts the data resolution since

only a very short distance is supersonic in the test section and the pressure port spacing is fixed. Recommendations for future work and considerations of this problem will be discussed in Chapter 6. A closer view of the pressures of interest, in the non-reacting test conditions, is presented in Figure 5.3 and Figure 5.4 for the top wall and back wall pressure ports, respectively.

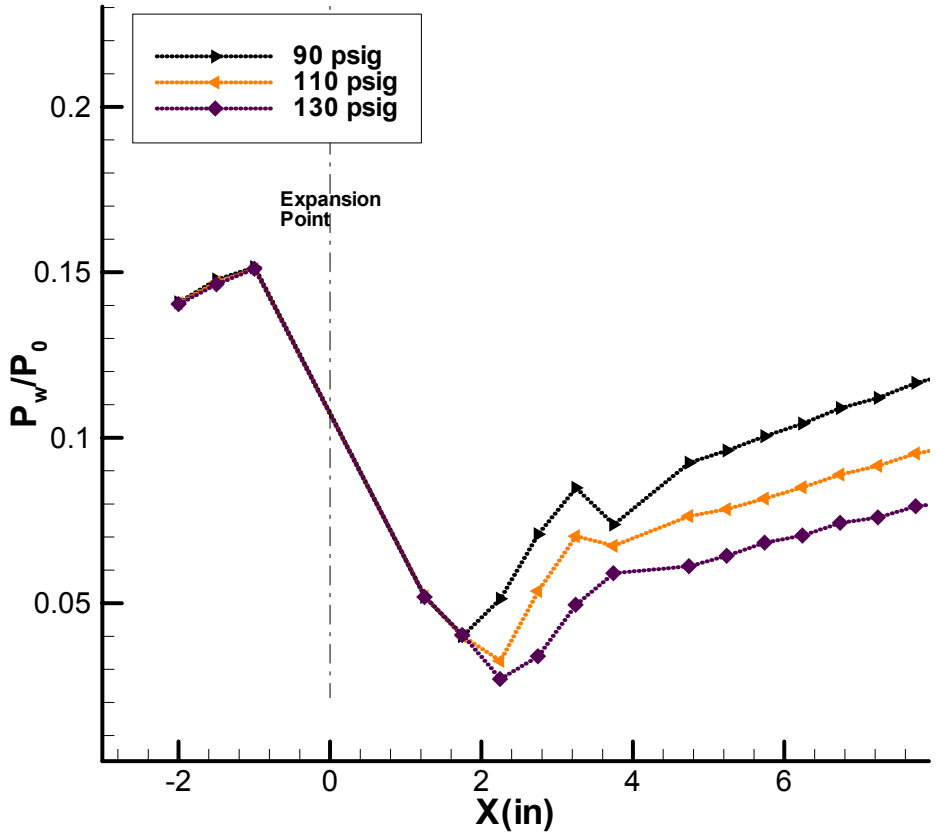

Figure 5.3: Normalized Pressure Profiles for Upstream Stagnation Pressures with Supersonic Regimes versus Axial Distance, Non-Reacting Cases, Measured by the Back Pressure Ports

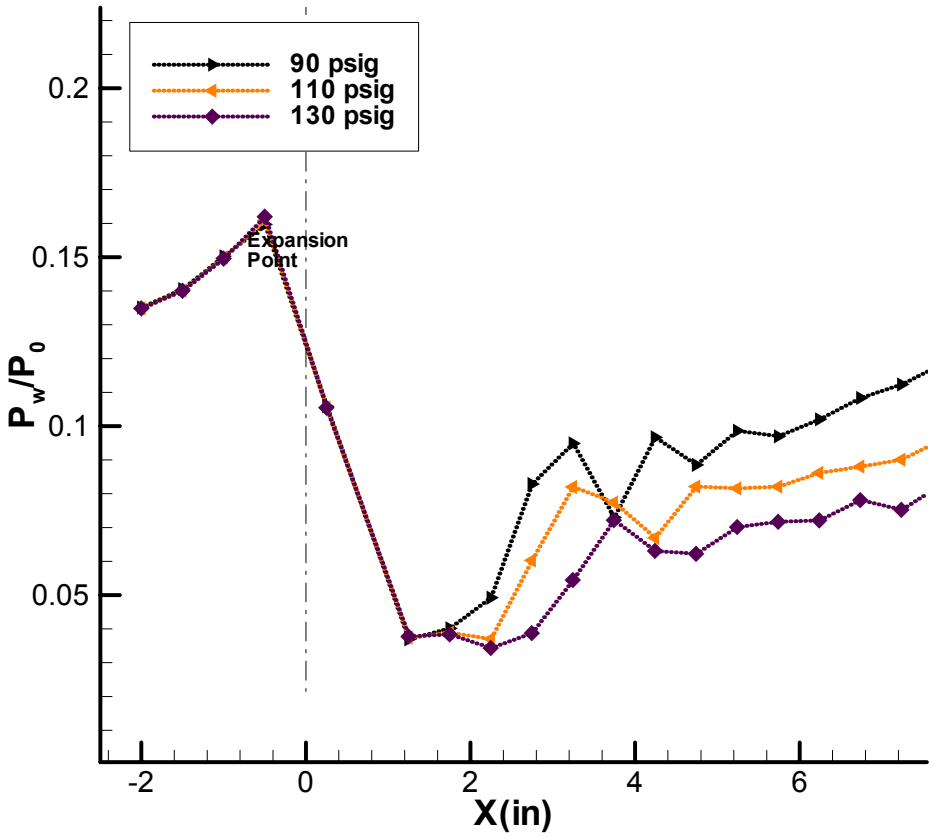

Figure 5.4: Normalized Pressure Profiles for Upstream Stagnation Pressures with Supersonic Regimes versus Axial Distance, Non-Reacting Cases, Measured by the Back Pressure Ports

With the baseline cold flow pressure characterization performed the reacting flow experiments could be conducted and compared to these non-reacting cases. These comparisons generate the combustion characteristics of the specific test article.

5.2 Reacting flow characterization

Reacting flow cases were conducted for only the higher pressure conditions

due to the operability range of the test article as described in the previous section. The igniter system described in 3.3.1 was utilized to produce the pilot flame for the staged fuel injection studies. This pilot flame was established using ethylene fuel, which was beneficial for monitoring purposes as the flame can be visualized by traditional optics. Two main fuels, ethylene and hydrogen, were investigated in the staged fuel injection configuration.

5.2.1 Staged Fuel Injection Studies

The procedure for the staged fuel injection testing is described in 3.3.3.1, however a brief revisit in the geometry is beneficial. A pilot flame is established at the second injection point which was placed approximately 1.75 inches downstream of the expansion point. The pilot flame is injected with a stoichiometric equivalence ratio of ethylene and air. The main fuel is supplied via the first injector point approximately 0.75 inches downstream of the expansion point, or 1.0 inches upstream of the pilot flame. The injection point diameter of 0.1 inch acts a choked orifice and the pressure of the injected fuel is altered to produce a variety of equivalence ratios. Equivalence ratio calculations were performed to give the overall equivalence ratio with respect to the core supersonic mass flow. Once the pilot flame was established the main fuel, either ethylene or hydrogen, was brought on and measurements were taken. Visual monitoring was taken via the CCD camera, and OH* chemiluminescence monitoring was conducted for the hydrogen fuel tests. The apparatus for these systems is described in Chapter 3. Pressure measurements were

taken as in the cold flow cases and compared.

5.2.1.1 Ethylene Main Fuel

Ethylene main fuel experiments were conducted for equivalence ratios of 0.3, 0.4 and 0.5 at upstream stagnation pressures of 90, 110, and 130 psig. Runs were also performed with: i.) only the pilot flame burning with no main fuel addition and ii.) full fuel mass injected under non-reacting conditions (i.e. pilot flame uninitiated).

Very little visible burning was evident in the monitoring of these cases, although a noticeable geometry change in the pilot flame was observed. For all equivalence ratios the burning efficiency was determined to be very low as evidenced by the lack of flame propagation outside of the pilot flame region. Pressure traces taken reveal that very small amounts of combustion were occurring, however the change in pressure is minimal with respect to the equivalence ratio. For these experiments the pressure port configuration was re-oriented to investigate the areas of supersonic flow. The pressure measurements were thus taken on the back wall and top wall at the same time, with eight ports on each being monitored for the same test. Pilot flame and fuel injection were performed from the top wall, for which reason access to the ports nearest the injectors was restricted. Therefore, the back wall pressure traces, which contain the axial port locations directly in front of, in between, and behind the injectors, are of the most interest.

Figure 5.5 shows the normalized pressure plot versus axial distance with the core flow at 110 psig and all of the fuel conditions. In this plot the difference

between the pilot/cold flow cases and all the cases with the main fuel injection are evident. At a location of approximately 1.25 inches a significant difference in normalized pressure of about 0.02 is seen between these two flow conditions. The rest of the plot is somewhat cluttered and will be broken down in subsequent plots to analyze specific trends. However, one trend is obvious, that all of the considered burning cases, including the pilot only case, shock to subsonic flow conditions farther downstream than the cold flow case. This indicates that some amount, albeit very small, of supersonic combustion is occurring in these cases and the additional energy deposited in the flow is helping it to remain supersonic for a longer distance. On the plot this is seen where the cold flow case (in red) has an positive pressure gradient beginning at approximately 2.25 inches whereas the other cases do not exhibit an positive pressure gradient until after approximately 2.75 inches.

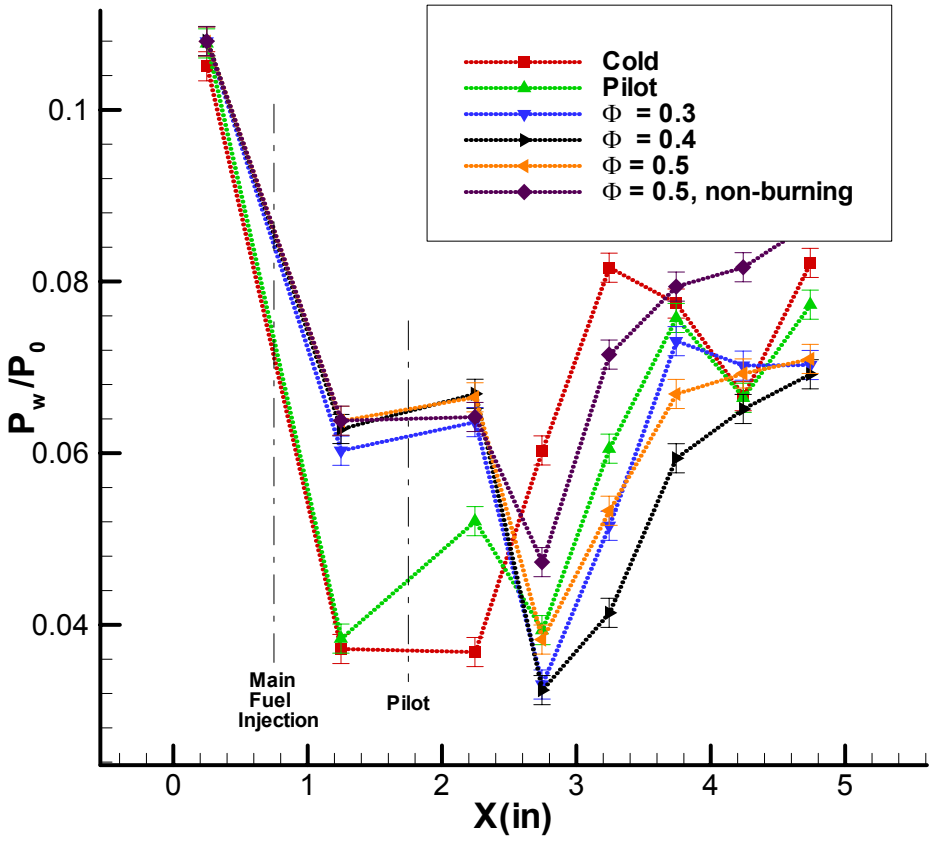

Figure 5.5: Normalized Pressure Profile for Upstream Stagnation Pressures of 110psig versus Axial Distance, Ethylene Main Fuel Cases, Measured by the Back Pressure Ports

When the areas directly around the injection points are investigated to compare the burning and non burning cases (specifically for the highest equivalence ratio) it is obvious that the effects of combustion are very small in this system. Figure 5.6 shows the comparison of burning and non-burning at an equivalence ratio of 0.5 for the same conditions as Figure 5.5, zoomed in on the area of interest along with the cold flow and pilot flame data points.

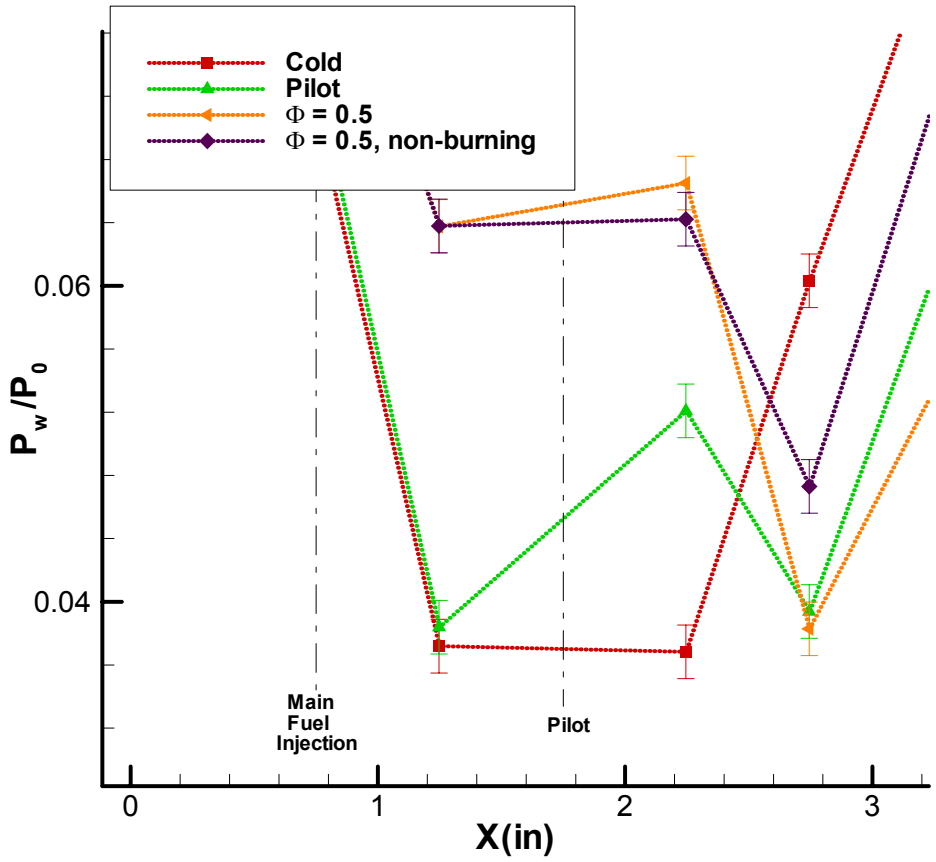

Figure 5.6: Normalized Pressure Profile near injectors for Upstream Stagnation Pressures of 110psig versus Axial Distance, Ethylene Main Fuel Cases, Measured by the Back Pressure Ports

At the axial location of 2.25 inches the differences between the cases are clear, although very small. The additional pressure rise due to the pilot flame, and subsequent main fuel mass flow and main fuel burning can be seen as these values of normalized pressure are consecutively higher. This clearly indicates a pressure addition in the burning case and thus supersonic combustion. Expected pressure distributions, however, would be up to an order of magnitude higher which indicates

the extremely small amount of fuel being reacted within this system. A very small amount of fuel reaction indicates poor combustion efficiency. Three main factors of this inefficiency are theorized to be: i.) the chemical reactivity of the fuel, ii.) mixing inefficiencies, or iii.) the low enthalpy nature of the test facility. Hydrogen fuel was later investigated to evaluate the mixing efficiencies on a qualitative level for these reasons.

The uncertainty bars shown in these plots are the measurement uncertainty as defined by the manufacturer of the DSA module. Statistical errors in the measurements were calculated by the methods outlined in 4.4.3, however were so small in magnitude they were omitted. For reference the largest statistical uncertainty was on the order of 1E-8 for the normalized pressure data. Normalized pressure data never went below the order of 1E-2, thus the statistical uncertainty is 6 orders of magnitude smaller than the measured values. The measurement uncertainty was found to be a more substantial value, one order of magnitude smaller than that of the normalized pressure data minimum.

The higher stagnation pressure of 130psig was also evaluated for these testing conditions and pressure plots were produced. These graphs are presented in Figure 5.7 and Figure 5.8. Trends in these graphs mirror those of the 110psig case in that the effect of fuel addition is clear but very minute. Also it should be noted that higher equivalence ratios do not seem to have a large effect on the pressure characteristics which implies that additional fuel does not react. These preliminary signs point towards mixing issues which were further investigated by first altering the fuel type.

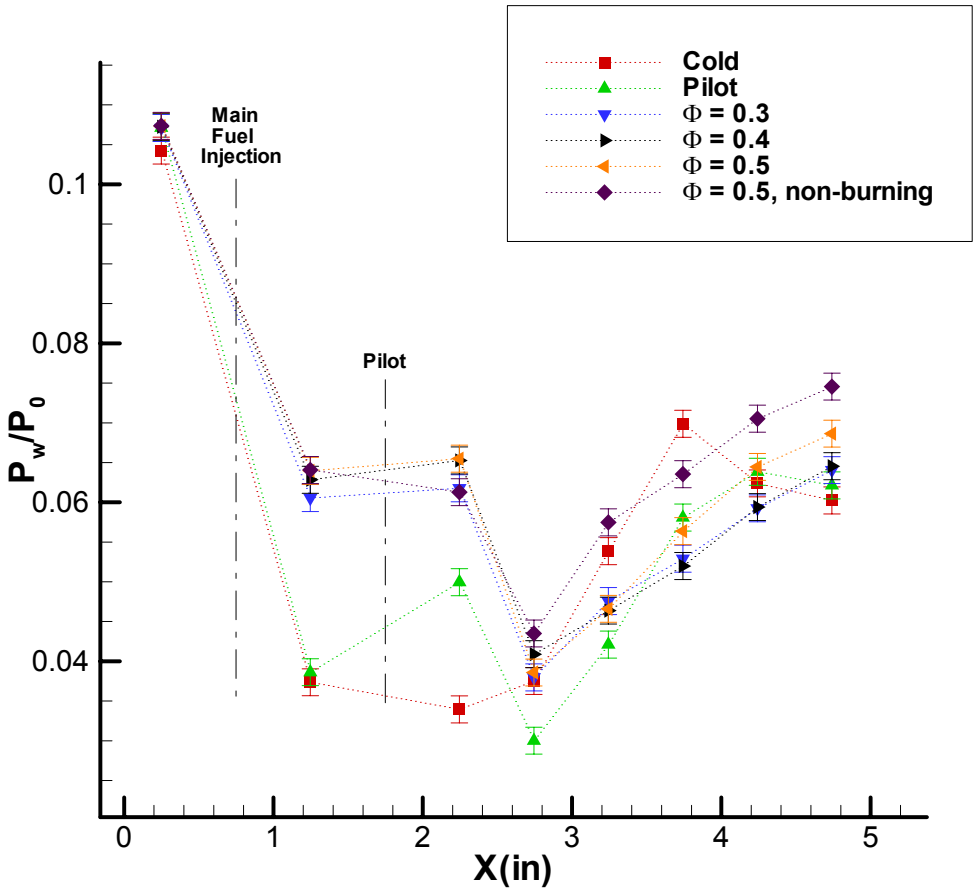

Figure 5.7: Normalized Pressure Profile for Upstream Stagnation Pressures of 130psig versus Axial Distance, Ethylene Main Fuel Cases, Measured by the Back Pressure Ports

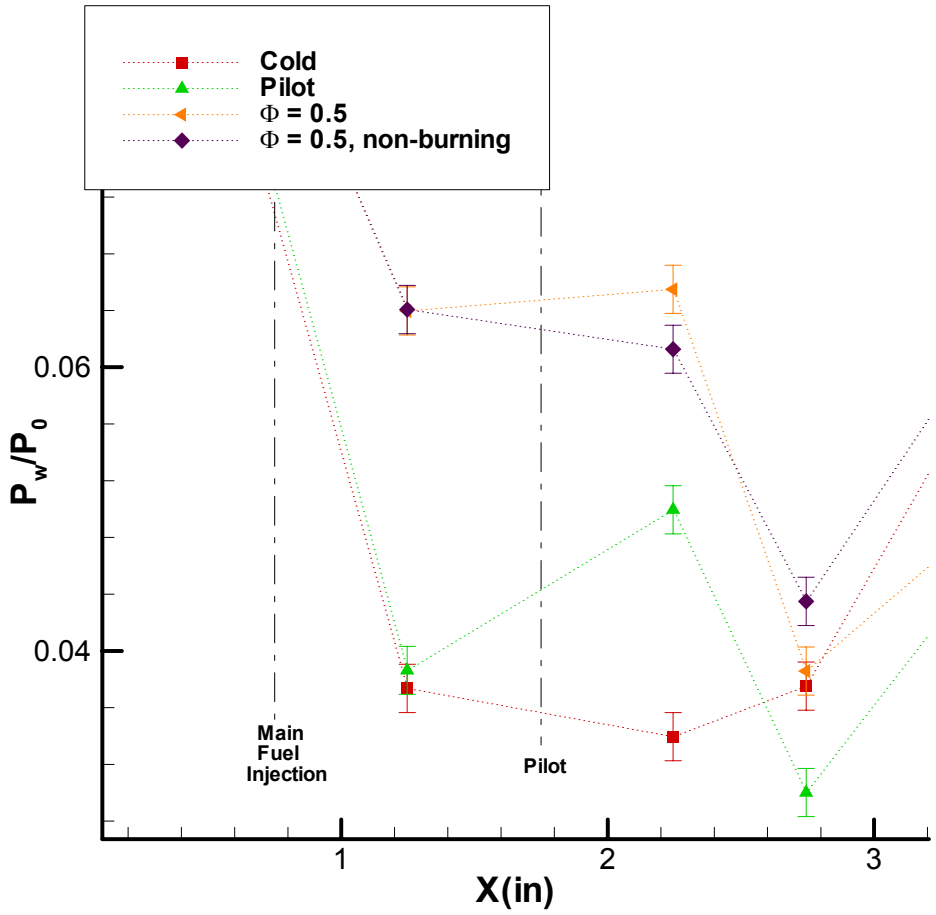

Figure 5.8: Normalized Pressure Profile near injectors for Upstream Stagnation Pressures of 130psig versus Axial Distance, Ethylene Main Fuel Cases, Measured by the Back Pressure Ports

5.2.1.2 Hydrogen Main Fuel

To provide insight into the reasons behind the low combustion efficiency of the hydrocarbon fueled tests a more reactive fuel was investigated. If hydrogen fuel provided considerably better combustion characteristics the problems encountered in the previous reacting flow experiments would be evident as chemical reactivity issues

associated with the hydrocarbon fuel. However, if the pressure traces and visual monitoring showed little increase in combustion the problems would most likely be associated with mixing or enthalpy and thus the experimental apparatus itself. Hydrogen fuel was injected through the main fuel orifice at equivalence ratios of 0.05, 0.075 and 0.10 at only the highest pressure case to investigate the combustion qualities. A plot of the back wall pressure port measurements are presented in Figure 5.9 and can be compared with Figure 5.7 for the ethylene testing.

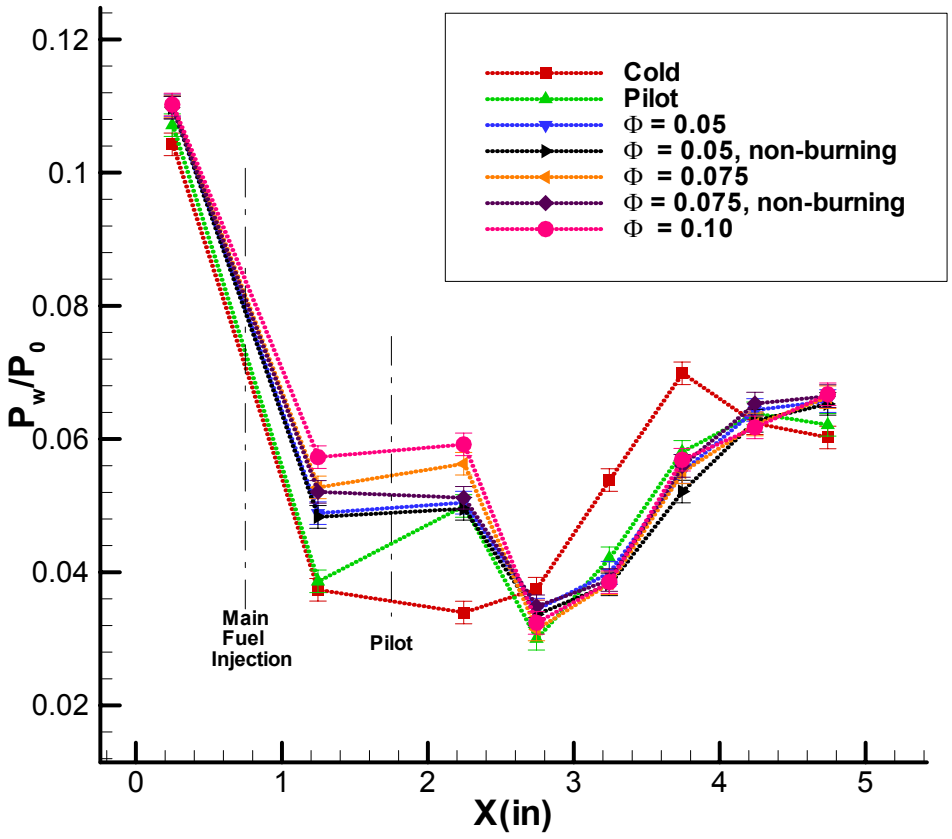

Figure 5.9: Normalized Pressure Profile for Upstream Stagnation Pressures of 130psig versus

Axial Distance, Hydrogen Main Fuel Cases, Measured by the Back Pressure Ports

The hydrogen has a more clear effect than that of the ethylene fuel which is a product of its lower activation energy. However, the affects are still not significant and the majority of the pressure rise can be attributed to mass addition. These results correspond to the same trends shown for the ethylene tests. Again the interest area is looked at closer in Figure 5.10 (for ER=0.075) and distinct effects are evident of mass addition and burning, but are very minute in comparison to expected results.

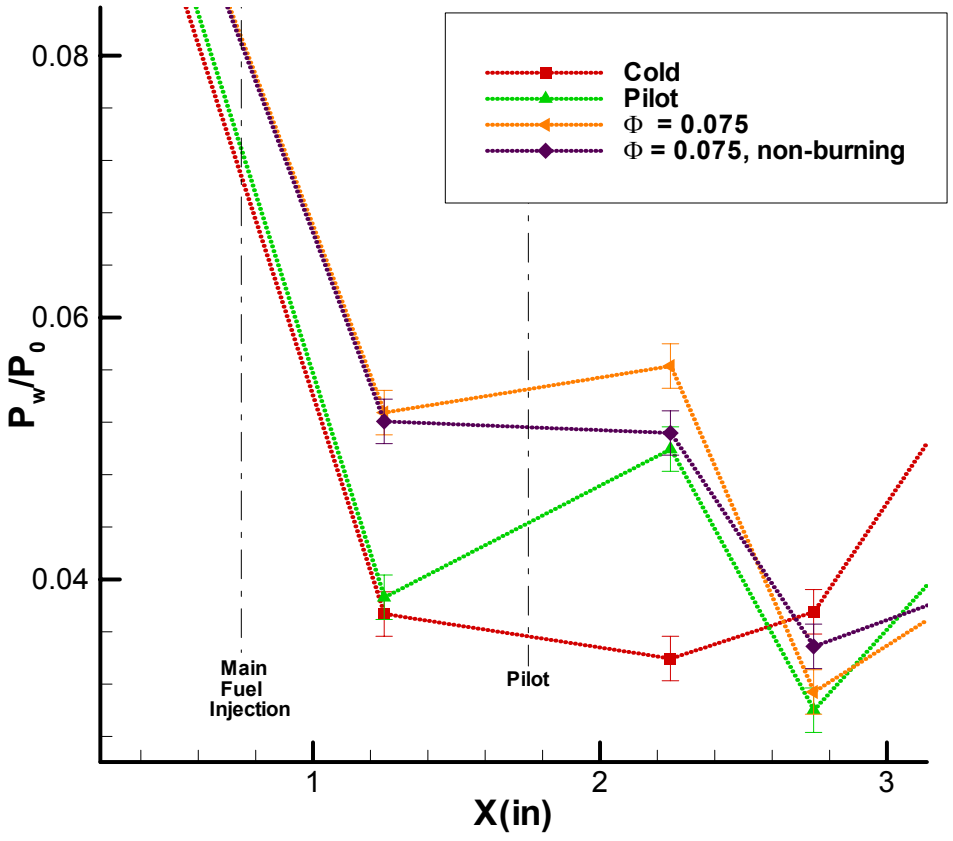

Figure 5.10: Normalized Pressure Profile for Upstream Stagnation Pressures of 130psig versus

Axial Distance, Ethylene Main Fuel Cases, Measured by the Back Pressure Ports

OH* chemiluminescence monitoring was taken for the hydrogen cases since the primary emission of H_2-Air reactions is in the ultra-violet range and cannot be visualized with the CCD camera. OH* chemiluminescence was performed using an ICCD camera and a long, time averaged, shutter speed of 0.1s. Images were averaged to produce brighter pictures of the flame front structure. Since OH* emission represents the area of highest reaction it is a good indicator of flame propagation and reaction zones. An image comparing the pilot flame OH* emission and the OH* emission with the main fuel on is seen in Figure 5.11.

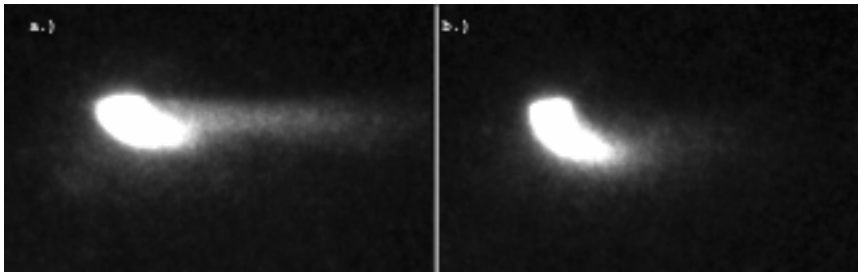

Figure 5.11: Chemiluminescent Images of a.) Pilot Flame and b.) Pilot Flame with Main Fuel Addition for Hydrogen Staged Fuel Testing

Here it is obvious that the effect of fuel addition is very minor. These findings confirm that the problem is not one of fuel reactivity and it was theorized that the staged fuel injection is not providing areas of favorable temperature and concentration for combustion at coincident points. The main fuel injection may be penetrating deeper into the core flow such that the highest fuel concentration is at a height above the pilot flame where only a small percentage of the fuel injected is

contacting the area of sufficient temperature from the pilot flame to enable reaction. A sketch of these trajectories and their associated concentration and temperature profiles is shown in Figure 5.12. Although this is the believed reason for poor combustion, providing conclusive proof is difficult due to a lack of line of sight visibility which prohibits use of many flow visualization techniques. In order to fully explore the combustion issues, therefore, a number of different methods should be investigated. Other possible problems are: a lack of flame holding in the staged system due to the small size of the injector ports and their relatively large spacing, and an overall deficiency in activation energy available due to the low enthalpy conditions.

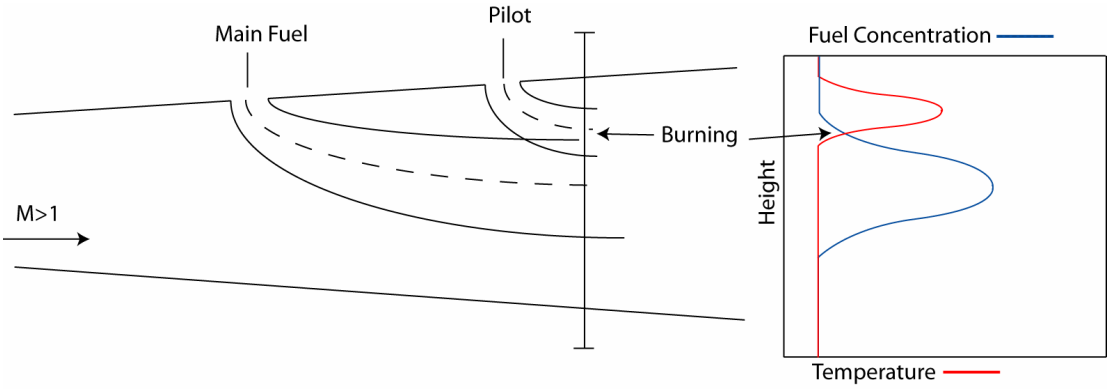

Figure 5.12: Theorized fuel and pilot flame trajectories and relative concentration / temperature profiles at their intersection

Due to the findings of the staged hydrogen fuel experiments it was decided that the fuel injection configuration had to be altered to completely identify the combustion issue as one of mixing inefficiency. Suggested reconfigurations include a

single-point injection of a fuel-rich plume. This may allow the fuel to be preheated and be more prone to react with the core airflow. It is suggested that such a system utilize a larger injection port to increase penetration and flame length as well as avoid chamber pressure issues. A further investigation into the reconfiguration of the fuel delivery system is discussed in section 6.3.

6 Summary and Conclusions

A set of two separate experimental investigations were performed to explore fundamental areas of scramjet development. The first experiment attempted to further the quantification of mixing enhancement by flow-induced cavity resonance. In these tests novel diagnostic techniques were implemented and fuel/air ratios were quantified at discrete points in the flowfield. The mixing benefits of a cavity mixing system were thus proven. The second investigation was conducted with the goal of characterizing a baseline supersonic combustor with an aspect ratio of one, developed for a low-enthalpy ground test facility. This investigation was predicated on the idea that scramjet development inevitably will result in the use or testing of novel combustion geometries, many of which utilize low aspect ratio flowpaths. With this in mind experiments were performed to analyze the combustion characteristics of an expanding, square combustor from which future investigations of non-traditional geometries could be compared. Many key issues were identified and explored and the resulting baseline configuration was determined to be unsatisfactory in combustion qualities.

6.1 Cavity Mixing Enhancement

Cavity mixing enhancement studies were conducted in a supersonic duct with design Mach number of 2.0 and with a cavity of L/D ratio of 4. Qualitative investigations were performed utilizing Schlieren visualization, at both high and low

shutter speeds. The high-speed imaging resulted in images of clearly defined coherent structures, which were shown conclusively to convect downstream from the trailing edge of the cavity. Individual structures were discernible in these images due to the shutter speed being substantially higher than the shedding frequency of the cavity itself. Portions of the structures were averaged, though, due to extremely high local velocity. In spite of this averaging the convecting structures are clearly identified at multiple locations downstream of the cavity in both individual frames and subsequent frames. The framing rate available was insufficient to allow tracking of individual structures; however individual frames are sufficient to demonstrate the structures convection. Conclusive proof of downstream convection provides insight to the mixing mechanism of this system and supports previous findings.

Time averaged Schlieren images were evaluated using image processing software which developed quantitative indications of fuel injection trajectories. These images, once analyzed, demonstrated that the cavity case increased the fuel injection penetration and mixing by tracking the transverse intensity gradient along the streamwise direction. Since the intensity gradient is related to the density gradient, it can be used as a quantitative measure of spreading rate in the flowfield. The resulting intensity maps support the observations taken from high-speed Schlieren and provide a means of mapping the fuel injection qualitatively. These techniques could be beneficial in quantitatively mapping fuel injection in other systems to provide insight into the fuel delivery dynamics. Furthermore they provide a means of deriving quantitative information from typically qualitative Schlieren

optical methods.

Dynamic pressure measurements were also performed to quantify the shedding frequency and confirm the cavity characteristics with the theoretical models. These measurements demonstrated that the shedding frequency matched with reasonable accuracy those predicted by Rossiter[44]. A shedding frequency of approximately 20 kHz was identified for the upstream stagnation pressures of interest. Dynamic pressure measurements were conducted across a wider range of upstream stagnation pressures, outside the range of interest for the cavity mixing investigations. These experiments revealed a mode-hopping phenomenon within the system. The values match with the model at the first harmonic, in contrast to the lower pressure investigations. This mode hopping phenomenon and the criterion for various mode selection process are of interest to study in the future. For the purposes of this investigation the second harmonic was dominant and the experimental and theoretical observations were in agreement.

Laser Induced Breakdown Spectroscopy (LIBS) was the third diagnostic technique performed on the test article. This application of LIBS is the first known application to a supersonic flow condition. LIBS provides discrete, rapid, in-situ measurements of elemental concentrations which are of great benefit to the scramjet application. Requiring only single point optical access this diagnostic technique allows for the quantitative measure of fuel/air ratio which is the key parameter in determining mixing. As applied to the cavity mixing experiments LIBS revealed the significant three-dimensional qualities of the mixing flowfield which could not be

realized by previous line of sight diagnostic techniques. Furthermore the LIBS data showed significant reductions in fuel/air ratio at a given height in the test section for the cavity configuration as compared to the non-cavity configuration. With constant mass flows of fuel a lower fuel/air concentration at a constant height indicates that fuel has penetrated deeper or dispersed across a wider area. These are quantitative indications of enhanced mixing and the differences in fuel/air ratio between configurations were seen to be as high as five fold. This result confirms both the benefits of cavity mixing enhancement quantitatively as well as proves LIBS as a robust diagnostic technique which could be beneficial in future scramjet testing and development.

6.2 Supersonic Combustion Characterization

Supersonic combustion characterization experiments were conducted in an expanding area duct with an aspect ratio of unity. The goal of these experiments was to develop baseline data for a square geometry to which future experimental geometries' combustion characteristics could be compared. Initial testing indicated that for hydrocarbon testing some form of secondary fuel injection would be necessary to test a wide range of fuel/air ratios. Both hydrocarbon and hydrogen fuels were of interest due to the various applications of scramjet technology. A robust baseline model would include multiple fuels and potentially various flow properties. Both of these aspects were initially investigated by changing fuel type and varying upstream stagnation pressures. Static pressure measurements were taken

along the length of the test section for a wide range of upstream stagnation pressures to characterize the non-reacting flow. Pressure profiles along the axial distance of the flowpath were produced by these measurements. These experiments revealed the operational limits of the test article to be narrower than expected, only achieving supersonic flow for a substantial distance of the expanding section at the higher upstream stagnation pressures.

With these conditions identified by the cold flow characterization the combustion experiments were performed utilizing a staged hydrocarbon fuel delivery system. These experiments resulted in evidence of supersonic combustion; however, the effect of changing fuel-air ratio was weak suggesting poor combustion efficiency. Furthermore, only a few normalized pressure data points could be obtained for these cases, and curve fitting these points for analysis would incur large amounts of uncertainty. Thus, the combustor appeared unsuitable to be used as a baseline configuration. Three possible causes of poor combustion efficiency were discussed. They are: a lack of chemical reactivity due to the hydrocarbon fuel, a lack of sufficient mixing provided by the staged fuel injection, and an overall lack of reactivity due to the low enthalpy conditions. Studies with hydrogen fuel were then performed to investigate these possibilities.

Hydrogen fuel experiments provided similar results as the hydrocarbon fuel investigations and confirmed that the deficiency might be due to a lack of mixing by the staged fuel injection. The issue is compounded by the low-enthalpy nature of the flow facility which requires that the high temperature zone created by the pilot flame

must coincide with an area of favorable fuel/air mixture. These issues need to be addressed in order to obtain efficient supersonic combustion, which must precede the development of the baseline combustor and its characterization.

6.3 Contributions

The significant contributions of these experimental studies are:

- In cavity-induced mixing enhancement, coherent structures are conclusively shown to convect downstream from the trailing edge of the cavity. This finding is consistent with the physical model and mechanism suggested previously.
- Laser Induced Breakdown Spectroscopy was applied to supersonic flow conditions for the first time. This diagnostic was used to quantify the dispersion of simulated fuel, He, which was injected into supersonic air flow. The technique is non-intrusive and can quantify the He/O ratio within the flow
- Quantitative comparisons of fuel injection trajectory based on density gradient were derived from qualitative, time-averaged Schlieren images. This tool shows promise in providing alternative quantitative analysis from traditionally qualitative Schlieren images.
- A supersonic test bed was designed, fabricated, and installed on the reacting flow stand in Maryland's Advanced Propulsion Research

Laboratory. The results expanded the combustion testing capability at the University of Maryland.

- Supersonic combustion was achieved utilizing a staged fuel injection strategy. However the results showed that the prescribed staged fuel injection system could be unsuitable for future experimental comparisons. A redesign of the fuel injection system and an increase in the system enthalpy could be necessary to promote more efficient combustion.

6.4 Recommendations & Future work

Cavity mixing enhancement experiments investigated the benefits of this mixing technique by quantifying the fuel/air ratios at specific locations. These experiments also investigated the mechanisms by which the fuel-air mixing enhancement was achieved. Although there is a clear gain in fuel-air mixing, the associated losses must also be considered to analyze the potential benefits. Most notably the pressure loss which may result from mixing enhancement should be quantified. This metric will determine whether or not the combustion gains by increased fuel mixing, and associated shorter combustor advantages, could outweigh the losses incurred by the cavity itself. Experiments of this nature would be the next logical step in the investigation of application of cavity induced resonance to scramjets as a mixing enhancement device.

The cavity mixing experiments were also conducted in a non-reacting flow facility under low enthalpy, off-design conditions. An interesting point of further

investigation may also be that of flight conditions, or increased enthalpy, on the cavity performance. Lastly, a reacting flow experiment to compare cavity and non-cavity combustion characteristics is of the utmost interest and has the closest link to application on a scramjet system.

Combustion characterization experiments have revealed the need for redesign of the fuel delivery system. It is believed that areas of favorable fuel concentration are not coincident with areas of high temperature in the flowfield. For this reason it is suggested that impinging or single point fuel delivery systems are considered in the redesign of this test article. While these solutions may resolve the mixing issues, the low enthalpy characteristics of the system may still prohibit the efficient burning in the test section. For this reason it is also recommended that some form of pre-heater is installed on the upstream air supply. This would raise the stagnation temperature of the airflow and increase the enthalpy of the system.

The expansion of operational limits may also be of interest to investigate multiple design points in reference to core mass flow in the test section which is representative of theoretically different flight altitudes. This can be achieved by reducing the overall expansion angle, which would result in a longer supersonic test region. It should also be noted that improved combustion may push this supersonic region farther downstream, in turn expanding the operation limits of the test article. Another solution is found in tightening the resolution of the static pressure ports. Currently 0.5 inch spacing is utilized to allow for more than adequate machining tolerances, these clearances can be reduced and a more thorough pressure profile may

be the result.

Future investigations will be conducted to evaluate novel geometries developed by design methods such as streamline tracing. These geometries will be tested utilizing the same fuel injection geometry as the square test section and at the same flow conditions to allow comparison. In this means issues such as corner effects and overall combustion characteristics will be analyzed for the novel geometries for the first time experimentally. These initial investigations will provide useful insight to direct future, full-scale, high-enthalpy ground testing as well as potential flight testing of new scramjet designs. Fundamental investigations into these geometries and their respective combustion qualities will be important to the progression of scramjet technology development.

7 Appendices

7.1 Appendix A: Switch Box Control System

Shown below is the wiring diagram for the electronic valve control system which was custom fabricated for the laboratory applications presented in this thesis.

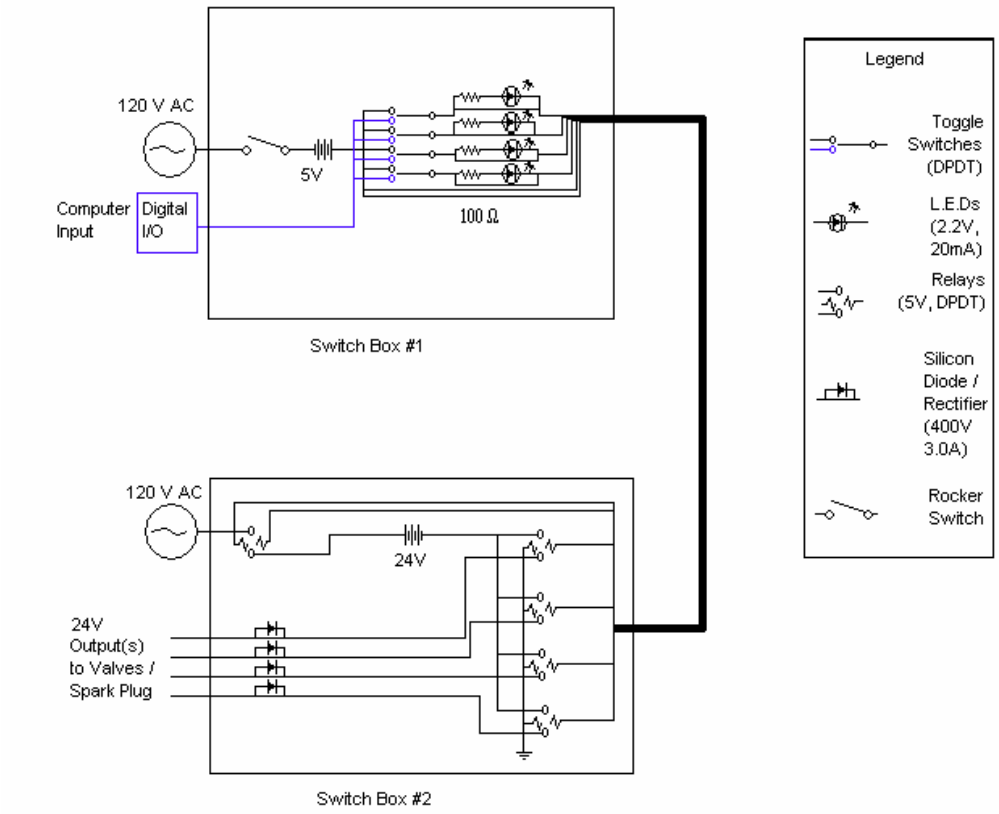

Figure 7.1: Wiring Diagram of Switch Box Control System

7.2 Appendix B: Time Histories for High Speed Schlieren

7.2.1 Appendix B-1: Optical Configuration #1

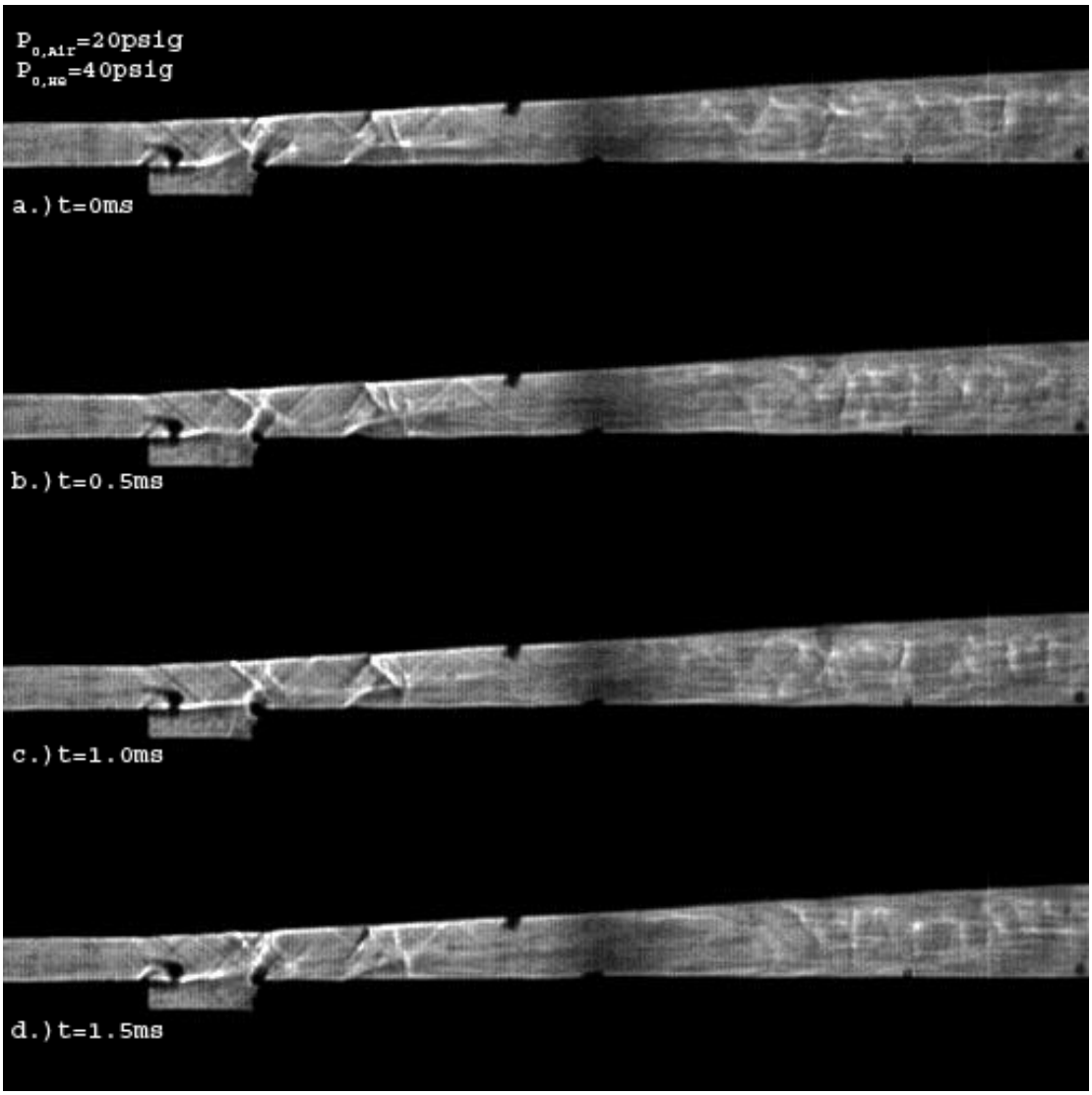

Figure 7.2: Schlieren Images of Cavity Configuration, Optical Configuration #1 for Air=20psig, He=40psig at a.) 0ms b.) 0.5ms c.) 1.0ms d.) 1.5ms

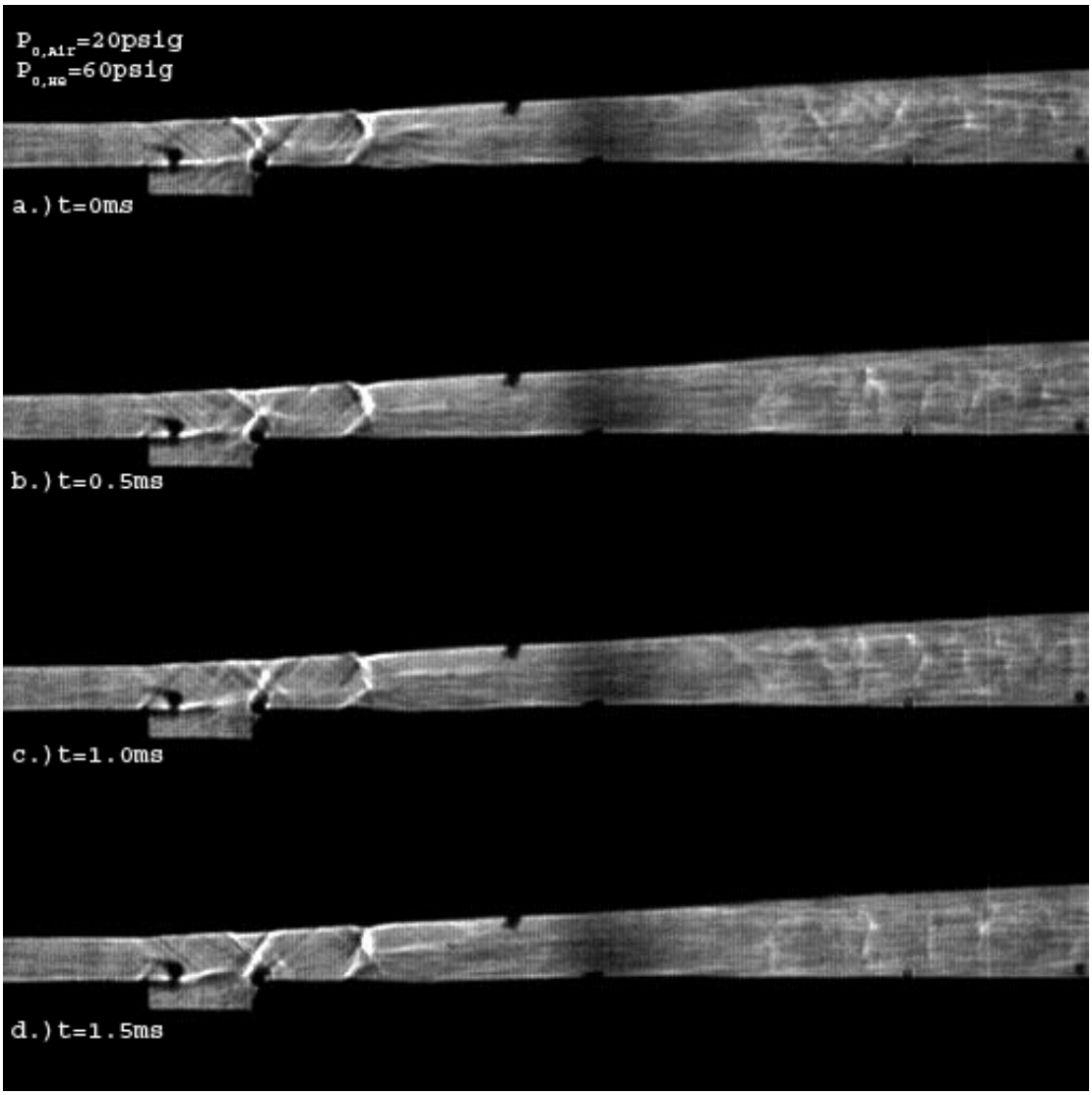

Figure 7.3: Schlieren Images of Cavity Configuration, Optical Configuration #1 for Air=20psig, He=60psig at a.) 0ms b.) 0.5ms c.) 1.0ms d.) 1.5ms

7.2.2 Appendix B-2: Optical Configuration #2

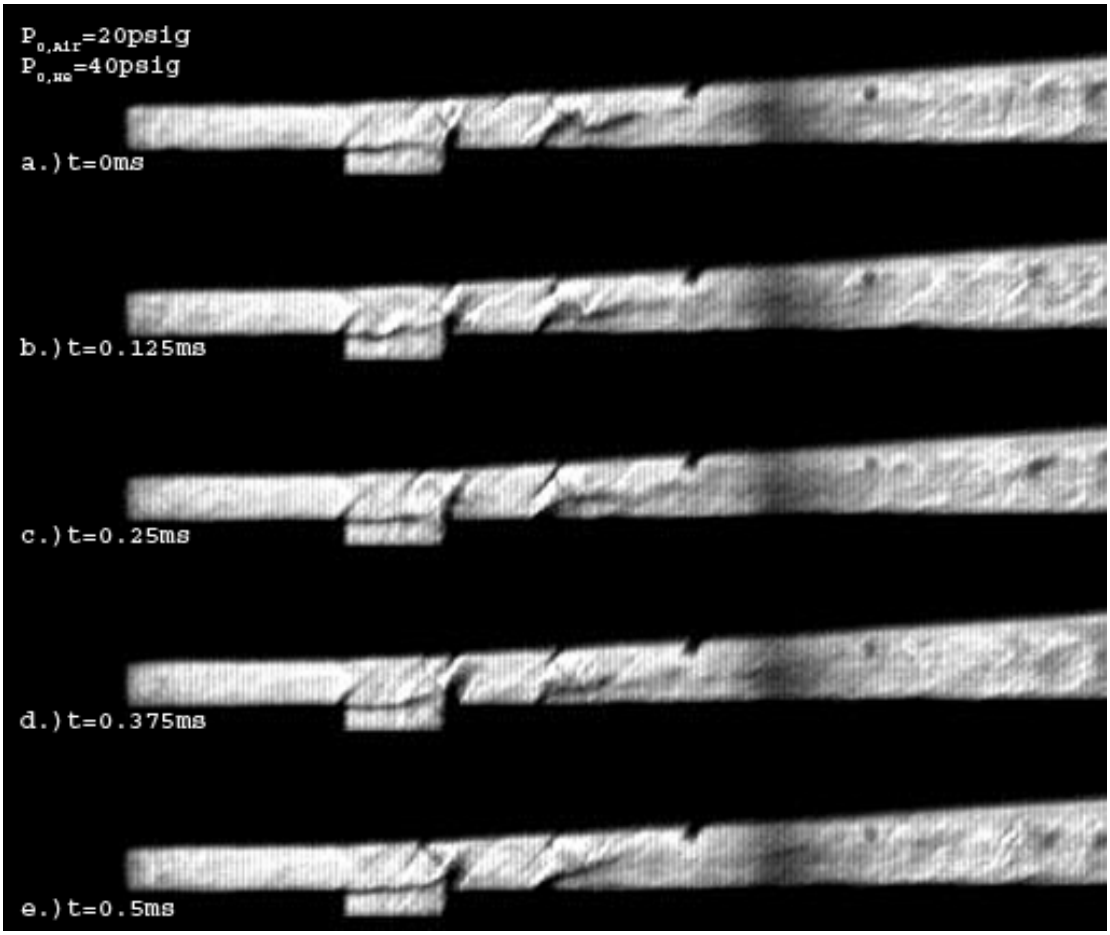

Figure 7.4: Schlieren Images of Cavity Configuration, Optical Configuration #2 for Air=20psig, He=40psig at a.) 0ms b.) 0.125ms c.) 0.25ms d.)0.375ms e.)0.5ms

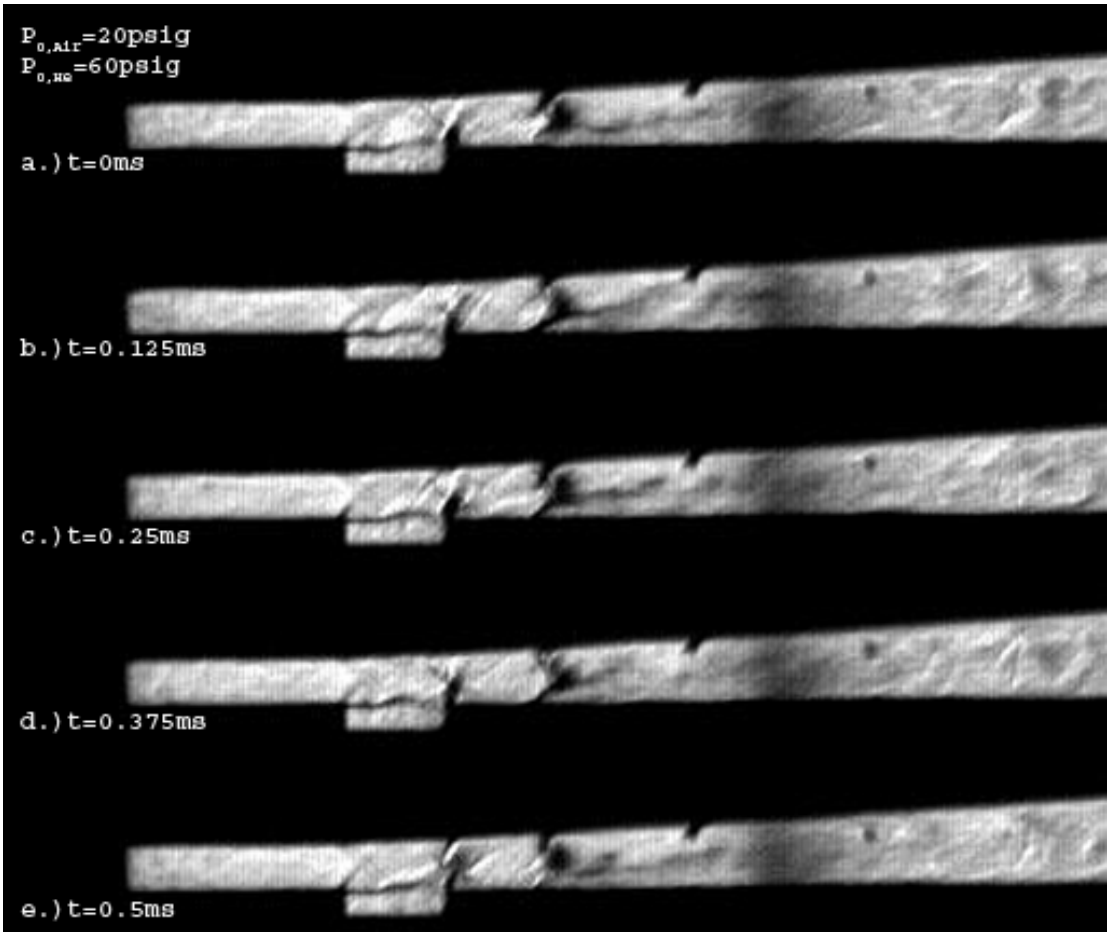

Figure 7.5: Schlieren Images of Cavity Configuration, Optical Configuration #2 for Air=20psig, He=60psig at a.) 0ms b.) 0.125ms c.) 0.25ms d.)0.375ms e.)0.5ms

7.3 Appendix C: Single Line Intensity Maps

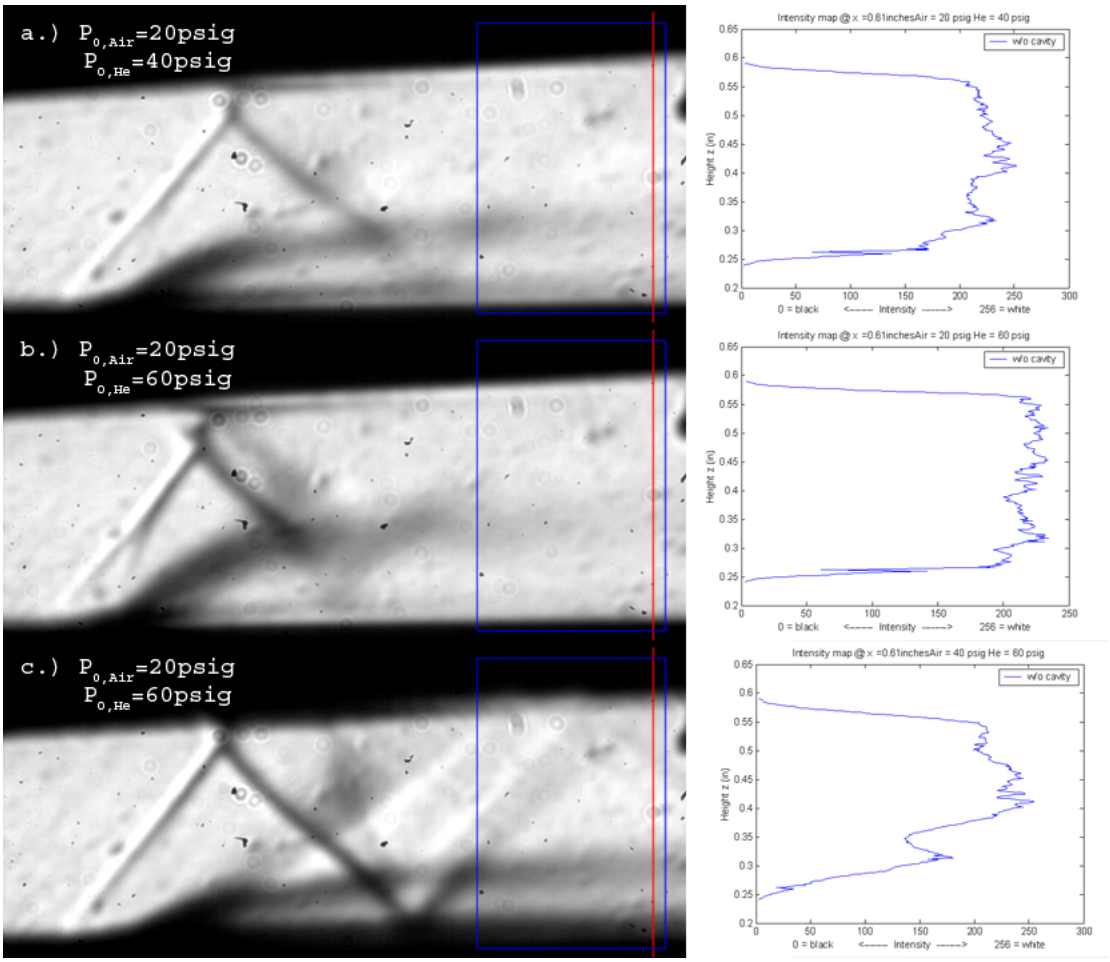

Figure 7.6: Single Pixel Width Intensity Maps for Time Averaged Schlieren Imagery, Baseline Configuration, a) Air=20psig, He=20psig b) Air=20psig, He=40psig c) Air=40psig, He=60psig

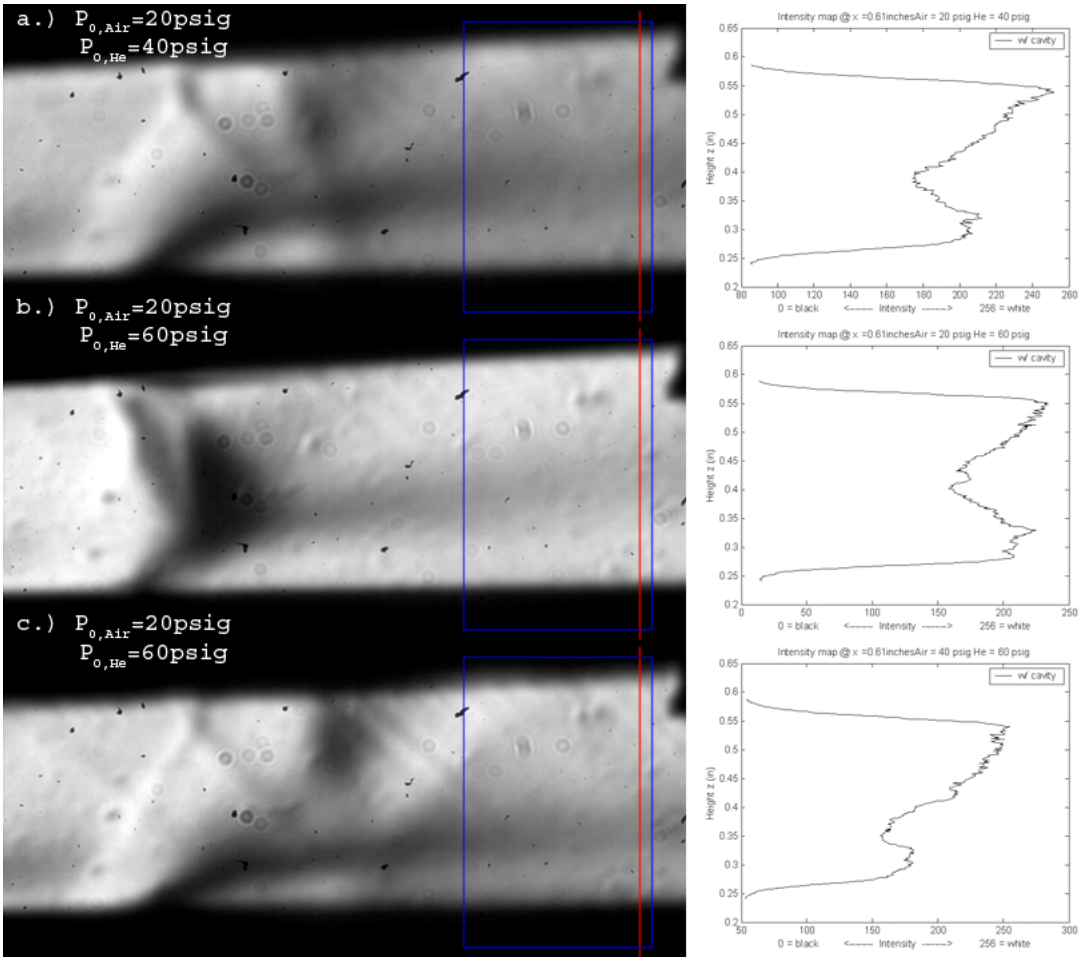

Figure 7.7: Single Pixel Width Intensity Maps for Time Averaged Schlieren Imagery, Cavity Configuration, a) Air=20psig, He=20psig b) Air=20psig, He=40psig c) Air=40psig, He=60psig

7.4 Appendix D: Dynamic Pressure Measurements

Flow conditions for a variety of higher stagnation pressures were run to examine the 'mode hopping' phenomenon which was first exhibited at the Air = 40psig, He = 60psig case. The following FFT outputs were produced and then tabulated in Table 7-1. Predicted frequencies were calculated using previous data for temperature[10], and estimated Mach number. The values in the table show good agreement between predicted and observed results, for frequency and Strouhal number. Also, it should be noted that after the second case the predicted Strouhal number was calculated using the first harmonic predicted frequency (n=1).

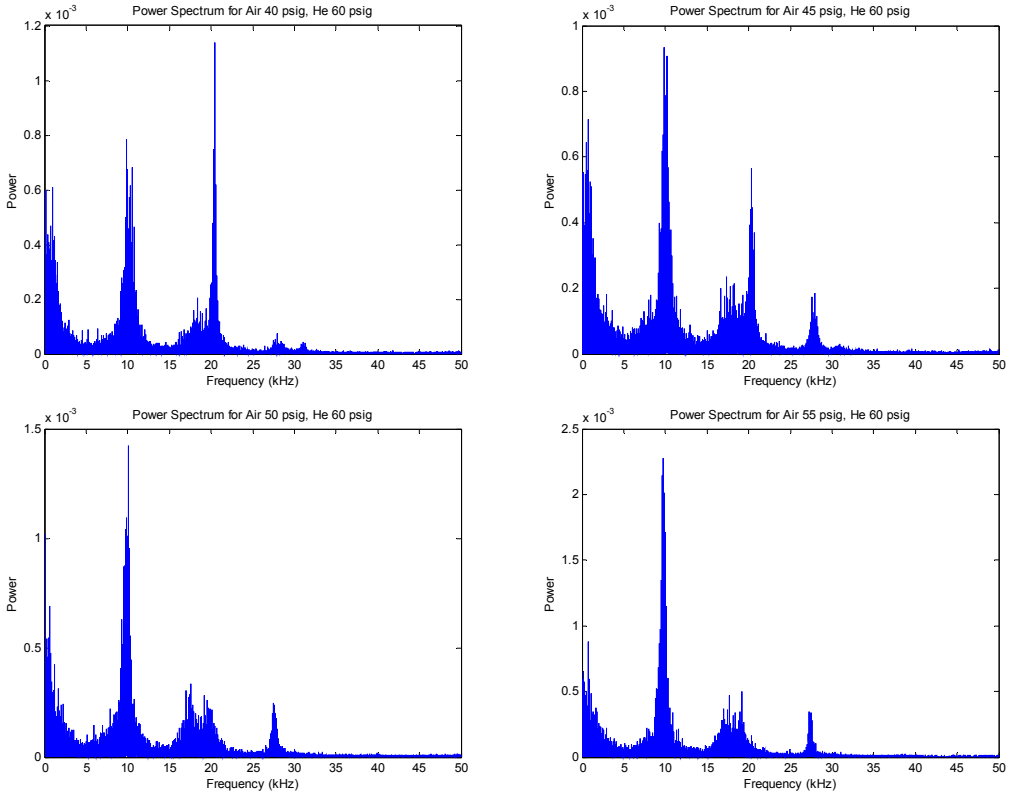

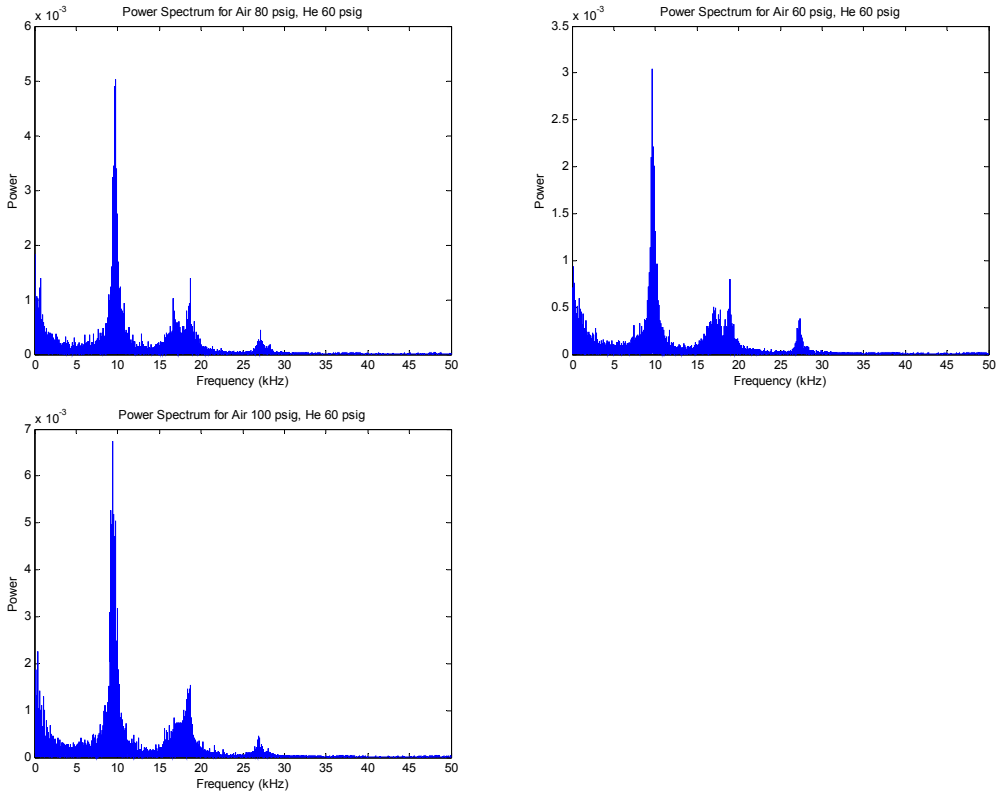

Figure 7.8: Fast Fourier Transforms of Dynamic Pressure Data for Various flow conditions

Table 7-1: Experimental and Predicted Frequencies and Strouhal Numbers for Various Flow Conditions

$P_{0,Air}$	f_{exp}(kHz)	M_{exp}	T_{exp}	U (m/s)	L_{exp} (m)	$Sr_{L,exp}$	k	n=1	$f_{predicted}$ n=2	Sr_L
20	19.8	1.59	196	446	0.0127	0.564	0.57	8.64	20.2	0.574
40	20.5	1.48	205	419	0.0127	0.621	0.57	8.31	19.4	0.588
45	9.87	1.47	205	421	0.0127	0.297	0.57	8.35	19.5	0.251
50	10.1	1.49	206	428	0.0127	0.299	0.57	8.45	19.7	0.250
55	9.69	1.46	205	419	0.0127	0.294	0.57	8.31	19.4	0.252

60	9.61	1.45	206	417	0.0127	0.293	0.57	8.29	19.3	0.252
80	9.74	1.51	202	430	0.0127	0.288	0.57	8.45	19.7	0.250
100	9.44	1.46	206	420	0.0127	0.285	0.57	8.33	19.4	0.252

7.5 Appendix E: LIBS Data Plots

As discussed in section 4.4.3 the standard deviation is a good representative measure of the variance in the measurements and thus a good indicator of the turbulence in the flow. Images presented below are the same as those presented earlier except with the standard error bars replaced with the standard deviation at each point. This shows that there is a lot of variance in the collected data and implies that larger data sets would be required to provide more certainty (this is also demonstrated by the uncertainty plots shown in 4.4.2).

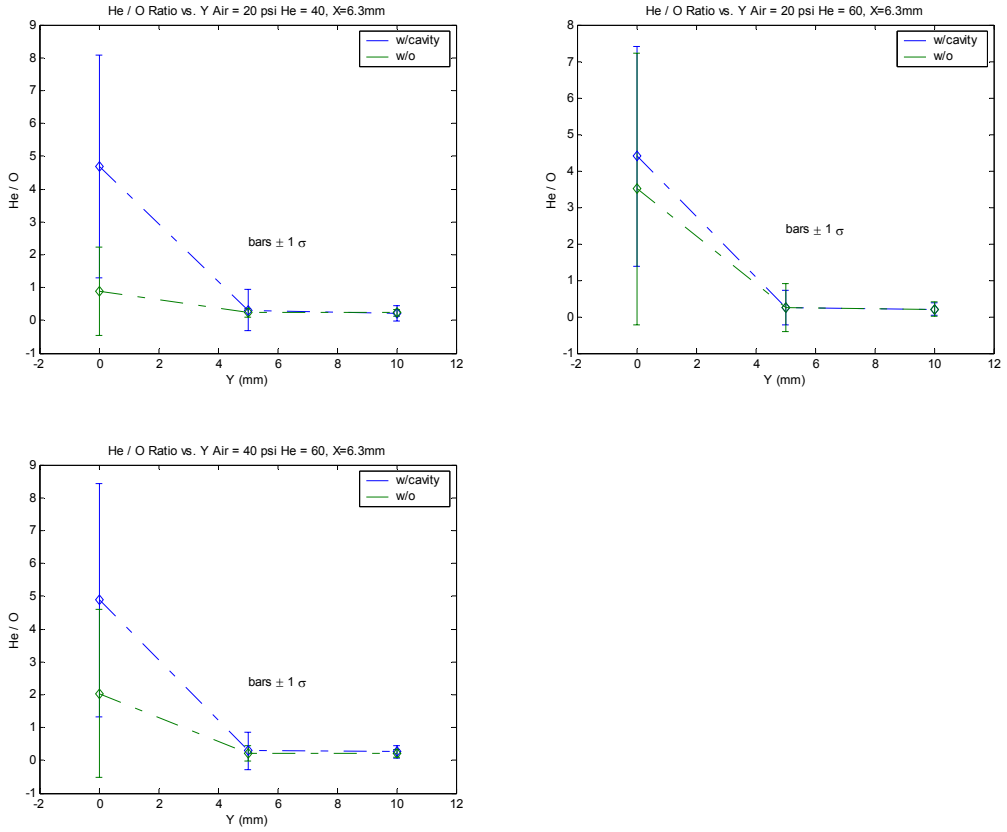

Figure 7.9: He/O Ratio versus Spanwise Distance at X=6.3, for Both Configurations and all

Three Flow Conditions, shown with Standard Deviations

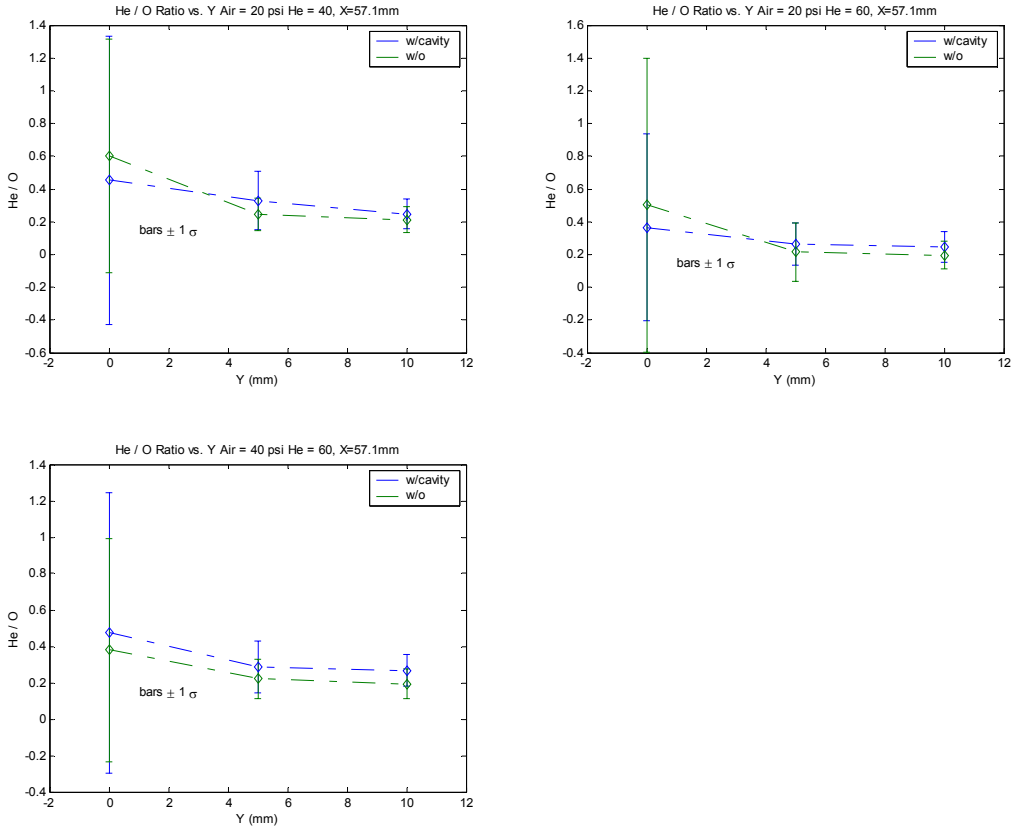

Figure 7.10: He/O Ratio versus Spanwise Distance at X=57.1, for Both Configurations and all Three Flow Conditions, shown with Standard Deviations

BIBLIOGRAPHY

1. Roy, M.M., "Moteurs Thermiques," *Comtes Rendus de l' Academie des Sciences,* Vol. 222, No.1, 1946; see also Royal Aircraft and Establishment Library Translation 112, 1946.
2. Ferri, A., "Discussion on M. Roy's Paper Propulsion Supersonique par Turboreacteurs et par Statoreacteurs," *Advances in Aeronautical Sciences,* Vol. 1, Pergamon, Oxford, England, U.K., 1959, pp. 79-112.
3. Ferri, A., Libby, P.A., and Zakkay V., "Theoretical and Experimental Investigations of Supersonic Combustion," *Proceedings of the International Council of the Aeronautical Sciences, Third Congress, Stockholm, 1962.* Spartan, New York, 1964, pp. 1089-1155.
4. Curran, E.T., "Scramjet Engines: The First Forty Years," *Journal of Propulsion and Power*, Vol. 17, No.6, Nov-Dec 2001, pp. 1138-1148.
5. Weber, R.J., and MacKay, J.S., "An Analysis of Ramjet Engines using Supersonic Combustion," NACA TN 4386, Sept. 1958.
6. Seiner, J.M., Dash, S.M., and Kenzakowski, D.C., "Historical Survey on Enhanced Mixing in Scramjet Engines," *Journal of Propulsion and Power*, Vol. 17, No. 6, 2001, pp. 1273-1286.
7. Burnes, R., Parr, T.P., and Yu, K., "Investigation of Supersonic Mixing Control Using Cavities: Effect of Fuel Injection Location,"*36th AIAA/ASME/SAE/ASEE Joint Propulsion Conference and Exhibit,* AIAA 2000-3618. July 2000.

8. Gutmark, E.J., Schadow, K.C., Yu, K., "Mixing Enhancement in Supersonic Free Shear Flows," *Annual Review of Fluid Mechanics*, Vol. 27, 375-417, 1995.
9. Mathur, T., Gruber, M., Jackson, K., Donbar, J., Donaldson, W., Jackson, T., and Billig, F., "Supersonic Combustion Experiments with a Cavity-Based Fuel Injector," *Journal of Propulsion and Power*, Vol. 17, No. 6, 2001.
10. Nenmeni, V. A. R., "Flow Induced Cavity Resonance for Turbulent Compressible Mixing Enhancement in Scramjets," *Master's Thesis*, Univ. of MD, College Park, 2002.
11. Tarpley, C., Kothari, A.P., "Effect of Trimmed Flight on Inward-Turning SSTO RLV GTOW," *12th AIAA International Space Planes and Hypersonic Systems and Technologies Meeting,* AIAA 2003-6995. December 2003.
12. Billig, F.S., and Kothari, A.P., "Streamline Tracing: Technique for Designing Hypersonic Vehicles," *Journal of Propulsion and Power*, Vol. 16, No. 3, May-June 2000.
13. Takashima, N. and Lewis, M. J., "Navier-Stokes Computation of a Viscous Optimized Waverider," Journal *of Spacecraft and Rockets,* vol. 31, no. 3, 1994, pp. 383-391.
14. Billig, F.S., "SCRAM – A Supersonic Combustion Ramjet Missile," at *29th AIAA/SAE/ASME/ASEE Joint Propulsion Conference,* AIAA 93-2329, June 1993.
15. Kothari, A.P., Tarpley, C., McLaughlin, T.A., and Babu, B.S. "Hypersonic Vehicle Design Using Inward Turning Flow Fields," at *32nd AIAA/SAE/ASME/ASEE Joint Propulsion Conference,* AIAA 96-2552, July 1996.

16. Kothari, A.P., "Designs of and Methodology for Inward or Outward, and Partially Inward or Outward Turning Flow Hypersonic Air-Breathing and Rocket-Based-Combine-Cycle Vehicles," United States Patent #6164956. Dec. 26, 2000.
17. Cutler, A.D., Diskin, G.S., Danehy, P.M., Drummond, J.P., "Fundamental Mixing and Combustion Experiments for Propelled Hypersonic Flight," *38th AIAA/ASME/SAE/ASEE Joint Propulsion Conference and Exhibit*, AIAA 2002-3879, July 2002.
18. Cutler, A.D., Danehy, P.M., O'Byrne, S., Rodriguez, C.G., Drummond, J.P. "Supersonic Combustion Experiments for CFD Model Development and Validation (Invited)" at *42nd Aerospace Sciences Meeting and Exhibit*, AIAA 2004-266, January 2004.
19. Bogdanoff, D.W., "Advanced Injection and Mixing Techniques for Scramjet Combustors," *Journal of Propulsion and Power*, Vol. 10, No.2, 1994.
20. Kutschenreuter, P., "Supersonic Flow Combustors," *Scramjet propulsion*, edited by Curran, E.T., and Murthy, S.N.B., Progress in Astronautics and Aeronautics Series, Vol. 189, 2000, pp. 513-568.
21. Tishkoff, J.M., Drummond, J.P., and Edwards, T., "Future Directions of Supersonic Combustion Research: Air Force/NASA Workshop on Supersonic Combustion," *35th Aerospace Sciences Meeting & Exhibit,* AIAA 1997-1017, January 1997.
22. Yu, G., Li, J.G., Chang, X.Y., and Chen, L.H., "Investigation of Kerosene Combustion Characteristics with Pilot Hydrogen in Model Supersonic

Combustors," *Journal of Propulsion and Power*, Vol. 17, No. 6, 2001.

23. Fernando, E.M., and Menon, S., "Mixing Enhancement in Compressible Mixing Layers: An Experimental Study," *AIAA Journal*, Vol. 31, No. 2, 1993.
24. Ferri, A., "Mixing-Controlled Supersonic Combustion," *Annual Review of Fluid Mechanics,* Vol. 5, 1973, pp. 301-338.
25. Cain, T., and Walton, C., "Review of Experiments on Ignition and Flameholding in Supersonic Flow," *38th AIAA/ASME/SAE/ASEE Joint Propulsion Conference & Exhibit,* AIAA 2002-3877. July 2002.
26. Van Griethuysen, V.J., Glickstein, M.R., Petley, D.H., Gladden, H.J., and Kubik, D.L., "High-Speed Flight Thermal Management," *Developments in High-Speed-Vehicle Propulsion Systems*, Edited by Murthy, S.N.B, and Curran, E.T., Progress in Astronautics and Aeronautics Series, Vol. 165, 1996, pp. 517-579.
27. Billig, F.S., and Jacobsen, L.S., "Comparison of Planar and Axisymmetric Flowpaths for Hydrogen Fueled Space Access Vehicles (Invited)," *39th AIAA/ASME/SAE/ASEE Joint Propulsion Conference and Exhibit*, AIAA 2003-4407. July 2003.
28. Heiser, W.H., and Pratt, D.T., et al., "Hypersonic Airbreathing Propulsion," AIAA Education Series, AIAA, 1994.
29. Gutmark, E.J., Schadow, K.C., and Yu, K.H., "Mixing Enhancement in Supersonic Free Shear Flows," *Annual Review of Fluid Mechanics*, Vol. 27, 1995, pp. 375-417.
30. Brown, G.L., and Roshko, A., "On Density Effects and Large Structure in

Turbulent Mixing Layers," *Journal of Fluid Mechanics,* Vol. 64, part 4, pp. 775-816.

31. Slessor, M.D., Bond, C.L. and Dimotakis, P.E., "Turbulent Shear Layer Mixing at High Reynolds Numbers: Effects of Inflow Condition," Journal *of Fluid Mechanics*, Vol. 376, 1998, pp. 115-138.
32. Dimotakis, P.E., "The Mixing Transition in Turbulent Flows," *Journal of Fluid Mechanics,* Vol. 409, 2000, pp. 69-98.
33. Papamoschou, D., "Structure of the Compressible Turbulent Shear Layer," AIAA *Journal,* Vol. 29, No. 5, 1989.
34. Papamoschou, D., and Roshko, A., "The Compressible Turbulent Shear Layer: an Experimental Study," *Journal of Fluid Mechanics,* Vol. 197, 1988, pp. 453-477.
35. Yu, K.H., Schadow, K.C., "Role of Large Coherent Structures in Turbulent Compressible Mixing," *Experimental Thermal and Fluid Science,* Vol. 14, 1997. pp. 75-84.
36. Nenmeni, V.A., and Yu, K.H., "Cavity-Induced Mixing Enhancement in Confined Supersonic Flows," *40th Aerospace Sciences Meeting & Exhibit,* AIAA 2000-1010, January 2000.
37. Ben-Yakar, A., and Hanson, R.K., "Cavity Flame-Holders for Ignition and Flame Stabilization in Scramjets: An Overview," *Journal of Propulsion and Power*, Vol. 17, No. 4, 2001, pp. 869-877.
38. Yu, K.H., Wilson, K.J., and Schadow, K.C., "Effect of Flame-Holding Cavities

on Supersonic-Combustion Performance," *Journal of Propulsion and Power,* Vol. 17, No. 4, 2001, pp. 1288-1295.

39. Yu, K.H., Wilson, K.J., Smith, R.A., and Schadow, K.C., "Experimental Investigation on Dual-Purpose Cavity in Supersonic Reaction Flow," *36th Aerospace Sciences Meeting & Exhibit,* AIAA 1998-0723, January 1998.
40. Yu, K.H., Wilson, K.J., and Schadow, K.C., "On the use of Combustor Wall Cavities for Mixing Enhancement," *3rd ASME/JSME Joint Fluids Engineering Conference,* FEDSM 1999-7255, July 1999.
41. Zhang, X., "Compressible Cavity Flow Oscillation due to Shear Layer Instabilities and Pressure Feedback," *AIAA Journal*, Vol. 33, No. 8, 1995, pp. 1404-1411.
42. Murry, R.C., and Elliot, G.S., "Characteristics of the Compressible Shear Layer over a Cavity," *AIAA Journal,* Vol. 39, No.5, 2001, pp. 846-856.
43. Cattafesta III, L.N., and Garg, S., "Experiments on Compressible Flow-Induced Cavity Oscillations," *29th Fluid Dynamics Conference,* AIAA 1998-2912, June 1998.
44. Rossiter, J.E., "Wind Tunnel Experiments on the Flow over Rectangular Cavities at Subsonic and Transonic Speeds," *British Aeronautical Research Council, Repts. And Memoranda 3488.* 1964.
45. Heller, H.H., and Bliss, D.B., "Physical Mechanism of Flow-Induced Pressure Fluctuations in Cavities and Concepts for Their Suppression," AIAA 1975-491.
46. Ferri, A., "Review of Problems in Application of Supersonic Combustion,"

Journal of the Royal Aeronautical Society, Vol. 68, No. 645, 1964, pp. 575-595.

47. Weidner, E.H., and Drummond, J.P., "Numerical Study of Staged Fuel Injection for Supersonic Combustion," *AIAA Journal,* AIAA 1981-1468R, Vol. 20, No. 10, pp. 1426-1431.
48. Turns, S.R., "An Introduction to Combustion: Concepts and Applications," McGraw-Hill International Editions: Mechanical Engineering Series, McGraw-Hill, 2000.
49. Waltrup, P.J., and Billig, F.S., "Prediction of Precombustion Wall Pressure Distributions in Scramjet Engines," *Journal of Spacecraft and Rockets*, Vol. 10, No. 9, 1973.
50. Billig, F.S., "Combustion Processes in Supersonic Flow," *AIAA Journal of Propulsion and Power,* Vol. 4, No. 3, 1988.
51. Billig, F.S., "Research on Supersonic Combustion," *Journal of Propulsion and Power*, Vol. 9, No.4, 1993
52. Yang, Wen-Jei, "Handbook of Flow Visualization," Taylor & Francis, Second Edition, 2001.
53. Dalziel, S.B., Hughes, G.O., Sutherland, B.R., "Whole-field Density Measurements by 'Synthetic Schlieren'," *Experiments in Fluids*, Vol. 28, 2000, pp. 322-335.
54. Fu, S., and Wu, Y., "Detection of Velocity Distribution of a Flow Field using Sequences of Schlieren Images," *Optical Engineering*, Vol. 40, No. 8, 2001, pp. 1661-1666.

55. Sutherland, B.R., Dalziel, S.B., Hughes, G.O., and Linden, P.F., "Visualization and Measurement of Internal Waves by 'Synthetic Schlieren'. Part1. Vertically oscillating cylinder," *Journal of Fluid Mechanics,* Vol. 390, 1999, pp. 93-126.

56. Muruganandam, T.M., Kim, B., Olsen, R., Patel, M., Romig, B., and Seitzman, J.M., "Chemiluminescence Based Sensors for Turbine Engines," *39th AIAA/ASME/SAE/ASEE Joint Propulsion Conference & Exhibit*, AIAA 2003-4490, 2003.

57. Mayinger, F., "Optical Measurements: Techniques and Applications," *Springer-Verlag*, 1994, pp. 356.

58. Ikeda, Y., Kojima, J., Nakajima, T., "Local Damkoler Number Measurement In Turbulent Methane/Air Premixed Flames by Local OH*, CH*, and C_2* Chemiluminescence," *36th AIAA/ASME/SAE/ASEE Joint Propulsion Conference and Exhibit*, AIAA 2000-3395, 2000.

59. Higgins, B., McQuay, M.Q., Lacas, F., Rolon, J.C., Darabiha, N., Candel, S., "Systematic Measurements of OH Chemiluminescence for Fuel-Lean, High-Pressure, Premixed, Laminar Flames," *Fuel*, Vol. 80, 2001, pp. 67-74.

60. Gaydon, A.G., "Spectroscopy of Flames," John Whiley & Sons, Inc., New York, 1957, pp. 195-196.

61. Ferioli, F. and Buckley, S. G., "Measurements of Hydrocarbons using Laser-Induced Breakdown Spectroscopy," *Combustion and Flame*, accepted.

62. Yalcin S et al. "Influence of Ambient Conditions on the Laser Air Spark," *Applied Physics B*, Vol. 68, 1999, pp. 121-130.

63. Buckley, S.G., Johnsen, H.A., Hencken, K.R., and Hahn, D.W. "Implementation of Laser-Induced Breakdown Spectroscopy as a Continuous Emissions Monitor for Toxic Metals," Waste *Management*, Vol. 20, 2000, pp. 455-462.

64. Bonnet, J.P., Gresillon, D., Taran, J.P., "Non-intrusive Measurements for High-Speed, Supersonic, and Hypersonic Flows," *Ann. Rev. Fluid Mech.*, Vol. 30, pp. 231-273.

65. Saad, M., "Compressible Fluid Flow," *Prentice Hall*, Second Edition, 1993, pp. 485-493.

66. Tempel, T., "Investigation of Supersonic Mixing Using Laser Induced Breakdown Spectroscopy," *Master's Thesis*, University of Maryland, College Park, 2003.